SANDIA REPORT

SAND2008-5592
Unlimited Release
Printed August 2008

Modeling and Design Optimization of Adhesion Between Surfaces at the Microscale

Kevin T. Sylves

Prepared by
Sandia National Laboratories
Albuquerque, New Mexico 87185 and Livermore, California 94550

Sandia is a multiprogram laboratory operated by Sandia Corporation,
a Lockheed Martin Company, for the United States Department of Energy's
National Nuclear Security Administration under Contract DE-AC04-94-AL85000.

Issued by Sandia National Laboratories, operated for the United States Department of Energy by Sandia Corporation.

Available to DOE and DOE contractors from
U.S. Department of Energy
Office of Scientific and Technical Information
P.O. Box 62
Oak Ridge, TN 37831

Telephone: (865) 576-8401
Facsimile: (865) 576-5728
E-Mail: reports@adonis.osti.gov
Online ordering: http://www.osti.gov/bridge

Available to the public from
U.S. Department of Commerce
National Technical Information Service
5285 Port Royal Rd
Springfield, VA 22161

Telephone: (800) 553-6847
Facsimile: (703) 605-6900
E-Mail: orders@ntis.fedworld.gov
Online ordering: http://www.ntis.gov/help/ordermethods.asp?loc=7-4-0#online

SAND2008-5592
Unlimited Release
Printed August 2008

Modeling and Design Optimization of Adhesion Between Surfaces at the Microscale

Kevin T. Sylves
Department of Aerospace Engineering Sciences
University of Colorado
Boulder, CO 80305
sylves@colorado.edu

Abstract

This research applies design optimization techniques to structures in adhesive contact where the dominant adhesive mechanism is the van der Waals force. Interface finite elements are developed for domains discretized by beam elements, quadrilateral elements or triangular shell elements. Example analysis problems comparing finite element results to analytical solutions are presented. These examples are then optimized, where the objective is matching a force-displacement relationship and the optimization variables are the interface element energy of adhesion or the width of beam elements in the structure. Several parameter studies are conducted and discussed.

Acknowledgment

The author would like to thank his co-advisors at the University of Colorado: Kurt Maute of the Aerospace Engineering Sciences department and Martin L. Dunn of the Mechanical Engineering Department; as well as his mentor at Sandia, E. David Reedy Jr. of the Applied Mechanics Development group.

The author gratefully acknowledges funding by a Sandia National Laboratories Campus Executive Laboratory Directed Research and Development (LDRD) research project. Sandia is a multiprogram laboratory operated by Sandia Corporation, a Lockheed Martin Company, for the United States Department of Energy's National Nuclear Security Administration under contract DOE. No. DE-AC04-94AL85000.

Contents

List of Figures

List of Tables

Chapter 1

Introduction

Adhesion is a phenomenon that has wide-ranging and increasingly important applications and effects in industry, nature and daily life. This report explores methods for designing surfaces with novel, previously unavailable adhesive properties through the coupling of advanced finite element techniques and the mathematics of topology optimization. The intent is to tailor surface force distributions to create strong or weak adhesion between structural members, as dictated by particular device applications and requirements.

As characteristic length scales in structures approach the micro and nanometer range, surface interaction forces play an increasingly important role in adhesion phenomena. The phenomenon of stiction in MEMS devices is one example of the power of surface interaction forces at the microscale [55]. At the nanoscale, the usually weak van der Waals forces between molecules can dominate depending on the geometry and topology of the surfaces in contact. For example, it has been shown that nanoscale hair-like structures on the feet of geckos allow them to stick to nearly any surface through van der Waals forces and support many times their own weight ([13], [47]).

Recent advances in nanomanufacturing technologies have created the potential for fabricating surfaces that utilize nanostructures for tailored adhesion properties. This promises to significantly impact a wide range of technologies in science, engineering and biology. Some example applications are surface engineering of MEMS components to alleviate stiction problems ([26], [50], [55]), creating self-assembling structures [30] and technology to design adhesive substrates for cell capture, adhesion and growth [51].

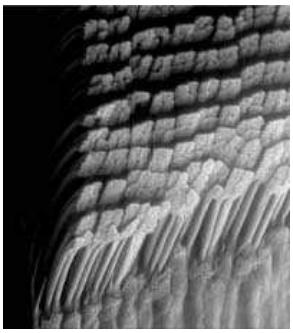

Figure 1.1: A SEM image of setae, or hair, on the foot of a gecko which allows adhesion to surfaces through van der Waals forces. [1]

However, until now no methods have been developed to design the geometry, topology and surface interaction force laws at the microscale. In fact, even the analysis of the phenomena is a challenge for arbitrary geometries. This research involves developing and using finite element methods coupled with topology optimization to develop a design methodology for adhesive microstructures. The types of design problems studied here involve structures that come into or out of adhesive contact at matching points between two surfaces. Specifically, the objective of concern is matching the loading response to a target curve as structures delaminate or come into adhesive contact, although a framework is developed and implemented to allow a wide range of types of design objectives. Only problems with small deformations and displacements are considered. Additionally, interfacial forces considered are restricted to those that act normal to the surfaces and are conservative. Adhesives with tangential friction force components and viscoelastic rate dependencies are not considered. This work is multidisciplinary and combines physical modeling, numerical simulations, and formal design optimization methods.

Chapter 2 is a review of the literature relevant to the work in this report. Chapter 3 describes the analysis framework used including a description of adhesive force laws, formulation of interface finite elements and example simulations. Chapter 4 focuses on the optimization of structures with adhesive surface interactions, beginning with a sensitivity analysis of the interface finite elements followed by several examples of design optimization. Chapter 5 summarizes the key conclusions and gives suggestions for future work.

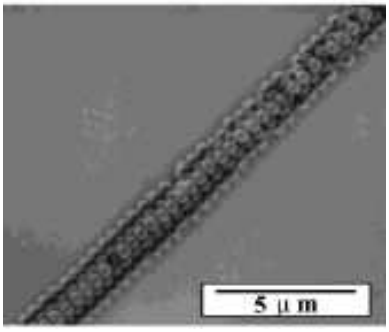

Figure 1.2: A SEM image of a nanowire composed of gold spheres. This wire self-assembled through adhesive forces [30]

Chapter 2

Survey of the Literature

This chapter is a survey of the literature pertaining to the topics of adhesion, modeling and design optimization. It begins with a brief history of the field of adhesive contact mechanics and then goes on to mention current advances in the fields of adhesion in MEMS, adhesion in nature, computational adhesive models and design optimization as they relate to the work presented in this report.

2.1 Brief History of Adhesive Modeling

The study of adhesion between surfaces in close proximity to each other originally grew out of contact theory. The first analytical formulations relating stresses, strains, displacements and forces in contacting spherical bodies were published by Heinrich Hertz in 1882 [18]. He found a cubic relation between the applied force and the radius of the circle of contact between the spheres:

$$a^3 = \frac{PR}{K} \tag{2.1}$$

where a is the radius of the contact circle, P is the contact force,

$$\frac{1}{R} = \frac{1}{R_1} + \frac{1}{R_2} \tag{2.2}$$

where R_1 and R_2 are the radii of the spheres, and

$$\frac{1}{K} = \frac{3}{4}\left(\frac{1-\nu_1^2}{E_1} + \frac{1-\nu_2^2}{E_2}\right) \tag{2.3}$$

where E_1 and E_2 are the Young's moduli and ν_1 and ν_2 are the Poisson's ratios of the spheres.

Fritz London, in 1930, used principles of quantum mechanics to explain attractive forces observed between inert noble gas atoms [28]. These forces, called van der Waals forces after 19th century Dutch physicist Johannes Diderik van der Waals, arise due to instantaneous dipole moments caused by a temporary asymmetrical distribution of electrons in a atom or molecule's electron cloud. These forces are negligibly weak when atoms are separated by large distances, but

become dominant as surfaces come with 100 nm or less of each other. London showed that the potential energy between molecules due to van der Waals forces is given by:

$$U = -\frac{C}{r^6}, \tag{2.4}$$

where C is the London constant, $\sim 10^{-79} Jm^6$ [32].

As molecules approach each other, this attractive force grows until the electron clouds begin to overlap, creating a very large repulsive effect referred to as Pauli or Born repulsion. Although quantum mechanics yields that the energy of repulsion $\sim e^{\frac{r_c}{r}}$, typically it is expressed $\sim \frac{1}{r^n}$ with $n > 10$ [32]. The most common expression for interaction energy that takes into account both London attraction forces and Born repulsion forces is the Lennard-Jones potential:

$$U = \frac{D}{r^{12}} - \frac{C}{r^6} \tag{2.5}$$

where $D = \frac{r_0^6 C}{2}$ and r_0 is the equilibrium radius between attraction and Born repulsion.

Bradley [4] and Deryagin [10], also in the early 1930s, showed that adhesive "pull-off" force between a rigid contacting sphere and plane is

$$F = 2\pi\Gamma R \tag{2.6}$$

where Γ is the energy of adhesion per area, and

$$\Gamma = \gamma_1 + \gamma_2 - \gamma_{12} \tag{2.7}$$

where γ_1 and γ_2 are the surface energies of the materials in contact and γ_{12} is their interfacial energy.

In the 1970s two new and apparently conflicting adhesive theories emerged for elastic spheres in contact. Johnson, Kendall and Roberts formulated a theory based on experiments on the interaction of rubber, a relatively flexible material, and glass [25]. This came to be known as the JKR theory of adhesive contact. They noticed that the contact area of a sphere of rubber on a glass substrate was larger than Hertz contact theory predicted and theorized that adhesive forces deformed the sphere surface into contact, shown in Figure 2.1b. JKR theory is analogous to fracture mechanics where the edge of the contact area coincides with a crack in mode I. At the rim of the circular contact area infinite stresses are sustained until the sphere is abruptly pulled off the substrate at $F = \frac{3}{2}\pi\Gamma R$.

However, researchers Derjaguin, Muller and Toporov independently developed an alternate theory, called DMT theory, describing adhesion in the contact of elastic spheres which yielded different predictions than the JKR theory [9]. In DMT theory adhesive forces are present in a ring outside the circular contact area, shown in Figure 2.1c. The profile, however, remains Hertzian and the stresses at the edge of the contact area remain finite. They find that when the sphere is in

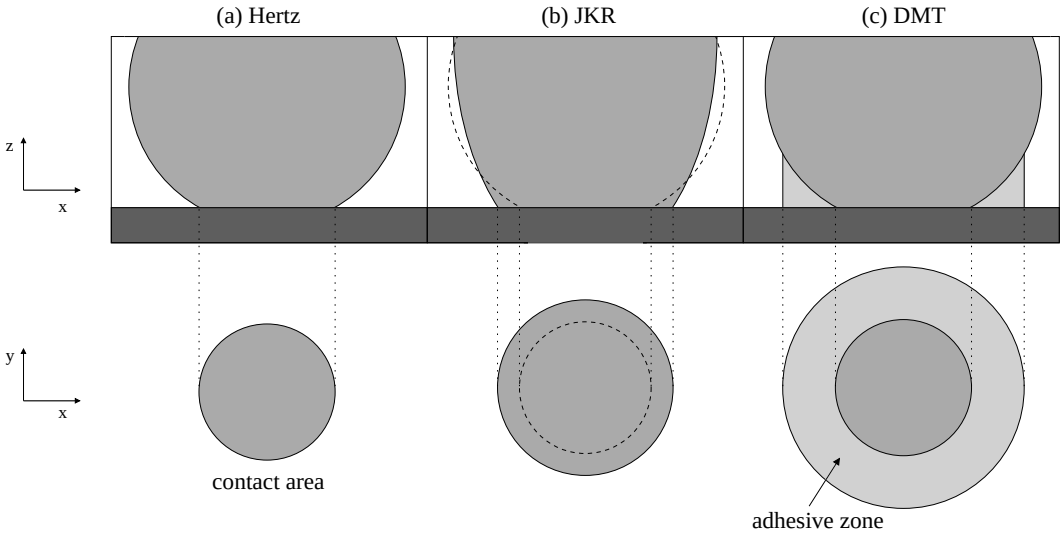

Figure 2.1: Diagram showing different adhesive contact models for a sphere pressing into a plane. (a) Hertz theory, no adhesion. (b) JKR theory, adhesive forces increase contact area, no adhesive forces outside of contact area. (c) DMT theory, sphere deformation same as Hertz, additional ring of adhesive forces outside of contact area.

contact with a substrate at a single point the pull-off force reduces to $F = 2\pi\Gamma R$ as in the theory for rigid spheres but tends to $F = \pi\Gamma R$ as the contact area increases.

These two theories which lead to different conclusions were reconciled by Tabor [49]. He defined a dimensionless parameter μ, later referred to as the Tabor number, where

$$\mu = \left(\frac{\Gamma^2 R}{E^2 Z_0^3} \right)^{\frac{1}{3}} \tag{2.8}$$

and Z_0 is the equilibrium distance between atoms. In cases of soft solids (small E) and large adhesion energy, $\mu \gg 1$ and the JKR theory is valid. For hard solids and relatively smaller adhesion energy, $\mu \ll 1$ and the DMT theory is valid. For intermediate values of μ there is a smooth transition between JKR and DMT models. Analytical expressions for the JKR-DMT transition were formulated by Maugis [31] by assuming a Dugdale model for the adhesive law between surfaces (described in Section 3.1.2.2).

2.2 Adhesive Modeling

Baney and Hui [2] extend the work of Maugis to describe the adhesion between long cylinders. They define a parameter λ which is proportional to the Tabor number μ. They find a relation between the force applied to the top of the cylinder per length P and the contact radius a by enforcing the condition that the singularity in the adhesive zone cancels the singularity from the contact pressure and integrating. In the case of a cylinder the contact area is rectangular and the contact radius is half the width of the contact area. One important conclusion of their work is that for cylinders, as λ approaches 0 the solution tends to the Hertz instead of the DMT model. This is due to the difference in the way that adhesive forces scale with characteristic contact length in 2D (cylinder) and 3D (sphere) cases. This work is used directly here in Section 3.4.

Johnson and Greenwood [24] found adhesion maps for a sphere in contact over a range of Tabor numbers analytically by using a Dugdale adhesion model, but with the errors in the Dugdale approximation corrected by numerical results using a Lennard-Jones adhesion model. The Lennard-Jones model is described in Section 3.1.2.1 and is a more realistic model than the Dugdale. However, closed form analytical solutions of the force-displacement characteristics cannot be obtained with the Lennard-Jones model.

Reedy [44] developed a theory for a rigid sphere coming into contact with a rigid surface coated in a thin elastic layer. He then verified his analytical theory through finite element analysis. He used a triangular adhesion model as in Section 3.1.2.3 and traced the JKR P-a curve as in Figure 3.30 for both the case with and without the elastic coating layer. In his finite element analysis the adhesion law was incorporated into the contact algorithm already implemented in his finite element code. In this work adhesion and contact are incorporated into the finite element model through material nonlinearities in an interface element.

Cho and Park [7] incorporated a Lennard-Jones adhesive model in their finite element analysis

of a sphere coming into contact with a substrate. They used the commercial ABAQUS finite element code and introduced the adhesive force as nonlinear body forces. They employed a quasi-static solver and nonlinear geometry analysis for large deformation effects.

Hui et al. [21] develop an analytical model based on JKR theory for the analysis of periodically rough surfaces at the microscale. In MEMS devices, surface roughness directly correlates to adhesion energy. Rough surfaces, because asperities keep the bulk of the surface from being within the range of van der Waals forces, have less adhesive energy than more smooth surfaces. They found a closed form relation between applied load, contact area and adhesion energy for arbitrary surface profiles.

Mi et al. [36] use interface elements which are completely analogous to the Inter elements presented in Chapter 3 to analyze the crack propagation and force-displacement characteristics in a double cantilever beam example. They use a triangular adhesive model. They claim that the interface element technique in simulating crack propagation was first used by Hilleborg et al. in 1976 [20]. They note the importance of mesh refinement to reduce ”peakiness” of the results, which leads to poor convergence. They advocate adaptive meshing if the location of the crack tip location or path is not previously known.

2.3 Adhesion in Micromechanical Structures

Zhao et al. [55] review some important topics in adhesion as it relates to microelectromechanical systems (MEMS). In these devices adhesion is often referred to as ”stiction” and can be problematic. Although in some cases stiction occurs due to capillary or electrostatic forces, it often arises due to van der Waals forces as described in this report.

Tayebi and Polycarpou [50] study how roughening the surface between MEMS structures can reduce adhesive effects. They conclude that increased surface roughness, as well as asymmetry in the asperity heights and decreased asperity thickness can reduce the adhesive energy between two surfaces. In the beam delamination example presented in Section 3.3 it is assumed that surface roughness is the mechanism for altering the adhesive energy in strips along the beam-substrate interface.

Knapp and de Boer [26] present an example of a microbeam in adhesive contact with a surface and compare experimental, numerical and analytical results. One important result that they present and that is duplicated here is that the choice of adhesive model has little effect on the final deformed shape of the beam. They gather beam deflection data experimentally using interferometry and calculate the energy of adhesion associated with the interface by matching to finite element simulation results. Both the experimental and finite element beam deflections are compared to analytical results derived from basic beam theory. The same approach was used here in Section 3.3, although without experimental results.

An example of an application of adhesive design that could benefit from optimization is presented by Meitl et al [34]. They present an elastomeric stamp which is used to transfer micropar-

ticles arranged in patterns from one surface to another through van der Waals adhesion forces. For example, optimization could be employed to design adhesive gradients on the stamp surface that would roll particles from one configuration into another.

2.4 Adhesion in Biology

Gao et al. [13] describe how the topology of the feet of geckos allows them to move along vertical walls and ceilings. They have a dense array of nanohairs on their feet called setae which can get close enough to the wall surface so that a large surface area of setae are within the range of van der Waals adhesion. Additionally, asymmetry in the setae allow the adhesion energy to change based on the orientation of the seta, allowing the gecko foot to release and lift off the surface. Since the adhesive characteristics of the gecko foot are entirely governed by the geometry of the surface, it is possible that design optimization of adhesive surfaces can be utilized to recreate the novel adhesion characteristics of gecko feet or other adhesive objectives in manufactured devices.

Sitti and Fearing [47] and Northen and Turner [39] propose designs for synthetic microscale adhesives based on observations of gecko feet. They present several approaches of microfabricating structures that mimic the setae of geckos. Their work is mainly experimental and does not include finite element analysis. Their microstructures were designed without design optimization techniques.

Tsibouklis et al. [51] design low surface energy coatings for implants. By reducing the energy of adhesion of surfaces through coating, bacteria cannot adhere as easily, reducing the formation of hazardous biofilms.

2.5 Design Optimization

There is currently very little work published on optimization of surfaces in adhesive contact where the dominant adhesion force is from van der Waals attraction. Yao and Gao [53] use an analytical approach to find optimal shapes of two contacting surfaces, with the objective of maximizing the adhesive pull-off force. However, the analytical approach is limited to axisymmetric problems where the adhesive energy in the interface is constant. In order to deal with general problem formulations and complex geometries we present a computational approach drawing from topology optimization of structures that come into contact without adhesion [42], [29], [11], [19]. These methods allow for the design of structures by starting with only boundary conditions and a design domain but do not account for adhesion, whereas the work presented in this paper focuses on designing the adhesive pattern between predefined structures.

Pajot [40] also investigates the design optimization of structures with nonlinear properties. He looks at designing structures with geometric nonlinearities such as buckling and studied the problems in optimization of systems that may develop limit points and turning points. He used the

same optimization algorithm, GCMMA, as is used here in Chapter 4, as well as the same nonlinear finite element framework and solvers used in Chapter 3.

Groth and Nordlund [16] use shape optimization to optimize adhesive joints at the macroscale. However they do not model the adhesive as intermolecular forces but instead focus on classical structural criteria such as the strength of the adhesive joint.

Chapter 3

Analysis Framework

In this chapter the general models used for contact and adhesion are described in detail. Three finite element models that incorporate these models are derived. The method for solving the materially nonlinear problem is then discussed. Finally, examples demonstrating the accuracy of these elements in matching analytical solutions as well as parameter studies are presented.

3.1 Modeling and Element Implementation

The adhesive contact model presented here stems from a one-dimensional forcing model. This model includes a force which is a function of the gap between two particles experiencing van der Waals attraction and Born repulsion, and can be thought of as a nonlinear spring. This spring has an equilibrium length, which corresponds to the equilibrium gap where the Born repulsion forces from electron cloud overlap balances the attractive van der Waals adhesion forces. However, the restoring force only increases up to a point, at which the decay rate of the van der Waals force outpaces the decay rate of the repulsion forces and the sum force acting on the particles begins to decrease.

This one-dimensional spring model is introduced in the literature when accounting for van der Waals forces between nodes in finite element analysis. Liu et al. [27] use this approach in their atomic scale finite element modeling. As nodes (atoms) approach each other, nonlinear spring elements are adaptively inserted when the distance between nodes is less than some cutoff value. These spring elements serve both to prevent surface penetration and to include adhesive van der Waals forces. Other researchers use a similar method of incorporating surface forces as nonuniform distributed loads that are functions of the nodal displacements [26], [7]. In another model, the gap between two surfaces remains identically zero while any interfacial forces exist [43], [52]. These forces drop to zero when the gap becomes greater than zero and are a function of the viscosity of the adhesive. This formulation is more appropriate for macro-scale adhesive problems such as those involving the delamination of composite materials and is not explored in this report.

3.1.1 Contact by Penetration Penalty

First, the penalty contact formulation is described. A one-dimensional one degree of freedom contact example is shown in Figure 3.1. Considering an elastic body subject to conservative external

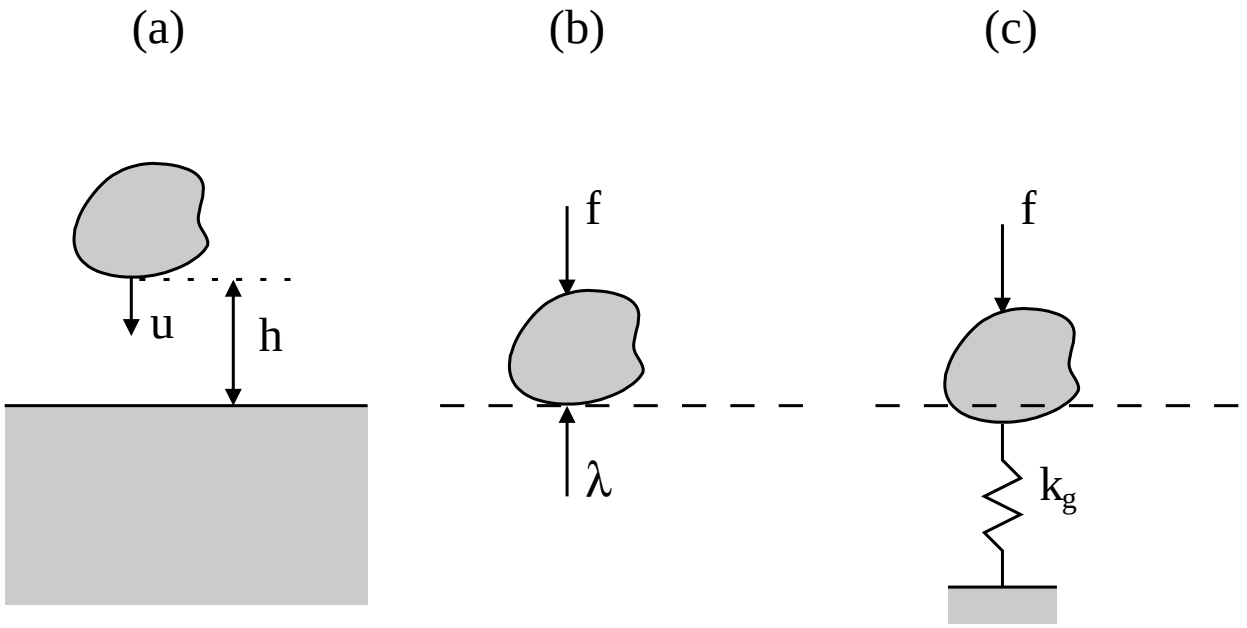

Figure 3.1: A body coming into contact with a surface. (a) Definition of initial gap h and displacement u. (b) Lagrange multiplier λ as reaction force preventing penetration. (c) Contact penalty as spring with stiffness k_g, allowing penetration.

forces, the potential energy Π of the system to be minimized can be expressed as

$$\Pi = U + W + \Pi_a(g) \tag{3.1}$$
$$g = h - u \geq 0 \tag{3.2}$$

Here U is the internal strain energy, W is the external work and Π_a is the adhesive energy in the system, defined as a function of the gap, g. Contact occurs when g is reduced to zero. To account for this, the energy minimization problem is constrained by the inequality (3.2), where h is the initial distance between the points closest to each other on the body and surface coming into contact and u is the displacement of the same point on the body.

Two standard methods for enforcing this constraint in conservative problems are the penalty and Lagrange multiplier methods [52]. In the Lagrange multiplier method, the potential energy is augmented by a term

$$\Pi_L = \lambda g \tag{3.3}$$
$$\Pi = U + W + \Pi_a(g) + \Pi_L, \tag{3.4}$$

where λ is a Lagrange multiplier and analogous to a reaction force at the interface preventing penetration. This term must be solved for as an additional variable. The penalty method, which is the method used in this work, augments the internal strain energy function by a term

$$\Pi_p = \frac{1}{2} k_g (g^-)^{2n} \tag{3.5}$$

$$\Pi = U + W + \Pi_a(g) + \Pi_p, \tag{3.6}$$

where g^- is zero for positive gaps and g for negative values. The value k_g is a penalty factor and is analogous to the stiffness of a spring that resists penetration but does not completely prevent it.

The interface elements used are derived by integrating a one-dimensional force model over the area of an interface segment. Wriggers [52] refers to this as an isoparametric contact element approach. One limitation in this approach is that tangential components of interfacial forces such as friction are not included. However, this model is sufficiently accurate for the design problems under consideration in this paper.

The penetration penalty is introduced in the interface elements as an interface stress σ which depends on the gap g for negative gap values:

$$\sigma(g) = \begin{cases} cg & ,g < 0 \\ 0 & ,g \geq 0, \end{cases} \tag{3.7}$$

where c is the penetration penalty.

3.1.2 One-Dimensional Adhesion Models

While the contact formulations define the response of the Inter elements for negative gaps or penetrations, several adhesion formulations have been developed that define how the Inter elements respond to positive gaps. In adhesion there is decreasing stiffness as the gap grows larger, and when two surfaces have debonded there is no longer any stiffness contribution from the gap between them. Three adhesion models have been implemented here: the Lennard-Jones, the Dugdale and a triangular model. The Lennard-Jones model is the sum of two inverse polynomials representing the adhesive van der Waals force and repulsive electron cloud overlap. The Dugdale model is an artificially constructed function that makes some analytical calculations easier but is not rooted in reality. It is a notch function with a constant force per area over a certain gap range and zero everywhere else. The triangular function is a linear approximation of the Lennard-Jones model with a positively sloped section, a negatively sloped section and zero everywhere else.

3.1.2.1 Lennard-Jones Model

Of all the models describing adhesion presented here, the Lennard-Jones model most realistically models forces between particles at the nanoscale. Equation 3.8 for the force per area between two

perfectly smooth surfaces was derived by integrating the Lennard-Jones potential between two atoms.

$$\sigma(g) = \frac{a}{(bg+1)^3} - \frac{a}{(bg+1)^9} \tag{3.8}$$

where g is the gap or distance between two surfaces. This function was constructed so that the equilibrium state $\sigma = 0$ is at the origin. In reality there is some non-zero distance between atomic nuclei which is a stable equilibrium. The term $a(bg+1)^{-3}$ represents the contribution from the van der Waals force. The term $-a(bg+1)^{-9}$ in Equation 3.8 is due to the strong repulsion that arises when the electron clouds of neighboring atoms begin to overlap. This effect is what prevents solids from penetrating each other at the macroscale. The Lennard-Jones function, which is shown in Figure 3.2, sums the effects from van der Waals attraction and electron cloud repulsion.

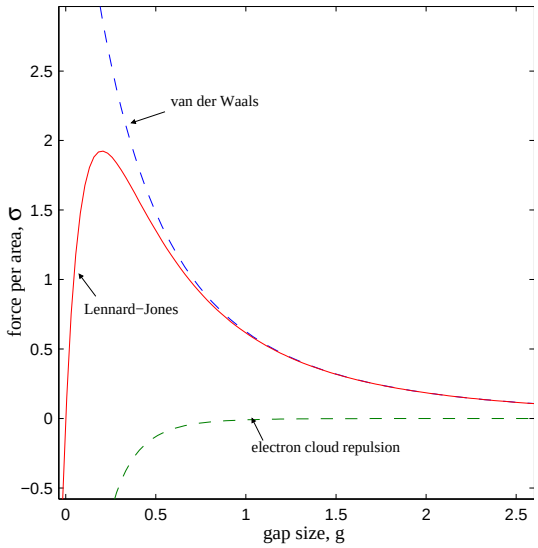

Figure 3.2: The Lennard-Jones model for attraction and repulsion between atoms as a sum of van der Waals forces and electron cloud interaction

The constants a and b in Equation 3.8 can be expressed in terms of characteristics of the Lennard-Jones function such as the maximum force per area σ_m, the distance between particles that corresponds to that force per area g_m and the surface energy or adhesive strength per area Γ. The maximum force per area σ_m occurs when the derivative $\frac{d\sigma}{dg} = 0$. Solving for b in terms of g_m,

$$\frac{d\sigma}{dg} = ab\left[-3(bg_m+1)^{-4} + 9(bg_m+1)^{-10}\right] = 0 \tag{3.9}$$

$$\begin{aligned} 3(bg_m+1)^{-4} &= 9(bg_m+1)^{-10} \\ (bg_m+1)^6 &= 3 \\ b &= \frac{3^{\frac{1}{6}}-1}{g_m}. \end{aligned} \tag{3.10}$$

The constant a can be expressed in term of σ_m:

$$\begin{aligned}
\sigma(g_m) = \sigma_m &= \frac{a}{\left(b\frac{3^{\frac{1}{6}}-1}{b}+1\right)^3} - \frac{a}{\left(b\frac{3^{\frac{1}{6}}-1}{b}+1\right)^9} \\
&= a\left(3^{-\frac{1}{2}} - 3^{-\frac{3}{2}}\right) \\
&= \frac{2\sqrt{3}}{9}a \\
a &= \frac{3\sqrt{3}}{2}\sigma_m
\end{aligned} \tag{3.11}$$

Alternately, either of these can be replaced with an expression relating a and b to each other and adhesion energy Γ. Adhesion energy per area is defined as the integral of the adhesion force per area σ over the distance between particles g:

$$\begin{aligned}
\Gamma &\equiv \int_0^\infty \sigma(g)\,dg \\
\frac{\Gamma}{a} &= \int_0^\infty (bg+1)^{-3}\,dg - \int_0^\infty (bg+1)^{-9}\,dg
\end{aligned} \tag{3.12}$$

Making the substitution $x = bg+1$,

$$\begin{aligned}
\frac{b\Gamma}{a} &= \int_1^\infty x^{-3}dx - \int_1^\infty x^{-9}dx \\
&= \frac{3}{8} \\
a &= \frac{8b\Gamma}{3}
\end{aligned} \tag{3.13}$$

One notable feature of the Lennard-Jones function is the existence of a singularity when the terms in the denominators approach zero. This occurs when $g = -\frac{1}{b} \approx -0.2g_m$. This makes the function by itself unsuitable for analysis when there are large penetrations, necessitating a piecewise function combining a linear or quadratic contact penalty and the Lennard-Jones formulation.

3.1.2.2 Dugdale Model

While the Lennard-Jones model is based closely on actual physical phenomena, the Dugdale model is constructed for mathematical reasons in deriving analytical solutions to example adhesion problems. For example, in Baney and Hui [2] a Dugdale model is used to derive closed-form solutions

to the Hertz and JKR problem for a cylinder. The Dugdale model is simply

$$\sigma(g) = \begin{cases} \frac{\Gamma}{u_2} & ,g < u_2 \\ 0 & ,g \geq u_2 \end{cases} \tag{3.14}$$

where Γ is defined in the same was as for the Lennard-Jones model (the adhesion energy per area, or the area under the force per area curve) and u_2 is a critical gap size. The function is shown in Figure 3.3. Note that the slope of this function is zero everywhere, and there are C^0 discontinuities

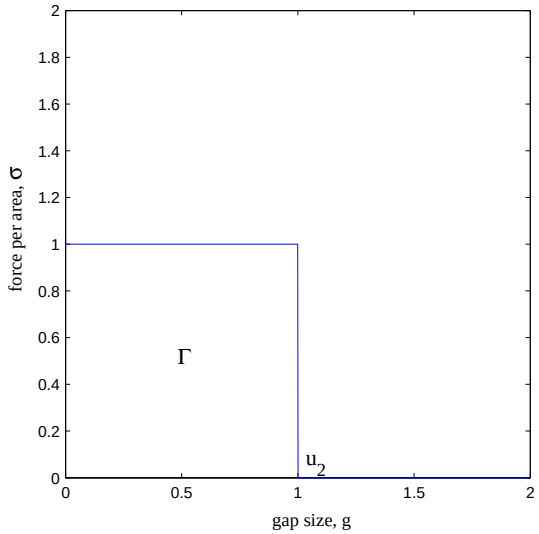

Figure 3.3: The Dugdale model for attraction between surfaces

at the origin and u_2. both of these features make this particular function ill-suited for numerical analysis.

3.1.2.3 Triangular Model

The triangular model is a compromise between the Lennard-Jones and Dugdale models. Like the Dugdale there is a critical gap u_2 after which the force per area is identically zero. However, the triangular model is C^0 continuous and has non-zero slope in the adhesive zone facilitating numerical solution methods. The force per area function for the triangular model is

$$\sigma(g) = \begin{cases} \frac{2\Gamma}{u_1 u_2} g & ,g < u_1 \\ \frac{2\Gamma(g-u_2)}{u_2(u_1-u_2)} & ,u_1 \leq g < u_2 \\ 0 & ,g \geq u_2 \end{cases} \tag{3.15}$$

where Γ is the adhesion per area as defined in Equation 3.12, u_1 is the critical gap corresponding to the maximum force per area (corresponding to g_m in the Lennard-Jones model) and u_2 is the gap size where the force per area becomes zero, as shown in Figure 3.4. Examples of triangular functions with various u_1 and u_2 values are shown graphically in Figure 3.18 in Section 3.3.3.

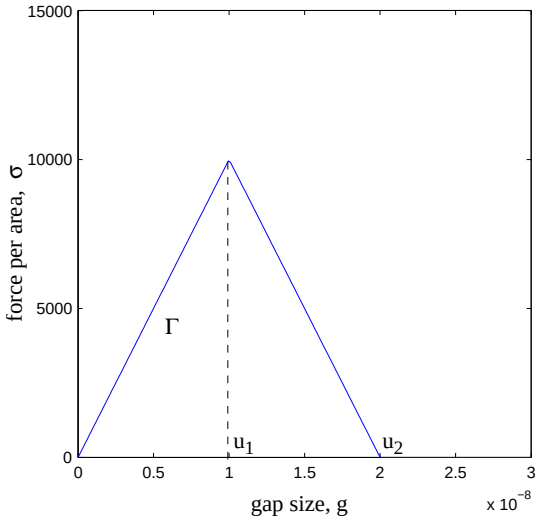

Figure 3.4: The triangular model for attraction between surfaces

3.1.3 Finite Element Development

A finite element discretization of these contact and adhesion models is developed here. The Inter elements, unlike other type of finite elements, are designed to be used in conjunction with specific other types of elements and cannot be used on their own. Specifically, they are designed to be placed topologically between two surfaces of the same element type, connecting them. The internal force and stiffness in Inter elements depend on the gap between the two surfaces as dictated by a contact and adhesion model pair, introducing a material nonlinearity to the system.

In nonlinear finite element analysis the internal force $\mathbf{p}$ and the tangential stiffness matrix $\mathbf{K}_t$ need to be formulated. The nonlinear solver requires these two quantities to determine the displacements of the system for the next step or Newton iteration. In the adhesion/contact problem studied here both $\mathbf{p}$ and $\mathbf{K}_t$ can be derived from a potential energy function U, implying that the system is conservative. This potential energy is the integral of a surface potential function S integrated over the area between two surfaces:

$$U = \iint_A S(g)dA \tag{3.16}$$

The surface potential S is defined to be the integral of the adhesive force per area σ:

$$S(g) \equiv \int_0^g \sigma(g)dg \tag{3.17}$$

where g is the gap between surfaces. Note from equation 3.12 that:

$$\Gamma = \lim_{g\to\infty} S(g) \tag{3.18}$$

The internal force $\mathbf{p}$ is defined as:

$$\mathbf{p} \equiv \frac{\partial U}{\partial \mathbf{u}} \tag{3.19}$$

Substituting Equations 3.16 and 3.17 into Equation 3.19 yields a general finite element equation for the internal force between two surfaces, which will be specialized to interface elements: the InterQuad, InterBeam and InterShell elements.

$$\begin{aligned} \mathbf{p} &= \frac{\partial}{\partial \mathbf{u}} \left[\iint_A S(g) dA \right] \\ &= \iint_A \frac{dS}{dg} \frac{\partial g}{\partial \mathbf{u}} dA \\ &= \iint_A \sigma(g) \frac{\partial g}{\partial \mathbf{u}} dA \end{aligned} \tag{3.20}$$

A general form for the tangential stiffness matrix can also be derived:

$$\begin{aligned} \mathbf{K}_t &\equiv \frac{\partial^2 U}{\partial \mathbf{u} \partial \mathbf{u}} = \frac{\partial \mathbf{p}}{\partial \mathbf{u}} \\ &= \frac{\partial}{\partial \mathbf{u}} \iint_A \sigma(g) \frac{\partial g}{\partial \mathbf{u}} dA \\ &= \iint_A \left[\frac{d\sigma}{dg} \frac{\partial g}{\partial \mathbf{u}} \left(\frac{\partial g}{\partial \mathbf{u}} \right)^T + \sigma(g) \frac{\partial^2 g}{\partial \mathbf{u} \partial \mathbf{u}} \right] dA \end{aligned} \tag{3.21}$$

3.1.3.1 InterQuad

The InterQuad element is two-dimensional with 4 nodes and 8 degrees of freedom, as shown in Figure 3.5. This element is designed to have 4-node quadrilateral elements sharing an edge be-

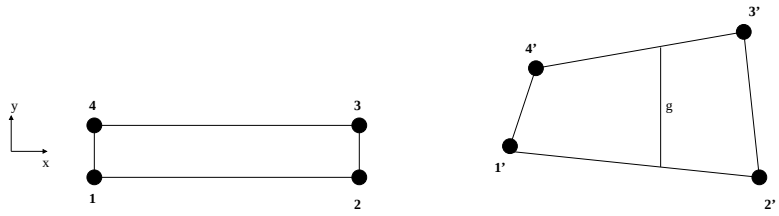

Figure 3.5: InterQuad element. Initial position is on the left with a deformed configuration on the right.

tween nodes 1 and 2 (the bottom edge) and between nodes 3 and 4 (the top edge). The InterQuad contributes stiffness and forces to the system depending on the gap between the top and bottom edges, shown in Figure 3.5 as g. The gap is interpolated from one-dimensional linear shape functions, treating each of the two edges as individual entities. If the local x-axis is aligned with the top

and bottom edges with the origin at nodes 4 and 1 respectively, the x-position can be parameterized:

$$\begin{aligned} x_t &= \frac{1+x_g}{2} L_t \\ x_b &= \frac{1+x_g}{2} L_b \end{aligned} \tag{3.22}$$

where x_t is the location along the top edge, x_b is the location along the bottom edge, L_t and L_b are the lengths of the edges and x_g is a parameterized coordinate that goes from -1 to 1. The linear shape functions for the y-component of the four nodes are:

$$\begin{aligned} N_{1y} &= \frac{1-x_g}{2} \\ N_{2y} &= \frac{1+x_g}{2} \\ N_{3y} &= \frac{1-x_g}{2} \\ N_{4y} &= \frac{1+x_g}{2} \end{aligned}$$

The gap g between the edges at given corresponding x-locations x_g can be written as a function of shape functions $N_{()y}$, nodal y-displacements $u_{()y}$ and initial nodal y-positions $y_{0()}$:

$$g = N_{4y}\left(y_{04}+u_{4y}\right) + N_{3y}\left(y_{03}+u_{3y}\right) - N_{1y}\left(y_{01}+u_{1y}\right) - N_{2y}\left(y_{02}+u_{2y}\right) \tag{3.23}$$

The generalized internal force equation (3.20) and tangential stiffness equation (3.21) can now be specialized to the InterQuad element. The width of the element is constant and the gap value does not change in the z-direction (along the width), reducing the integral for internal force to

$$\mathbf{p} = w \int_0^L \sigma(g) \frac{\partial g}{\partial \mathbf{u}} dx \tag{3.24}$$

where w is the element width and x and L represent either x_b and L_b or x_t and L_t depending on which edge each component of the internal force vector corresponds to. Substituting Equation 3.22 for generalized coordinates allows for a Gauss point approximation of the integral over the length of the element

$$\begin{aligned} \mathbf{p} &= \frac{wL}{2} \int_{-1}^{1} \sigma(g) \frac{\partial g}{\partial \mathbf{u}} dx_g \\ &\cong \frac{wL}{2} \sum_i^n w_i \sigma(g_i) \left.\frac{\partial g}{\partial \mathbf{u}}\right|_{x_{g_i}} \end{aligned} \tag{3.25}$$

where n is the number of Gauss points, x_{g_i} are the generalized coordinates of the Gauss points, w_i are the corresponding weights, and g_i is the gap equation (3.23) evaluated at the gauss points x_{g_i}.

The derivative of the gap g with respect to the elemental displacement vector $\mathbf{u}$ is

$$\frac{\partial g}{\partial \mathbf{u}} = \begin{bmatrix} 0 & -N_{1y} & 0 & -N_{2y} & 0 & N_{3y} & 0 & N_{4y} \end{bmatrix}^T. \tag{3.26}$$

The tangential stiffness matrix can also be specialized to the InterQuad element in the same way. The first observation is that $\frac{\partial^2 g}{\partial \mathbf{u} \partial \mathbf{u}} = 0$, following from Equation 3.26. The tangential stiffness matrix for the InterQuad element, following from Equation 3.21 is

$$\begin{aligned} \mathbf{K}_t &= \iint_A \frac{d\sigma}{dg} \frac{\partial g}{\partial \mathbf{u}} \left(\frac{\partial g}{\partial \mathbf{u}} \right)^T dA \\ &= \frac{wL}{2} \int_{-1}^{1} \frac{d\sigma}{dg} \frac{\partial g}{\partial \mathbf{u}} \left(\frac{\partial g}{\partial \mathbf{u}} \right)^T dx_g \\ &\cong \frac{wL}{2} \sum_i^n w_i \left. \frac{d\sigma}{dg} \right|_{g_i} \left. \frac{\partial g}{\partial \mathbf{u}} \left(\frac{\partial g}{\partial \mathbf{u}} \right)^T \right|_{x_{g_i}} \end{aligned} \tag{3.27}$$

Here, the gap derivative matrix is:

$$\frac{\partial g}{\partial \mathbf{u}} \left(\frac{\partial g}{\partial \mathbf{u}} \right)^T = \begin{bmatrix} 0 & 0 & 0 & 0 & 0 & 0 & 0 & 0 \\ 0 & N_{1y}N_{1y} & 0 & N_{1y}N_{2y} & 0 & -N_{1y}N_{3y} & 0 & -N_{1y}N_{4y} \\ 0 & 0 & 0 & 0 & 0 & 0 & 0 & 0 \\ 0 & N_{2y}N_{1y} & 0 & N_{2y}N_{2y} & 0 & -N_{2y}N_{3y} & 0 & -N_{2y}N_{4y} \\ 0 & 0 & 0 & 0 & 0 & 0 & 0 & 0 \\ 0 & -N_{3y}N_{1y} & 0 & -N_{3y}N_{2y} & 0 & N_{3y}N_{3y} & 0 & N_{3y}N_{4y} \\ 0 & 0 & 0 & 0 & 0 & 0 & 0 & 0 \\ 0 & -N_{4y}N_{1y} & 0 & -N_{4y}N_{2y} & 0 & N_{4y}N_{3y} & 0 & N_{4y}N_{4y} \end{bmatrix} \tag{3.28}$$

The forces in the InterQuad element act only in the local y-direction; there is no friction-like resistance to motion in the tangential direction. Highly distorted elements, where the upper surface may be offset from the lower in the x-direction, will behave in the same manner as rectangular elements since the tangential component of the gap between the surfaces is disregarded. This is true for all three interface elements developed here.

3.1.3.2 InterBeam

The InterBeam element is very closely related to the InterQuad element, except that it is designed to be compatible with 2-node 6-DOF beams along the top and bottom edges. The InterBeam element, shown in Figure 3.6, has 4 nodes and 12 degrees of freedom, two translational and one rotation at each node. Besides the additional rotational degrees of freedom, the major difference between the InterBeam and InterQuad elements is the cubic shape functions. The shape functions

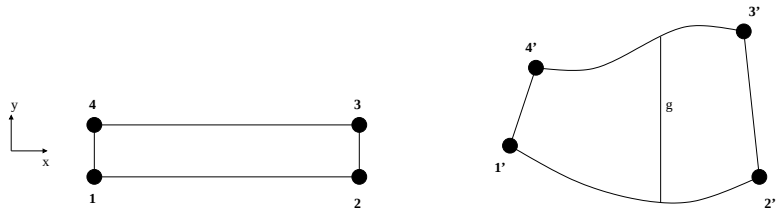

Figure 3.6: InterBeam element. Initial position is on the left with a deformed configuration on the right.

for the InterBeam element are

$$
\begin{aligned}
N_{1y} &= \frac{1}{L_b^3}\left(2x_b^3 - 3L_b x_b^2 + L_b^3\right) \\
N_{1\theta} &= \frac{1}{L_b^3}\left(L_b x_b^3 - 2L_b^2 x_b^2 + L_b^3 x_b\right) \\
N_{2y} &= \frac{1}{L_b^3}\left(-2x_b^3 + 3L_b x_b^2\right) \\
N_{2\theta} &= \frac{1}{L_b^3}\left(L_b x_b^3 - L_b^2 x_b^2\right) \\
N_{3y} &= \frac{1}{L_t^3}\left(-2x_t^3 + 3L_t x_t^2\right) \\
N_{3\theta} &= \frac{1}{L_t^3}\left(L_t x_t^3 - L_t^2 x_t^2\right) \\
N_{4y} &= \frac{1}{L_t^3}\left(2x_t^3 - 3L_t x_t^2 + L_t^3\right) \\
N_{4\theta} &= \frac{1}{L_t^3}\left(L_t x_t^3 - 2L_t^2 x_t^2 + L_t^3 x_t\right)
\end{aligned}
$$

Note that x_b and x_t are used as defined in Equation 3.22 in place of x_g. The gap function g is

$$
\begin{aligned}
g = & N_{4y}\left(y_{04} + u_{4y}\right) + N_{4\theta}u_{4\theta} + N_{3y}\left(y_{03} + u_{3y}\right) + N_{3\theta}u_{3\theta} \\
& - N_{1y}\left(y_{01} + u_{1y}\right) - N_{1\theta}u_{1\theta} - N_{2y}\left(y_{02} + u_{2y}\right) - N_{2\theta}u_{2\theta}
\end{aligned}
\tag{3.29}
$$

Equations 3.25 and 3.27 for the internal force $\mathbf{p}$ and tangential stiffness matrix $\mathbf{K}_t$ are identical for the InterBeam element. The differences are in the shape functions and the derivatives of the gap with respect to the displacement vector. The gap derivative vector for the InterBeam element becomes

$$
\frac{\partial g}{\partial \mathbf{u}} = \begin{bmatrix} 0 & -N_{1y} & -N_{1\theta} & 0 & -N_{2y} & -N_{2\theta} & 0 & N_{3y} & N_{3\theta} & 0 & N_{4y} & N_{4\theta} \end{bmatrix}^T . \tag{3.30}
$$

The gap derivative matrix $\frac{\partial g}{\partial \mathbf{u}}\left(\frac{\partial g}{\partial \mathbf{u}}\right)^T$ is not written explicitly here, but obviously follows from Equation 3.30..

One optional feature in InterBeam elements is the ability to adjust the gap to take the beam thickness into account. In this case the top and bottom edges of the InterBeam are taken as the midlines of the beams, shown in Figure 3.7. If g' is defined to represent the original gap measure-

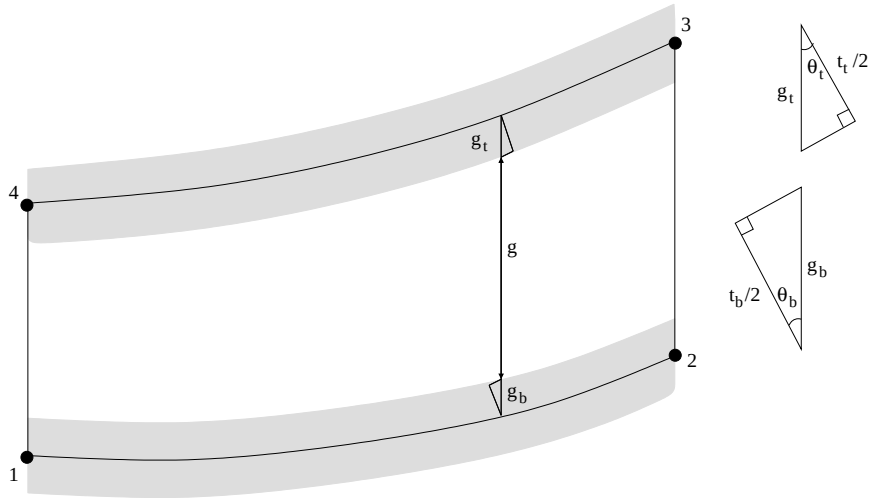

Figure 3.7: The gap g adjusted for beam thicknesses. Triangles show close-up of g_t and g_b construction

ment, the true value for the gap g becomes

$$g = g' - g_t - g_b \tag{3.31}$$

where g_t and g_b are defined graphically in the diagram. With the assumption that beam cross-sections remain normal to the beam midline under bending a relation between the beam slope and the angles θ_t and θ_b emerge

$$\begin{aligned} \tan\theta &= \frac{dy}{dx} \\ \sec\theta &= \sqrt{1+\left(\frac{dy}{dx}\right)^2} \end{aligned} \tag{3.32}$$

From the triangles in Figure 3.7 the following trigonometric relations exist

$$\begin{aligned} g_t &= \frac{t_t}{2}\sec\theta_t \\ g_b &= \frac{t_b}{2}\sec\theta_b \end{aligned} \tag{3.33}$$

where t_t and t_b are the thickness of the top and bottom beams respectively. Substituting Equation

3.32 into Equations 3.33

$$\begin{aligned} g_t &= \frac{t_t}{2}\sqrt{1+\left(\frac{dy_t}{dx_t}\right)^2} \\ g_b &= \frac{t_b}{2}\sqrt{1+\left(\frac{dy_b}{dx_b}\right)^2} \end{aligned} \tag{3.34}$$

Since beam elements are isoparametric the y-coordinate as a function of x along the beam is

$$\begin{aligned} y_t &= \mathbf{N}_t^T \mathbf{x}_t \\ y_b &= \mathbf{N}_b^T \mathbf{x}_b \end{aligned} \tag{3.35}$$

where

$$\begin{aligned} \mathbf{N}_t &= \begin{bmatrix} 0 & N_{4y} & N_{4\theta} & 0 & N_{3y} & N_{3\theta} \end{bmatrix}^T \\ \mathbf{N}_b &= \begin{bmatrix} 0 & N_{1y} & N_{1\theta} & 0 & N_{2y} & N_{2\theta} \end{bmatrix}^T \end{aligned}$$

and

$$\begin{aligned} \mathbf{x}_t &= \begin{bmatrix} x_4 & y_4 & \theta_4 & x_3 & y_3 & \theta_3 \end{bmatrix}^T \\ \mathbf{x}_b &= \begin{bmatrix} x_1 & y_1 & \theta_1 & x_2 & y_2 & \theta_2 \end{bmatrix}^T. \end{aligned}$$

Differentiating Equations 3.35,

$$\begin{aligned} \frac{dy_t}{dx_t} &= \frac{d\mathbf{N}_t^T}{dx_t}\mathbf{x}_t + \mathbf{N}_t^T \underbrace{\frac{d\mathbf{x}_t}{dx_t}}_{=0} \\ \frac{dy_b}{dx_b} &= \frac{d\mathbf{N}_b^T}{dx_b}\mathbf{x}_b + \mathbf{N}_b^T \underbrace{\frac{d\mathbf{x}_b}{dx_b}}_{=0} \end{aligned}$$

and substituting back into Equation 3.34 yields the equations used to modify the midline gap g' to account for beam thicknesses

$$\begin{aligned} g_t &= \frac{t_t}{2}\sqrt{1+\left(\frac{d\mathbf{N}_t^T}{dx_t}\mathbf{x}_t\right)^2} \\ g_b &= \frac{t_b}{2}\sqrt{1+\left(\frac{d\mathbf{N}_b^T}{dx_b}\mathbf{x}_b\right)^2} \end{aligned} \tag{3.36}$$

3.1.3.3 InterShell

The InterShell element shown in Figure 3.8, unlike the InterBeam and InterQuad, is fully three-dimensional and is meant to be compatible with 3-node 18-DOF triangular shell elements. It has

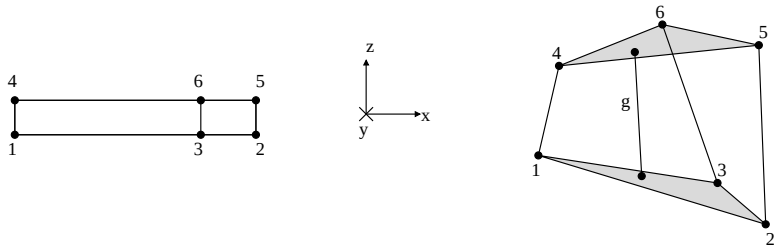

Figure 3.8: InterShell element. Initial position is on the left with a deformed configuration on the right. The gap g measured between the top and bottom surfaces is shown

6 nodes with 6 degrees of freedom at each node for a total of 36 degrees of freedom. It has upper and lower triangular surfaces defined by nodes 4,5,6 and 1,2,3 respectively. The overall element is prismatic in shape. The top and bottom surfaces are interpolated with linear shape functions for simplicity. Rotations at the nodes are not taken into account. The shape functions for the shell elements are

$$\begin{aligned} N_1 &= \zeta_1 \\ N_2 &= \zeta_2 \\ N_3 &= \zeta_3 \\ N_4 &= \zeta_1 \\ N_5 &= \zeta_2 \\ N_6 &= \zeta_3 \end{aligned}$$

where ζ_1, ζ_2 and ζ_3 are generalized triangular coordinates of a given point on the top or bottom surface of the element. The gap g can be described in terms of these shape functions and z-displacements and initial conditions.

$$\begin{aligned} g =& N_4\left(z_{04}+u_{4z}\right)+N_5\left(z_{05}+u_{5z}\right)+N_6\left(z_{06}+u_{6z}\right) \\ & -N_1\left(z_{01}+u_{1z}\right)-N_2\left(z_{02}+u_{2z}\right)-N_3\left(z_{03}+u_{3z}\right) \end{aligned} \tag{3.37}$$

The internal force can be specialized from the general form (Equation 3.20) by converting from Cartesian to triangular coordinates. Using the relation

$$dA = Jd\zeta_1 d\zeta_2 d\zeta_3 \tag{3.38}$$

where J is the Jacobian determinant. For linear shape functions the Jacobian determinant J reduces to either the area A_t or A_b, depending on whether it is the top or bottom surface under consideration.

The specialized internal force vector becomes

$$\begin{aligned}\mathbf{p} &= \int_0^1\int_0^1\int_0^1 \sigma(g)\frac{\partial g}{\partial \mathbf{u}} J d\zeta_1 d\zeta_2 d\zeta_3 \\ &= A\int_0^1\int_0^1\int_0^1 \sigma(g)\frac{\partial g}{\partial \mathbf{u}} d\zeta_1 d\zeta_2 d\zeta_3\end{aligned}$$

and with triangular Gauss integration approximation

$$\mathbf{p} \cong A\sum_i^n \sigma(g_i)\frac{\partial g_i}{\partial \mathbf{u}} w_i \tag{3.39}$$

where n is the number of points in the Gauss integration rule, g_i represents the gap evaluated at Gauss points and w_i is the weighting factors of each Gauss point. The gap derivative vector $\frac{\partial g}{\partial \mathbf{u}}$ has zeros for all non-z-component entries, negative nodal shape functions for the first three nodes and positive nodal shape functions for the last three nodes. since this vector is constant in $\mathbf{u}$ the second derivative $\frac{\partial^2 g}{\partial \mathbf{u}\partial \mathbf{u}} = 0$. The specialized tangential stiffness matrix can be derived from Equation 3.21

$$\begin{aligned}\mathbf{K}_t &= \int_0^1\int_0^1\int_0^1 \frac{d\sigma}{dg}\frac{\partial g}{\partial \mathbf{u}}\left(\frac{\partial g}{\partial \mathbf{u}}\right)^T J d\zeta_1 d\zeta_2 d\zeta_3 \\ &\cong A\sum_i^n w_i \left.\frac{d\sigma}{dg}\right|_{g_i} \frac{\partial g_i}{\partial \mathbf{u}}\left(\frac{\partial g_i}{\partial \mathbf{u}}\right)^T\end{aligned} \tag{3.40}$$

Again for space considerations the 36x36 gap derivative matrix $\frac{\partial g_i}{\partial \mathbf{u}}\left(\frac{\partial g_i}{\partial \mathbf{u}}\right)^T$ is not included. It includes 36 non-zero entries and has a structure very similar to that of the gap derivative matrix for the InterQuad element.

3.2 Nonlinear Solver

The material nonlinearity introduced by the contact and adhesion models in the Inter elements require the use of a nonlinear finite element solver. In linear systems the stiffness matrix $\mathbf{K}$ of the system is constant, allowing the displacements vector $\mathbf{u}$ to be solved for in a single step. Additionally, the principle of superposition applies, meaning that solutions for different system boundary conditions can be added. In nonlinear systems, however, the stiffness of the system is a function of the displacements, meaning that the solution cannot be computed in a single step. At each equilibrium displacement vector a tangential stiffness matrix $\mathbf{K}_t$ must be computed to predict the displacement of the next incremental step. A Newton corrector method is applied to applied to reduce the residual of the resulting prediction until the guess is satisfactorily close to a new equilibrium state. There are several methods for stepping through equilibrium states to the solution. Those shown in Figure 3.9 are the load control, state or displacement control and arclength control.

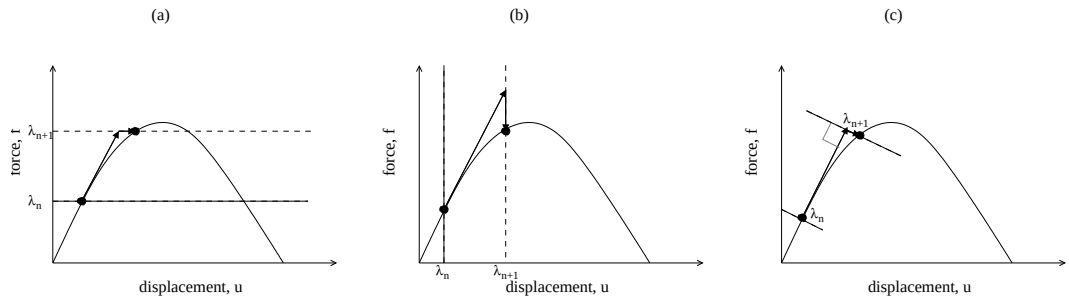

Figure 3.9: Sketch of different nonlinear solution methods. (a) Load control. (b) State (displacement) control. (c) Arclength control.

The diagram shows a one-dimensional simplification of the displacement and force vectors. The methods can be abstracted to higher dimensions. In all methods the step size is $\Delta\lambda$ and the $n+1^{th}$ step is $\lambda_{n+1} = \lambda_n + \Delta\lambda$. In the forward Euler method, which is the method used in this work, a prediction is made for the solution in step λ_{n+1} by moving along a vector tangent to the residual path (defined by the tangential stiffness matrix $\mathbf{K}_t$) until a constraint is met. In the load control method, this constraint is a hyperplane defined by a fraction of the total applied force. The Newton corrector method then traverses along this constant force plane until the guess is close enough to the equilibrium residual curve, as defined by a convergence tolerance. In the displacement control method the constraint for the first prediction is instead a constant displacement hyperplane that is defined by a fraction of the applied displacements vector. The advantage of the displacement control method is the ability to traverse limit points on the equilibrium residual curve. A limit point is a critical point where the tangential stiffness matrix $\mathbf{K}_t$ becomes singular and the tangent to the equilibrium path is normal to the load axis. If a solution is past a limit point, it is not possible to solve for it using the load control method. In the arclength method, the prediction constraint is the length of the prediction vector itself. The Newton corrector then traverses the hyperplane that is perpendicular to the predictor vector toward the equilibrium path. This is the most robust method, able to traverse limit points and turning points in which $\mathbf{K}_t$ is singular and the tangent to the equilibrium path is normal to the displacement axis. In this work the displacement control method is used because typically limit points are the only types of critical points encountered and it makes specifying certain applied displacements to be saved for optimization objective formulations trivial.

In solving nonlinear problems the step size $\Delta\lambda$ is a critical value, especially near critical points where the tangential stiffness changes drastically over a small λ range. In these regions a relatively small step size is necessary or the Newton corrector method could ”blow-up” or get stuck oscillating between two values. However, a smaller step size may not be required for the majority of the solution, where unnecessary λ steps can add to the solution time without improving significantly the accuracy of the solution. As a compromise, an adaptive λ scheme is use based on the number of iterations the previous step took. If the previous step converged to within the specified tolerance in less than n_{max} Newton iterations, $\Delta\lambda$ is doubled for the next step. Likewise, if the previous steps took more than n_{min} iterations to converge, $\Delta\lambda$ is halved for the next step. The number of times that $\Delta\lambda$ can be doubled or halved is specified by the factors lf_{min} and lf_{max} respectively. This allows refinement near difficult areas such as critical points while allowing large steps through easier

sections.

In most nonlinear solution methods, the Newton convergence tolerance tends to be defined by the current residual value normalized by a reference value. This relative convergence scheme allows the user to set a single tolerance value that is non-dimensional and valid for a wide range of problems. However, problems arise when using a relative tolerance for adaptive step size when coupled with saving the state for optimization at specific values of λ. For example, if the last λ step solved for is close to a λ value that needs to be saved for optimization, the prediction for that step may be extremely accurate. If a relative convergence criteria is used, the solution may not be able to be improved to the level specified because the prediction was already almost converged. This will force the Newton solver to continue iterating and it may not be able to converge to the specified tolerance. This will trigger the adaptive step size to be even smaller on the next step, exacerbating the problem. This can be avoided by using an absolute residual convergence tolerance. All the tolerances given in this work are absolute residual values. Care needs to be taken in selecting an absolute tolerance that leads to a well-converged solution. This is studied in Section 3.3.4.

3.2.1 Multiple Statically Stable Solutions

Sometimes in the solution of nonlinear problems two different equilibrium states can be reached for the same boundary conditions. The solution that the solver finds is dependent on the beginning state of that step; it will find the solution that it begins closest to. This multiplicity of solutions may seem similar to a path dependency, which would be counterintuitive as each element in a system is internally conservative. Indeed, if every node position is prescribed, the same forces arise independent of the path that the nodes took to reach the prescribed configuration. However, typically only some boundary nodes in a system have prescribed displacements or forces, allowing possibly multiple stable equilibria to exist, even in conservative nonlinear systems such as those that include Inter elements. This can be demonstrated with a simple example, shown in Figure 3.10. This example is a simplified model of one object being pushed into another with an adhesive

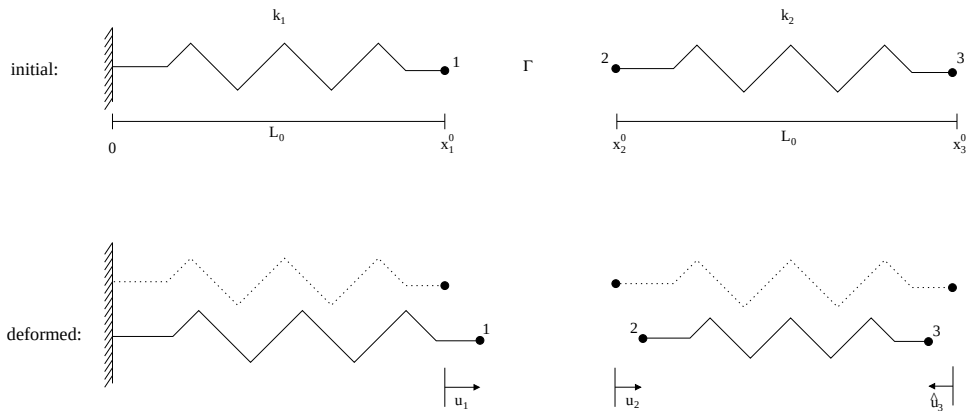

Figure 3.10: Diagram of multiple stable equilibria example problem. Initial and deformed states are shown. There is an adhesive field between points 1 and 2. Initial position and displacement of point 3 are prescribed.

force between the two, such as the cylinder example detailed in Section 3.4. Here one linear spring is pushed into another by specifying an initial undeformed position for point 3 (x_3^0) and a prescribed displacement for the same node ($\hat{u}_3$). Displacements u_1 and u_2 are the degrees of freedom. There exists a nonlinear adhesive function between points 1 and 2, modeled with the Lennard-Jones equation. It is important to note that since the problem is one-dimensional, the contact area between points 1 and 2 is constant and assumed to be 1. The units of Γ are reduced to energy instead of energy per area.

Equilibrium states of the system for a given x_3^0 and $\hat{u}_3$ occur when the potential energy of the system, U, is at a local minimum. The potential energy of the system can be expressed

$$U(u_1,u_2) = U_S + U_A \tag{3.41}$$

where U_S is the potential energy of the linear springs and U_A is the energy stored in the adhesive field between points 1 and 2. The energy in the springs is a function of the deformation of the springs from their undeformed length, L_0. It is assumed that both springs have the same undeformed length and that in the initial state the springs are undeformed, such that $x_1^0 = L_0$ and $x_2^0 = x_3^0 - L_0$. The energy stored in the springs is therefore

$$U_S(u_1,u_2) = \frac{1}{2}k_1u_1^2 + \frac{1}{2}k_2\left(u_2+\hat{u}_3\right)^2. \tag{3.42}$$

The energy in the adhesive field can be expressed

$$U_A(g(u_1,u_2)) = S(g) = \int_0^g \sigma dg \tag{3.43}$$

from Equations 3.16 and 3.17, assuming contact area is constant and equal to 1. Here, the gap g is

$$g(u_1,u_2) = x_2^0 - x_1^0 + u_2 - u_1 = x_3^0 - 2L_0 + u_2 - u_1. \tag{3.44}$$

Substituting the Lennard-Jones model for σ from Equation 3.8, U_A can be expressed

$$U_A(g) = \frac{8b\Gamma}{3}\left[\int_0^g \frac{1}{(bg+1)^3}dg - \int_0^g \frac{1}{(bg+1)^9}dg\right] \tag{3.45}$$

$$U_A(g) = \Gamma\left[\frac{1}{3(bg+1)^8} - \frac{4}{3(bg+1)^2} + 1\right], \tag{3.46}$$

where b, defined in Equation 3.10, is proportional to the inverse of the gap that corresponds to the maximum adhesive force, g_m, and has units of inverse length.

Stable equilibria will occur either at critical points of U or where $g = 0$, since negative g corresponds to penetration which is not admissible. Critical points of U occur where

$$\frac{\partial U}{\partial u_1} = \frac{\partial U}{\partial u_2} = 0. \tag{3.47}$$

variable	value
k_1	4
k_2	100
x_3^0	4
$\hat{u}_3$	1
Γ	2
b	2
L_0	1

Table 3.1: Parameters in spring problem

Differentiating Equation 3.41,

$$\frac{\partial U}{\partial u_1} = \frac{\partial U_S}{\partial u_1} + \frac{dU_A}{dg}\frac{\partial g}{\partial u_1} = \frac{\partial U_S}{\partial u_1} - \frac{dU_A}{dg} \tag{3.48}$$

$$\frac{\partial U}{\partial u_2} = \frac{\partial U_S}{\partial u_2} + \frac{dU_A}{dg}\frac{\partial g}{\partial u_2} = \frac{\partial U_S}{\partial u_2} + \frac{dU_A}{dg}. \tag{3.49}$$

Setting these to zero and summing,

$$0 = \frac{\partial U_S}{\partial u_1} + \frac{\partial U_S}{\partial u_2}. \tag{3.50}$$

Differentiating Equation 3.42,

$$\frac{\partial U_S}{\partial u_1} = k_1 u_1 \tag{3.51}$$

$$\frac{\partial U_S}{\partial u_2} = k_2(u_2 + \hat{u}_3). \tag{3.52}$$

Substituting back into Equation 3.50, the following relation between u_1 and u_2 at a critical point of U is obtained:

$$u_2 = -\frac{k_1}{k_2}u_1 - \hat{u}_3. \tag{3.53}$$

Equation 3.53 has several implications. At all critical points of U, (u_1^*, u_2^*), u_2^* is a linear function of u_1^*. This means that for each critical u_2^* there is a unique u_1^*, and the problem can be reduced to a single degree of freedom. Furthermore, in the three-dimensional u_1-u_2-U space, all critical points of the surface U are along the intersection with the vertical plane defined by Equation 3.53. Figure 3.11 shows a contour plot of the potential energy of the system U as a function of u_1 and u_2 for the values in Table 3.1. For these parameters there are two local minima of U in the admissible ranges for u_1 and u_2, implying two different stable equilibria for the same $\hat{u}_3$.

Since all critical points of U intersect Equation 3.53 and that equation is linear, we can effectively reduce the problem to one degree of freedom. Substituting Equation 3.53, U becomes

$$U^*(u_1) = U_S^*(u_1) + U_A(g^*(u_1)) \tag{3.54}$$

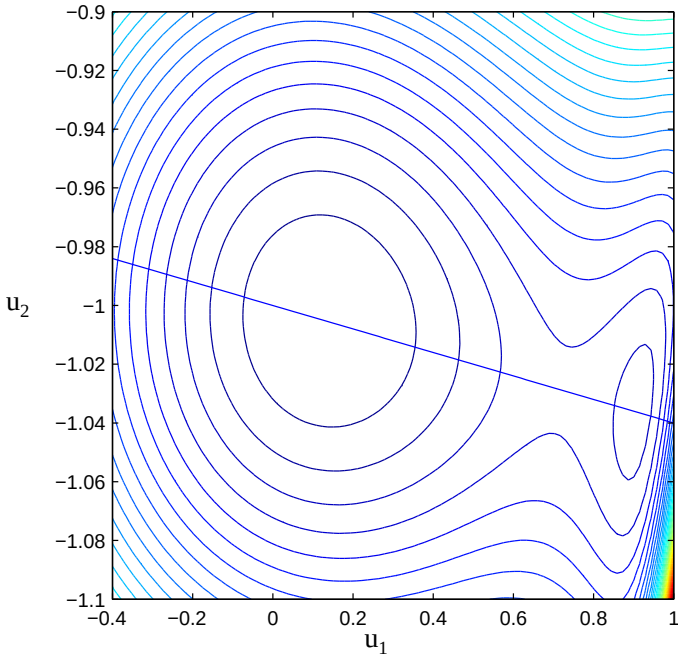

Figure 3.11: Contour plot of U for spring system as a function of u_1 and u_2, with Equation 3.53 overlaid. All critical points of U lie on the line. There are two local minima and one saddle point in the range shown.

where

$$U_S^* = \frac{1}{2}k_1 u_1^2 \left(1 + \frac{k_1}{k_2}\right) \tag{3.55}$$

$$g^* = x_3^0 - \hat{u}_3 - 2L_0 - u_1 \left(1 + \frac{k_1}{k_2}\right). \tag{3.56}$$

As a final step, the problem can be non-dimensionalized by scaling U^* by $\frac{1}{k_1 L_0^2}$. Scaling a function by a constant does not change the location of its critical points. Non-dimensional terms

are denoted by bars:

$$\begin{aligned}
\bar{b} &= bL_0 \\
\bar{u_1} &= \frac{u_1}{L_0} \\
\bar{u_3} &= \frac{\hat{u}_3}{L_0} \\
\bar{k} &= \frac{k_1}{k_2} \\
\bar{x_3^0} &= \frac{x_3^0}{L_0} \\
\bar{\Gamma} &= \frac{\Gamma}{k_1 L_0^2} \\
\bar{g} &= \frac{g^*}{L_0} = \bar{x_3^0} - 2 - \bar{u_3} - \left(\bar{k}+1\right)\bar{u_1} \\
\bar{U_S} &= \frac{1}{2}\bar{u_1^2}(1+\bar{k}) \\
\bar{U_A} &= \bar{\Gamma}\left[\frac{1}{3(b\bar{g}+1)^8} - \frac{4}{3(b\bar{g}+1)^2} + 1\right] \\
\bar{U} &= \frac{U^*}{k_1 L_0^2} = \bar{U_S} + \bar{U_A}.
\end{aligned} \tag{3.57}$$

Figure 3.12 shows $\bar{U}$ plotted against $\bar{u_1}$ at various non-dimensionalized displacement values of point 3. In each case, only admissible values of $\bar{u_1}$ are plotted; larger values of $\bar{u_1}$ than those plotted in each graph would correspond to an inadmissible negative gap between points 1 and 2. The path that a displacement controlled nonlinear solver would take, starting from $\bar{u_3} = 0.6$, increasing to 1.6 and returning to 0.6 is shown. The solver would find the local minimum of $\bar{U}$ at each λ ($\hat{u}_3$) step, starting at the equilibrium $\bar{u_1^*}$ from the previous step and using the gradient there in the current step for the search direction. At $\bar{u_3} = 1.1$, the solver finds different stable equilibria based on which direction that step is approached from, creating an apparent path dependency. Also, local minima can "disappear" between λ steps, making the distance to the next stable equilibrium relatively large. This can cause problems in a real numerical solver in a problem with more degrees of freedom. Another potential problem, not shown in Figure 3.12, is "flip-flopping" between two stable equilibria if they are too close together relative to the Newton step size. These problems combined can make some adhesive problems nearly unsolvable, as shown in Section 3.4.

3.3 Beam Delamination Example

A simple example problem is presented that has an analytical solution to which numerical results can be compared. In this problem, a beam begins fully adhered to a rigid substrate. A vertical displacement u_t is applied to the tip of the beam while the angle of beam at the tip is fixed at zero,

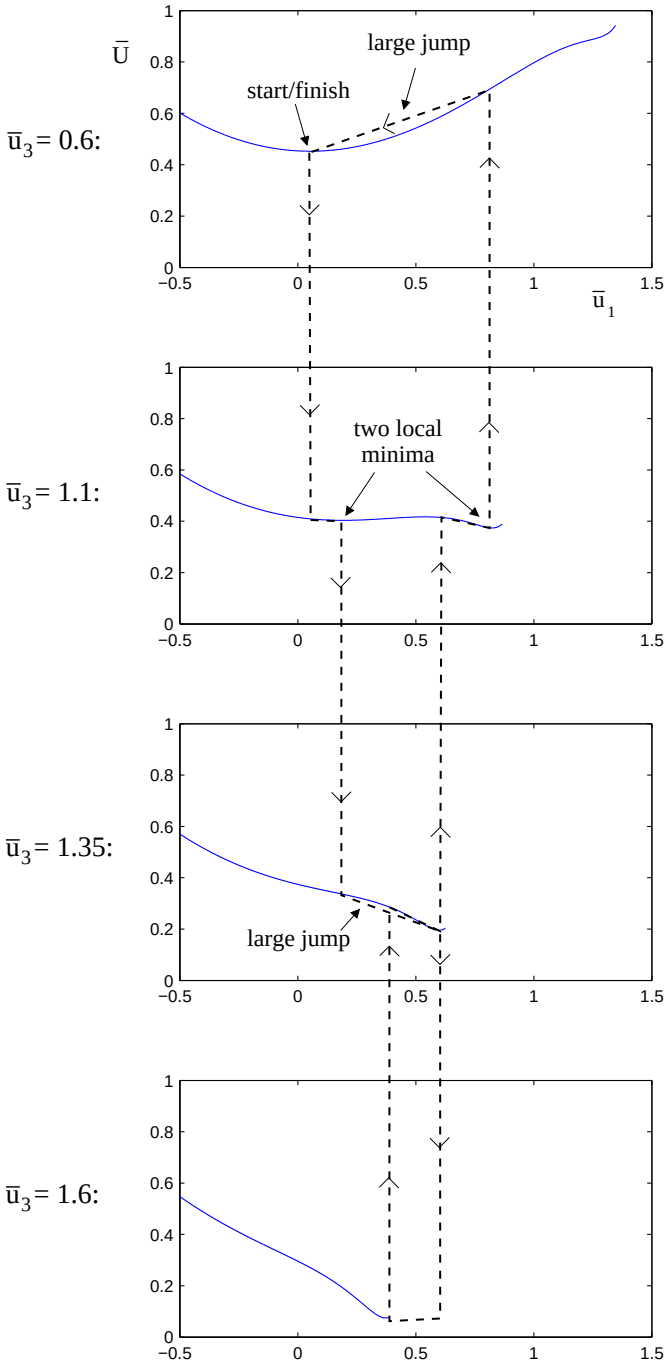

Figure 3.12: Progression of displacement controlled nonlinear solver finding stable equilibria of the spring system as $\bar{u_3}$ is increased from 0.6 to 1.6 and back. Solver finds different stable equilibrium at $\bar{u_3} = 1.1$ depending on which direction that displacement is approached from.

as shown in Figure 3.13. As the gap between the beam tip and the substrate grows, the tip force

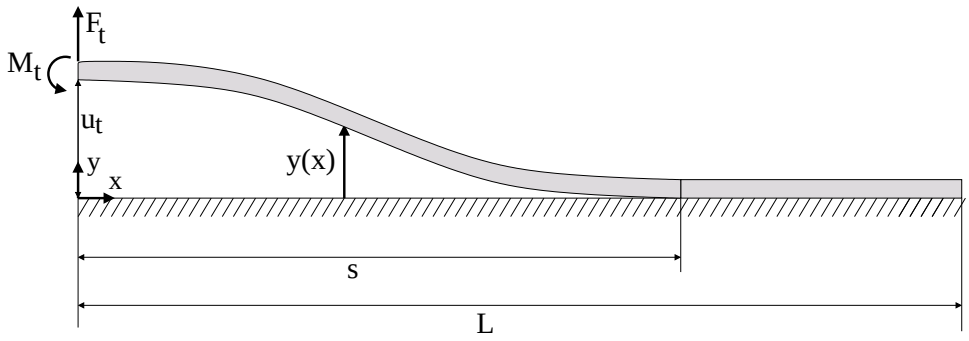

Figure 3.13: Diagram of beam example delamination problem

increases until a crack begins to form and propagates along the space between the beam and the substrate. Analytically this crack length is represented as s, while numerically the crack length is determined by the number of Inter elements with a gap larger than some critical value, usually g_m for the Lennard-Jones model or u_1 for the triangular model. Nominal values for all the problem parameters are given in Table 3.2

In the following sections the analytical solution is derived and then a series of case studies where various problem or numerical parameters are varied, demonstrating the envelope of responses that are possible and verifying the accuracy of the three Inter element models. With the exception of the parameter under study, all other parameters take the nominal value given in Table 3.2. Additionally the triangular model is the default adhesive force per area function with a linear contact penalty function, a spooles solver is used for solving systems of equations, the beam is discretized by 1200 beam elements with InterBeam elements connecting to the substrate and 6 Gauss points per InterBeam element is used for numerical integration.

3.3.1 Analytical Solution

For this problem an analytical solution can be obtained. A simplification is made that no adhesive force acts on the delaminated section of the beam and that the adhered section acts as though clamped. The delaminated portion of the beam can then be modeled as shown in Figure 3.14 with the following boundary conditions:

$$y'(0) = 0 \tag{3.58}$$
$$y'(s) = 0 \tag{3.59}$$
$$y(0) = u_t \tag{3.60}$$
$$y(s) = 0. \tag{3.61}$$

Summing moments in the free body diagram in Figure 3.14 yields

$$M(x) = F_t x - M_t \tag{3.62}$$

variable	value	description
w	$8\,\mu m$	beam width
t_t	$2\,\mu m$	beam thickness
t_b	$2\,\mu m$	substrate thickness
A	$1.6\times10^{-11}\,m^2$	beam cross-sectional area
E	$1.6\times10^{11}\,Pa$	beam Young's modulus
I	$5.333\times10^{-24}\,m^4$	beam moment of inertia
L	$800\,\mu m$	beam length
u_t	$2\,\mu m$	vertical beam tip displacement
m	1200	elements per beam
Γ	$100\,\frac{\mu J}{m^2}$	adhesion energy per area
u_1	$1\times10^{-8}\,m$	triangular first critical gap
u_2	$2\times10^{-8}\,m$	triangular second critical gap
c	$1\times10^{16}\,\frac{N}{m^3}$	contact penetration penalty
tol	1×10^{-8}	absolute residual convergence tolerance
λ_0	0.002	initial λ for nonlinear solver
$\Delta\lambda_0$	0.002	initial λ step size
lf_{min}	3	minimum $\Delta\lambda$ multiplication factor
lf_{max}	5	maximum $\Delta\lambda$ multiplication factor
n_{min}	20	minimum iterations for $\Delta\lambda$ factor decrease
n_{max}	5	maximum iterations for $\Delta\lambda$ factor increase

Table 3.2: Nominal values for the parameters in the beam example problem

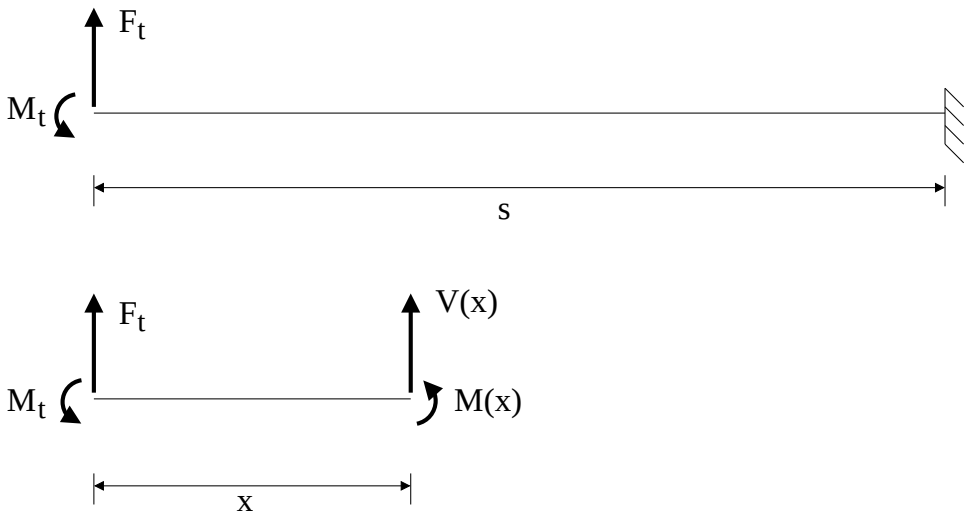

Figure 3.14: Free body diagram of delaminated section of beam example. Lower diagram includes shear force and moment exposed by a cut

and from basic beam theory,

$$EIy'' = M. \tag{3.63}$$

Substituting Equation 3.62 and integrating,

$$\begin{aligned} EIy'' &= F_t x - M_t \\ EIy' &= \frac{1}{2}F_t x^2 - M_t x + c_1. \end{aligned} \tag{3.64}$$

Substituting Boundary Condition 3.58 yields $c_1 = 0$. Substituting Boundary Condition 3.59 gives a relation between crack length, tip force and tip moment:

$$M_t = \frac{1}{2}F_t s. \tag{3.65}$$

Integrating Equation 3.64,

$$EIy = \frac{1}{6}F_t x^3 - \frac{1}{2}M_t x^2 + c_2 \tag{3.66}$$

Substituting Boundary Condition 3.60 yields $c_2 = EIu_t$. Substituting Boundary Condition 3.61 and Equation 3.65 yields a relation between crack length, tip force and tip displacement.

$$\begin{aligned} 0 &= \frac{1}{6}F_t s^3 - \frac{1}{2}M_t s^2 + EIu_t \\ EIu_t &= \frac{1}{12}F_t s^3 \\ F_t &= \frac{12EI}{s^3}u_t \end{aligned} \tag{3.67}$$

Using this expression it is possible to express the beam shape $y(x)$ in terms of crack length and tip displacement.

$$\begin{aligned} EIy &= F_t\left[\frac{1}{6}x^3 - \frac{1}{4}sx^2\right] + EIu_t \\ y &= u_t\left[\frac{12}{s^3}\left(\frac{1}{6}x^3 - \frac{1}{4}sx^2\right) + 1\right] \\ y &= u_t\left(2\frac{x^3}{s^3} - 3\frac{x^2}{s^2} + 1\right) \end{aligned} \tag{3.68}$$

In order to express the crack length in terms of the adhesion energy per area, Γ, the strain energy rate of the beam needs to be formulated. From beam theory, the strain energy density W is a function of the stress,

$$\begin{aligned} \sigma_x &= \frac{My}{I} \\ W &= \frac{\sigma_x^2}{2E} = \frac{M^2y^2}{2EI^2}. \end{aligned} \tag{3.69}$$

The strain energy of the beam U is the strain energy density integrated over the beam cross-sectional area and the length

$$\begin{aligned} U &= \int_0^s \iint_A W\,dA\,dx \\ &= \int_0^s \frac{M^2}{2EI^2} \iint_A y^2\,dA\,dx \\ &= \int_0^s \frac{M^2}{2EI} dx \\ U &= \frac{1}{2EI}\int_0^s M^2\,dx \end{aligned} \tag{3.70}$$

The term M^2 is expressed in terms of crack length and tip displacement by substituting Equations 3.65 and 3.67 into Equation 3.62

$$\begin{aligned} M &= F_t\left(x-\frac{1}{2}s\right) \\ M^2 &= \frac{12^2E^2I^2u_t^2}{s^6}\left(x^2-sx+\frac{1}{4}s^2\right) \end{aligned}$$

Substituting into Equation 3.70,

$$\begin{aligned} U &= \frac{1}{2EI}\frac{12^2E^2I^2u_t^2}{s^6}\int_0^s\left(x^2-sx+\frac{1}{4}s^2\right)dx \\ &= \frac{6\cdot 12EIu_t^2}{s^6}\left[\frac{1}{3}s^3-\frac{1}{2}s^3+\frac{1}{4}s^3\right] \\ U &= \frac{6EIu_t^2}{s^3} \end{aligned} \tag{3.71}$$

The beam/adhesive system will be in equilibrium when the energy released when increasing the delaminated area by an infinitesimal amount is equal to the energy of adhesion per area,

$$\begin{aligned} \Gamma &= -\frac{dU}{dA} = -\frac{dU}{wds} \\ &= \frac{18EIu_t^2}{ws^4} \\ s &= \left(\frac{18EIu_t^2}{w\Gamma}\right)^{\frac{1}{4}} \end{aligned} \tag{3.72}$$

where w is the beam width. Substituting $I=\frac{wt^3}{12}$,

$$s=\left(\frac{3Et^3u_t^2}{2\Gamma}\right)^{\frac{1}{4}} \tag{3.73}$$

where t is the beam thickness. Substituting this back into Equation 3.68 yields an equation for the beam shape y in terms of the tip displacement u_t and the energy of adhesion per area Γ. This equation is used as the baseline to compare numerical results. An example is in Figure 3.16.

3.3.2 Element Model Study

The first study we look at is modeling the beam using either beam, four-node quadrilaterals, or three-node shell elements. In the case of beam elements, the upper delaminating beam was discretized into 1200 elements. Displacements at all degrees of freedom of the lower substrate beam were set to zero, as well as those of the right-most node of the upper beam. A displacement of $2 \times 10^{-6} m$ in the y-direction was applied to the leftmost node of the upper beam, and all other degrees of freedom were left free.

In the case of shell elements, the upper beam was discretized in 2400 triangular elements in a pattern shown in Figure 3.15 This discretization preserved the x-length of the elements from the

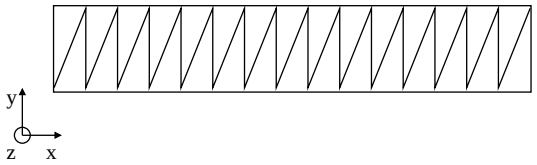

Figure 3.15: Sketch of beam discretization pattern for three-node triangular shell elements, top-down view

beam element discretization. In this case the tip displacement is in the z-direction, out of the page as shown in Figure 3.15. Again, displacements in all degrees of freedom of the substrate beam were restricted to zero, as well as at the rightmost two nodes of the upper delaminating beam.

Several meshes were studied for quadrilateral elements. In general, the converged shape of the beam discretized with quadrilaterals matched the least well with the analytical solution. This is most likely due to not having rotational degrees of freedom and the linear as opposed to cubic shape functions. The mesh that was the best compromise between accuracy and computation time was 2400 elements in the x-direction and 4 in the y-direction. As in the beam element case, beam tip displacement is in the y-direction. It is important to note that the element length in the x-direction is twice as small as in the beam and shell element cases.

Figure 3.16 shows numerical results for the delaminated beam shape using different element types to discretize the beam, compared to the analytical solution. In some cases, the upper beam is clamped at the analytically computed crack tip and the adhesive energy of the Inter elements is set to zero. The clamped beam and shell element discretizations are nearly indistinguishable from the analytical solution. Figure 3.17 shows the difference between the different examples and the analytical solution. The clamped quadrilateral discretization is less accurate, even though the mesh is twice as dense in the x-direction as the beam and shell cases. This is especially evident in the region between the beam tip and the crack tip. In the remaining cases the adhesion energy

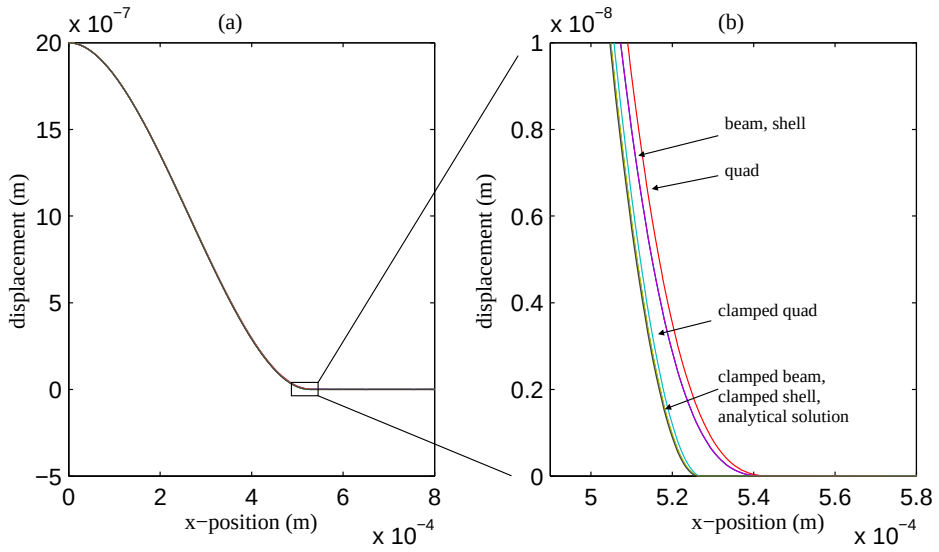

Figure 3.16: Beam deflection example modeled with different element types. (a) Delaminated beam profile (b) Close-up on crack tip area

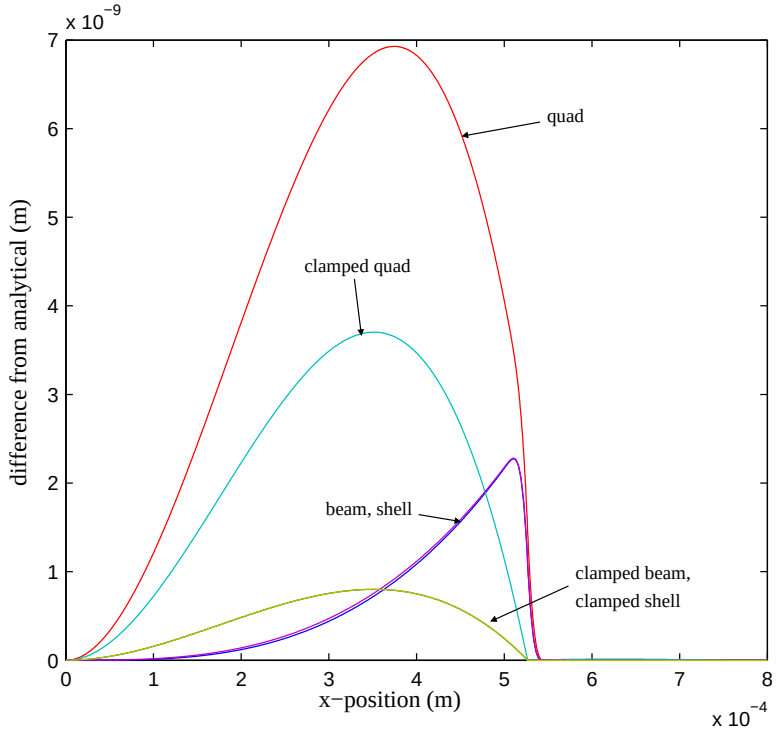

Figure 3.17: Difference between FEM and analytical solutions to beam delamination example along the beam length

in the Inter elements is set to 1×10^{-4} and the upper beam is not clamped at the analytically determined crack tip. The beam and shell element discretizations are nearly indistinguishable, and the quadrilateral element case is slightly worse. All three show a crack tip shifted to the right, indicating a possibly weaker adhesive than calculated analytically. However, this effect is due to the transition between fully "stuck" and fully delaminated regions of the elemental force function, while the analytical case assumed no transition zone. However, the maximum error overall, in the quadrilateral case, was less than $7\,nm$, which is about a third of one percent of the beam thickness.

3.3.3 Adhesion Law Study

Two adhesion laws were implemented, one based on the Lennard-Jones equation and four variations on the triangle law used in all other examples. Figure 3.18 shows the five functions, which all have a corresponding adhesion energy per area (Γ) of $1 \times 10^{-4} \frac{J}{m^2}$. Figure 3.18(a) shows the

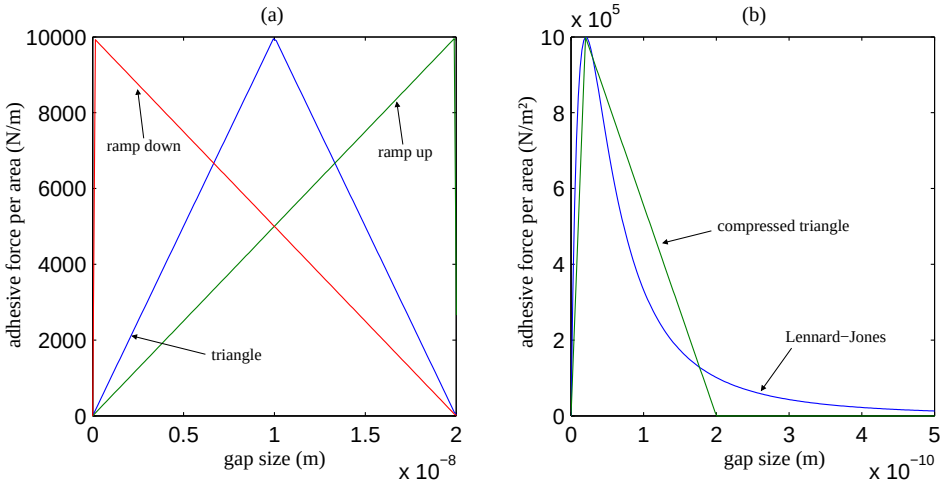

Figure 3.18: Various nonlinear adhesive functions studied. (a) Triangular functions with $u_2 = 2.0 \times 10^{-8}$ (b) Lennard-Jones-style function and a corresponding triangular function

triangular functions "ramp down," "ramp up" and "triangle," which all have the same gap size over which adhesion is active (u_2) in addition to the same Γ. Figure 3.18(b) shows a Lennard-Jones function and a corresponding triangular function that is scaled to similar dimensions. The Lennard-Jones function was scaled so that the penetration penalty would be large enough to allow the same amount of penetration as the other triangular functions. Note the two order of magnitude difference between the scales in the figure.

Figure 3.19 shows the resulting beam profiles for the various adhesion laws. Interestingly, at the crack tip the ramp up and ramp down laws give similar results, but the error over the beam as a whole is much greater for the ramp down case. Also, the Lennard-Jones law gave by far the closest agreement with the analytical solution, while the similar compressed triangle law yielded the poorest results. In fact, the nonlinear solver could not converge to an absolute residual of 1×10^{-8} for the compressed triangle case as it did in all the others, so the tolerance had to be

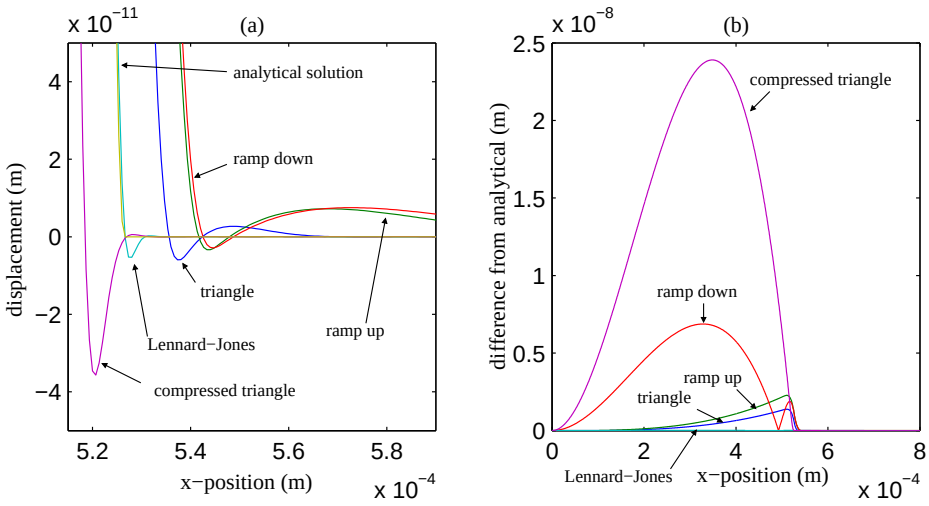

Figure 3.19: Beam delamination with various adhesive force laws. (a) Close-up of crack tip (b) Difference in beam shape from analytical solution

relaxed to 1×10^{-6}. Even with this relaxation, many steps took more than 80 iterations to converge. The convergence issues are most likely due to the sharp C^1 discontinuities in the compressed triangle function. Although the Lennard-Jones function does not have any definitive u_2 point, the vast majority of the adhesive strength is concentrated in a much more narrow range than in the other triangular functions. This accounts for the closer agreement to the analytical solution, which assumes no transition whatsoever from adhered to free.

3.3.4 Convergence Tolerance Study

In any nonlinear analysis the degree to which the force residual, or the norm of the difference between the external and internal forces, converges to zero is an important parameter. If the residual is not required to converge to a small enough value the resulting displacement field can become offset by increasing error at each iteration. However, setting an overly strict convergence tolerance could force the solver into additional iterations that improve a solution that is already adequately converged adding computation time. Also, if the convergence factor is set too low it may be below the range of numerical precision of the machine, in which case the problem would never converge.

Typically nonlinear problems are solved using a relative convergence tolerance, in which the value of the residual is normalized by the residual of the first iteration of a given step. However, this approach was not suitable here because an adaptive step size was employed. In the case of a very small step size the first residual may be already well converged, in which case a relative drop in the residual of several orders of magnitude may not be possible. Extremely small step sizes may occur when solving an optimization problem, especially when the optimization criteria are dependent on variables at specified nonlinear steps. Figure 3.20 shows the baseline beam delamination problem run with various absolute convergence tolerances. The solutions when converged to a tolerance of

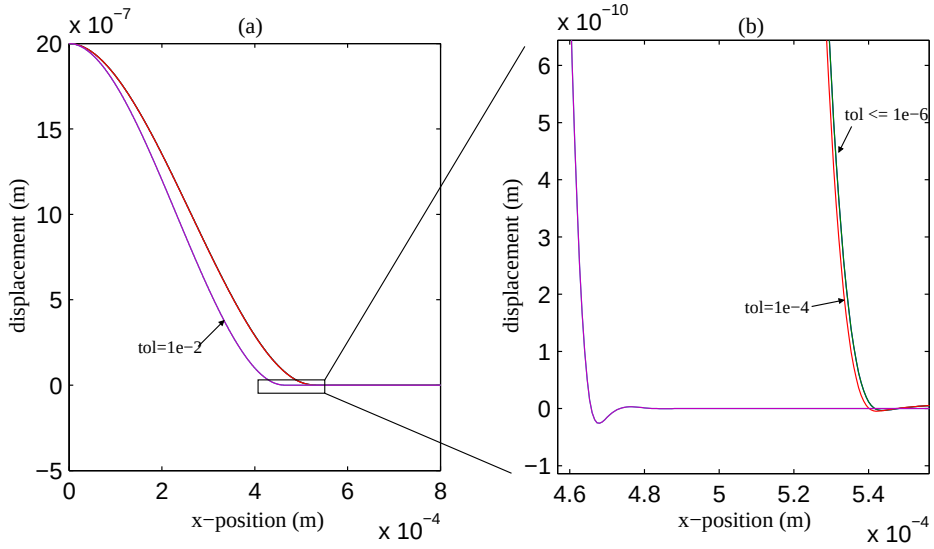

Figure 3.20: (a) Beam delamination with various residual convergence tolerances (b) Close-up

1×10^{-6}, 1×10^{-8} and 1×10^{-10} were identical. Differences appeared when the tolerance was 1×10^{-4}, and the solution with a tolerance of 1×10^{-2} was significantly different.

3.3.5 Penetration Penalty Study

In the Inter elements, contact is implemented through a penalty method by treating it as a material nonlinearity. Although this method is much easier to implement than a Lagrange multiplier method which would require modifying the solver itself, it has drawbacks including severe material nonlinearities and penetration. Figure 3.21 shows solutions to the beam problem with various penetration penalty factors. These factors correspond to the slope of the contact portion of the adhesion law described earlier. For this problem, a penalty factor of $1 \times 10^{10} \frac{N}{m^3}$ is inadequate, leading to extreme penetration of the upper beam into the substrate. A penalty factor of $1 \times 10^{16} \frac{N}{m^3}$ leads to very little penetration, on the order of $1\,nm$, while larger penalty factors lead to increased numerical problems in solving.

The penalty factor is not non-dimensionalized due to the lack of a stable reference value to normalize it against. In optimization, if the energy of adhesion of the elements are the optimization variables then the obvious choice for normalization, the slope of the adhesive σ curve, is variable for each element in the structure. In elements that have small adhesive energies the contact penalty would also be small, allowing more penetration in these regions. An acceptable penalty factor must be found for each new problem for this reason; the value used in the beam delamination problem will not work globally.

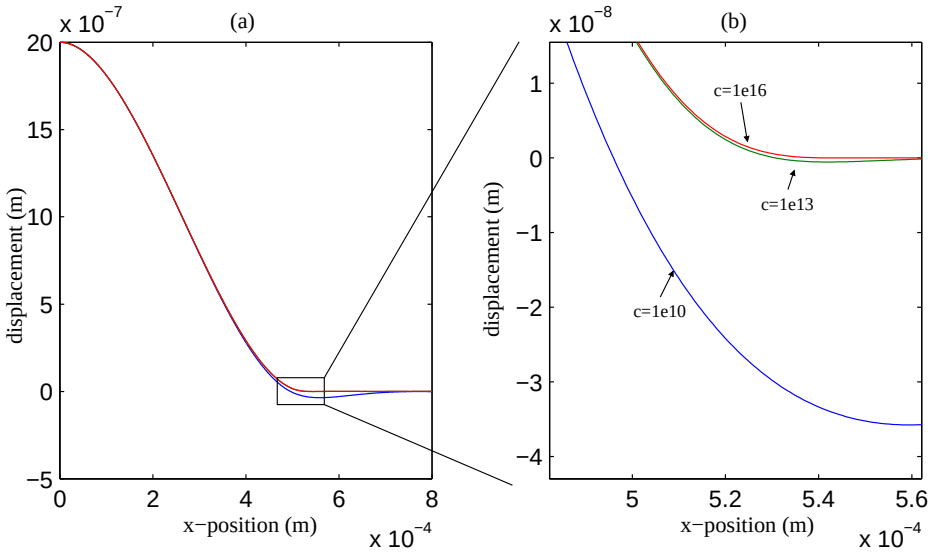

Figure 3.21: (a) Beam delamination with various contact penalty factors (b) Close-up

3.3.6 Gauss Point Study

One variable in the Inter element formulation is the number of Gauss points used in the integration approximations for the internal force vector and tangential stiffness matrix. These approximations for the InterBeam element are in Equations 3.20 and 3.21. Figure 3.22 shows the difference between the shapes of the analytical solution and numerical solution using 1-point, 3-point and 6-point Gauss integration rules. The differences between the solutions are nearly negligible. How-

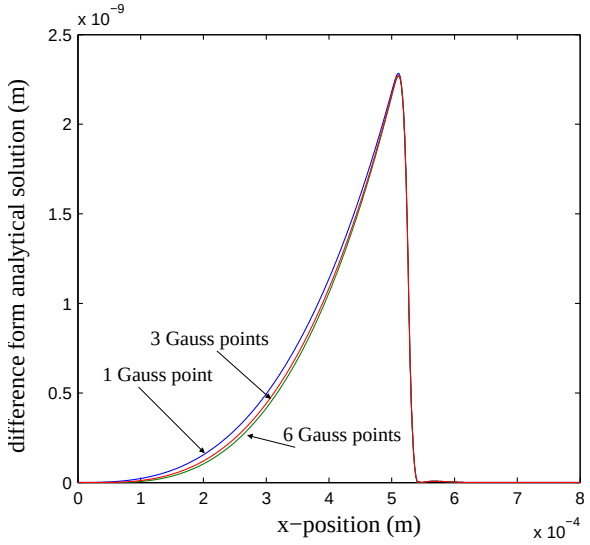

Figure 3.22: Effect of Gauss point integration rule on results. Difference between solution with various Gauss points and the analytical solution is shown.

ever, the numerical statistics in arriving at these solutions shown in Table 3.3 are more telling: For

Gauss point rule	max iterations per λ step	average iterations per λ step
6	13	6.0268
3	12	**7.2362**
1	**71**	6.6727

Table 3.3: Statistics from the numerical analysis in the Gauss integration rule study

one Gauss point per element the solver had trouble converging in some steps. This becomes especially problematic if used for optimization, which may create adhesive patterns along the beam which cause additional convergence problems. The three-point rule did not have any steps where convergence was difficult, but the solver took the least number of steps using the six-point rule.

3.3.7 Mesh Refinement Study

Another important parameter in any finite element analysis is the mesh discretization size. Typically in finite element analysis a finer mesh results in a more accurate solution at the expense of computation time. Five discretizations are presented here. In the 1200 element case, for example, the beam and substrate are each discretized into 1200 elements with 1200 InterBeam elements connecting them for a total of 3600 elements. Figure 3.23 shows that even the most coarse discretization yields a relatively close match to the analytical solution with a maximum error in the beam shape of less than $4\,nm$. However, the coarser discretizations did not always yield the fastest

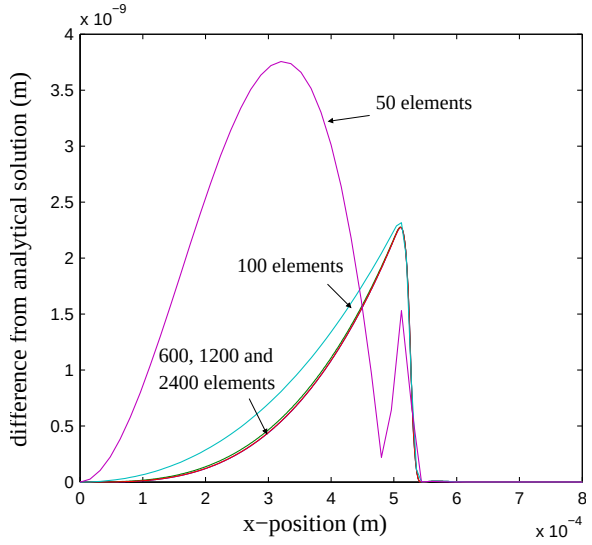

Figure 3.23: Difference between numerical solutions with various mesh refinement levels and the analytical solution of Section 3.3.1

run time. Table 3.4 shows that nonlinearities began giving the solver convergence problems for discretizations of 100 and 50 elements per beam. The convergence issues with more coarse dis-

InterBeam elements	max iter/step	average iter/step	total run time (s)
50	$>$ **110**	24.616	$\mathbf{2.26 \times 10^3}$
100	$>$ **110**	17.749	3.82×10^2
600	13	6.045	1.89×10^2
1200	13	6.0268	3.86×10^2
2400	13	6.0357	8.03×10^2

Table 3.4: Statistics from the numerical analysis in the mesh refinement study

cretizations also become more problematic with varying adhesive strength topologies that arise from optimization.

3.3.8 Adhesion Energy Study

Figure 3.24 shows the beam response as the energy of adhesion, Γ, is varied between 1×10^{-5} and 1×10^{-3}. Fig. 3.24(a) shows the nodal force vs. the displacement at the tip of the beam. In

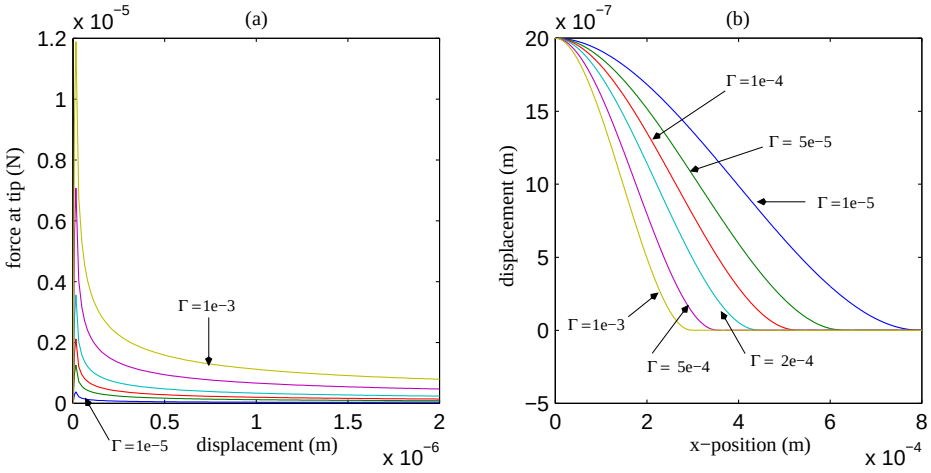

Figure 3.24: Beam delamination example over a range of adhesion energies Γ. (a) Force at beam tip for given tip displacements (b) Beam shape profile for a tip deflection of $2\,\mu m$

Chapter 4 the distribution of adhesive energy along the beam will be optimized to meet a given tip force/displacement objective. The adhesion energy in each block of four elements along the beam will be free to vary between 1×10^{-12} (effectively zero) and $1 \times 10^{-3}\,J/m^2$. The plot of tip force vs. displacement in Figure 3.24(a) serves as an envelope for all possible solutions. If an objective point is outside the curve labeled $\Gamma = 1 \times 10^{-3}$, it is not reachable given the constraints on the design variable Γ. Figure 3.24(b) shows the final beam profiles for various adhesive energies for a $2\,\mu m$ tip displacement.

3.3.9 Beam Stiffness Study

The response of the system to changing the Young's modulus of the beam, shown in Figure 3.25, is extremely similar to the response of changing the energy of adhesion per area (Figure 3.24). In the

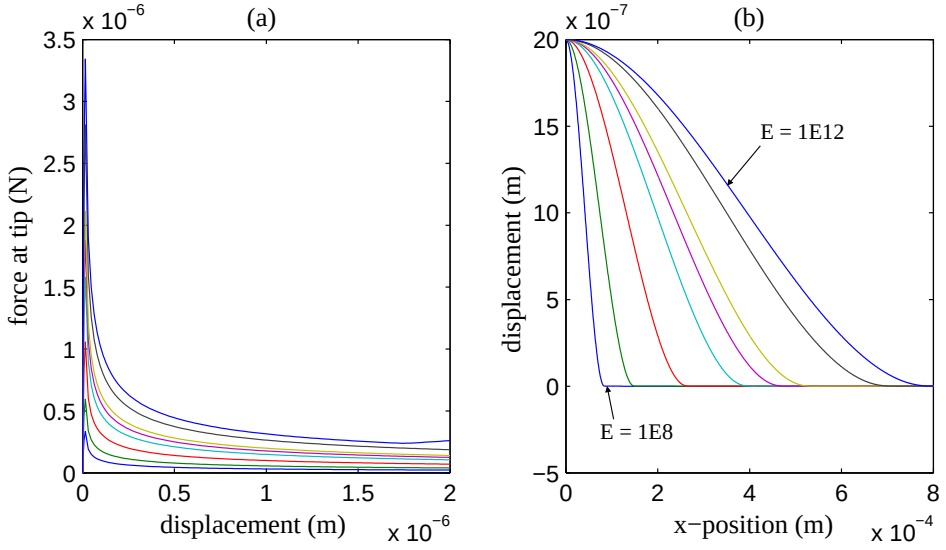

Figure 3.25: Beam delamination example over a range of beam Young's moduli. (a) Force at beam tip for given tip displacements (b) Beam shape profile for a tip deflection of $2\,\mu m$

analytical solution, Equation 3.73 shows that increasing the Young's modulus E and decreasing the energy of adhesion per area Γ increases the crack length s by the same factor. One important note is that as either Γ became large or E became small the solver had more difficulty converging in some steps. This difficulty arose due to the region ahead of the crack tip in which there is strong adhesion (the cohesive zone) shrinking to act within a single Inter element. This can be mitigated by switching to finer mesh densities. The ratio between E and Γ also is important in the following example.

3.4 Hertz/JKR Cylinder Example

While the beam delamination example was chosen because it has an easily computed analytical solution, this example of a cylinder in adhesive contact with a rigid substrate was selected because it is derived from one of the most exhaustively studied problems in the field of adhesive contact mechanics. The problem of contacting spheres was first studied in the 19th century by Hertz, as described in Chapter 2, and modified to include adhesion by Johnson, Kendall and Roberts (JKR) and Derjaguin, Muller and Toporov (DMT). In JKR theory the contact area increases due to adhesive forces but there is no cohesive zone outside of the contact area where adhesive forces act. This model is valid for very flexible smooth materials such as rubber. The DMT theory the contact area does not increase due to the adhesive forces but forces act in a cohesive zone ring outside the contact area. This model holds for very rigid structures.

The classical model for spheres was reformulated for cylinders with quadratic shape profiles in contact by Baney and Hui [2]. They model the adhesive force with the Dugdale Model (described in Section 3.1.2.2), which leads to a sharply defined cohesive zone outside the contact area. In this work the triangular model is used instead for ease in numerical solution. A factor λ is defined as a function of the cylinder Young's modulus, Poisson's ratio and the energy of adhesion per area. As this factor approaches ∞ the cohesive zone length approaches zero, leading to a JKR-type solution. As λ approaches zero the solution approaches the Hertz solution. Note that for spheres as an analogous λ factor approaches zero the DMT solution is reached. The difference between a 2-D cylinder and 3-D spheres comes from the way that the adhesive force scales with contact lengths.

Figure 3.26 shows the cylinder example problem. In the initial condition the cylinder is in

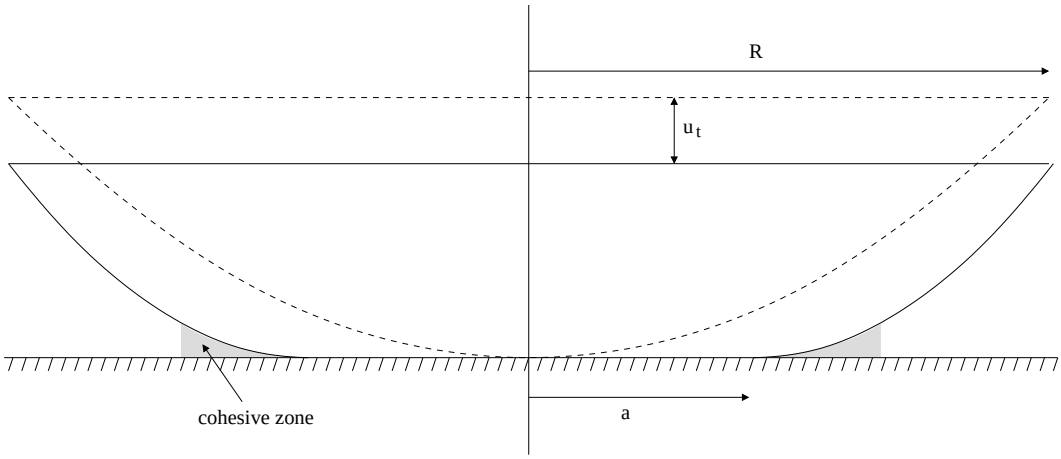

Figure 3.26: Diagram of the cylinder adhesive contact example

contact with the substrate at a single point. A displacement u_t is applied to the top cylinder surface pressing the cylinder into the rigid substrate. A rectangular contact area forms with a length of L, the length of the cylinder, and width $2a$ where a is the contact radius. The undeformed surface of the cylinder is defined to be quadratic, such that

$$y = \frac{1}{2R}x^2 \tag{3.74}$$

where R is the radius of curvature of the cylinder. R is also defined geometrically for this problem in Figure 3.26.

For this problem, the parameters were used are tabulated in Table 3.5. Note that length scales are in the macro range to help reduce numerical issues associated with small length scales.

variable	value	description
E	$1\times10^{6}\,Pa$	cylinder Young's modulus
ν	0.23	cylinder Poisson's ratio
L	$80\,m$	cylinder length
R	$8\,m$	cylinder radius of curvature
a_{max}	$0.8\,m$	maximum contact radius
$\tilde{a}_{max}$	2	maximum normalized contact radius
u_1	$4\times10^{-3}\,m$	triangular first critical gap
u_2	$8\times10^{-3}\,m$	triangular second critical gap
c	$1\times10^{16}\,\frac{N}{m^3}$	contact penetration penalty
tol	1×10^{-4}	absolute residual convergence tolerance

Table 3.5: Nominal values for the parameters in the cylinder example problem

3.4.1 Analytical Solution

Baney and Hui derive an analytical solution that relates a non-dimensionalized force per unit length applied to the top surface of the cylinder, $\tilde{P}$, and a non-dimensionalized contact radius, $\tilde{a}$ [2]:

$$\tilde{P}_{Hertz} = \tilde{a}^2 \tag{3.75}$$

$$\tilde{P}_{JKR} = \tilde{a}^2 - 2\tilde{a}^{\frac{1}{2}} \tag{3.76}$$

where

$$\tilde{P} = \frac{P}{(\pi E^{*}\Gamma^2 R)^{\frac{1}{3}}} \tag{3.77}$$

$$\tilde{a} = \frac{a}{2\left(\frac{R^2\Gamma}{\pi E^{*}}\right)^{\frac{1}{3}}} \tag{3.78}$$

$$P = \frac{f_t}{L}$$

$$E^{*} = \frac{E}{1-\nu^2}$$

and f_t is the sum of forces acting along the top surface of the cylinder and ν is the Poisson's ratio of the cylinder material. A graph showing Equations 3.75 and 3.76 is in Figure 3.30

3.4.2 Contact Area Formulation

In the beam example the crack length s never needs to be explicitly extracted from the numerical solutions because the analytical solution for the entire beam shape was available. In the case of the

cylinder example there is no analytical solution available for the deformed shape of the cylinder surface. The analytical solution instead relates the force along the cylinder top surface to the radius of contact a. This radius needs to be extracted from the numerical solution. For InterBeam and InterQuad elements, the contact radius is the sum of the area per element that is in contact A_c over all the Inter elements divided by the width of the elements (the length of the cylinder, in this case).

The contact area per element A_c is formulated by detecting whether the gap between surfaces is less than a certain value $\bar{g}$, shown in Figure 3.27. This detection is captured by a contact indication

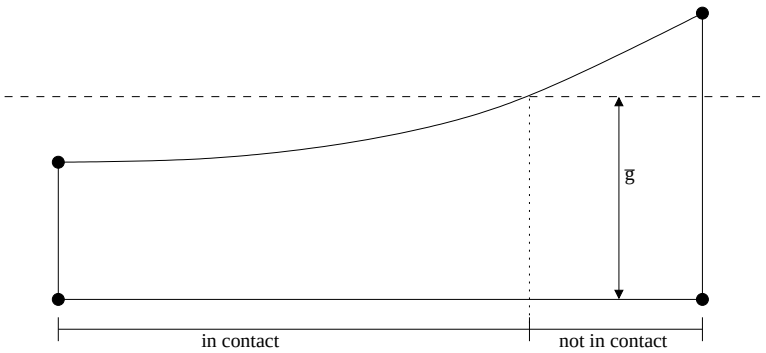

Figure 3.27: An InterQuad element showing partial contact. If the gap is less than the critical gap $\bar{g}$ the part of the element is in contact and the function $\aleph$ is 1. For the rest of the element, the contact indication function $\aleph$ is 0.

function $\aleph$ that takes the value 1 if the gap is smaller than $\bar{g}$, indicating contact, and takes the value 0 if the gap is greater than $\bar{g}$.

The contact indication function $\aleph$ includes a transition gap between complete contact and no contact, making the function C^0 and C^1 continuous, which aids in optimization if contact area is a criterion. The function is defined as

$$\aleph(g) = \begin{cases} 1 & ,g < (1-p)\,\bar{g} \\ \frac{1}{2}\cos\left[\frac{\pi}{2p}\left(\frac{g}{\bar{g}}+p-1\right)\right]+\frac{1}{2} & ,(1-p)\,\bar{g} \le g < (1+p)\,\bar{g} \\ 0 & ,g \ge (1+p)\,\bar{g} \end{cases} \tag{3.79}$$

and is shown graphically in Figure 3.28. p is a fraction of the critical gap $\bar{g}$ that defines the transition zone between complete contact and no contact.

The elemental contact area A_c equals the contact indication function integrated over the element area,

$$A_c = \frac{A}{A_0}\iint_{A_0} \aleph(g)\,dA_0 \tag{3.80}$$

Where A is the deformed elemental area and A_0 is the initial elemental area. For the InterBeam

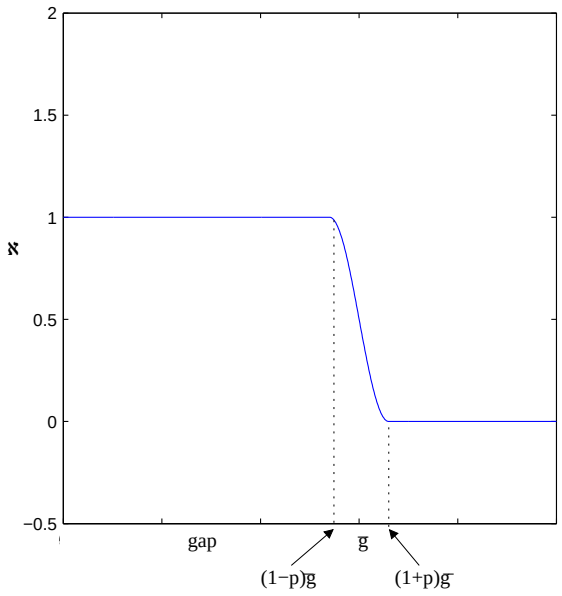

Figure 3.28: The contact indication function א as a function of the gap between surfaces.

and InterQuad elements, this reduces to

$$\begin{aligned} A_c &= w\frac{L}{L_0}\int_0^{L_0} \aleph(g)\,dx \\ &= w\frac{L}{2}\int_{-1}^{1} \aleph(g)\,dx_g \\ &\cong w\frac{L}{2}\sum_i^n w_i \aleph(g_i) \end{aligned} \tag{3.81}$$

where x_g are generalized coordinates defined in Equation 3.22, L is the deformed element length, w_i are Gauss weighting factors, and w is the element width.

3.4.3 Numerical Solution

In this section, the analytical equations for the relation between force per length $\tilde{P}$ and contact radius $\tilde{a}$ are attempted to be matched with finite element analysis. The cylinder domain was discretized into 4-node linear quadrilateral elements and InterQuad elements were placed between the cylinder and the substrate as shown in Figure 3.29. The first $0.8\,m$ in the x-direction of the domain was discretized into 40 InterQuad elements and the remainder, which is never in the cohesive zone, is discretized into 10 InterQuad elements.

The Hertz solution is obtained by setting the energy of adhesion per area Γ to be near-zero. A solution is obtained for a range of top cylinder surface displacements u_t. For each of these solutions, $\tilde{P}$ and $\tilde{a}$ are computed. P is computed by summing the forces at all the nodes along the

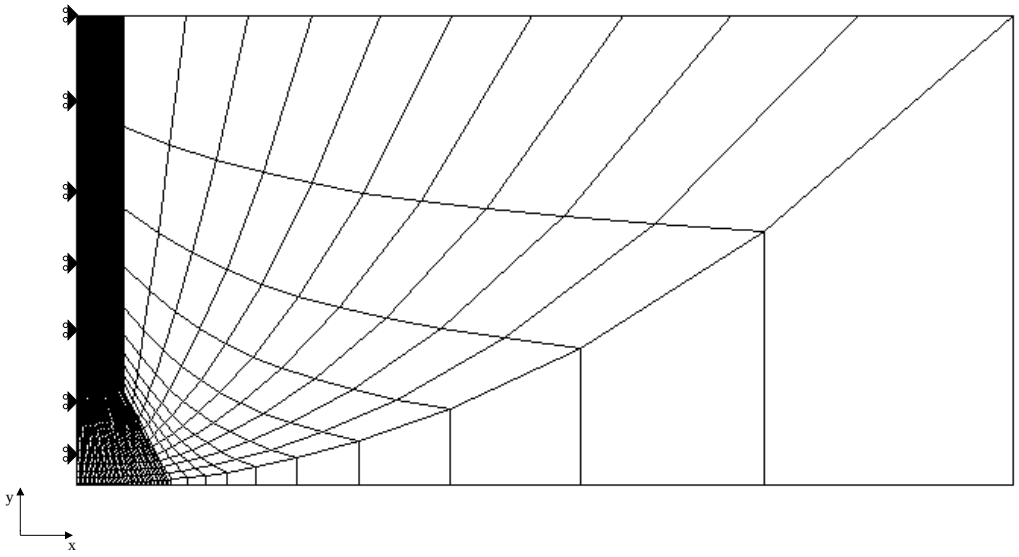

Figure 3.29: Mesh for cylinder example

top surface of the cylinder. a is computed by the method described in Section 3.4.2. These $\tilde{P}-\tilde{a}$ coordinates are plotted against the analytical curve in Figure 3.30. There is generally very close agreement between the numerical and analytical solution.

As the adhesion energy per area Γ is increased, the $\tilde{P}-\tilde{a}$ response gradually shifts from the Hertz solution and approaches the JKR solution if all other variables are kept constant. Baney and Hui define a factor λ to parameterize the transition between the solutions:

$$\lambda = \frac{4\sigma_0}{\left(\frac{\pi^2 E^{*2}\Gamma}{R}\right)^{\frac{1}{3}}} \tag{3.82}$$

where σ_0 is the force per area defined in the Dugdale model,

$$\sigma_0 = \frac{\Gamma}{u_2}$$

from Section 3.1.2.2. Here the triangular model is used instead. σ_0 is redefined as

$$\sigma_0 = \frac{2\Gamma}{u_2} \tag{3.83}$$

which corresponds to the peak force per area in the triangular σ curve shown in Figure 3.4. Sub-

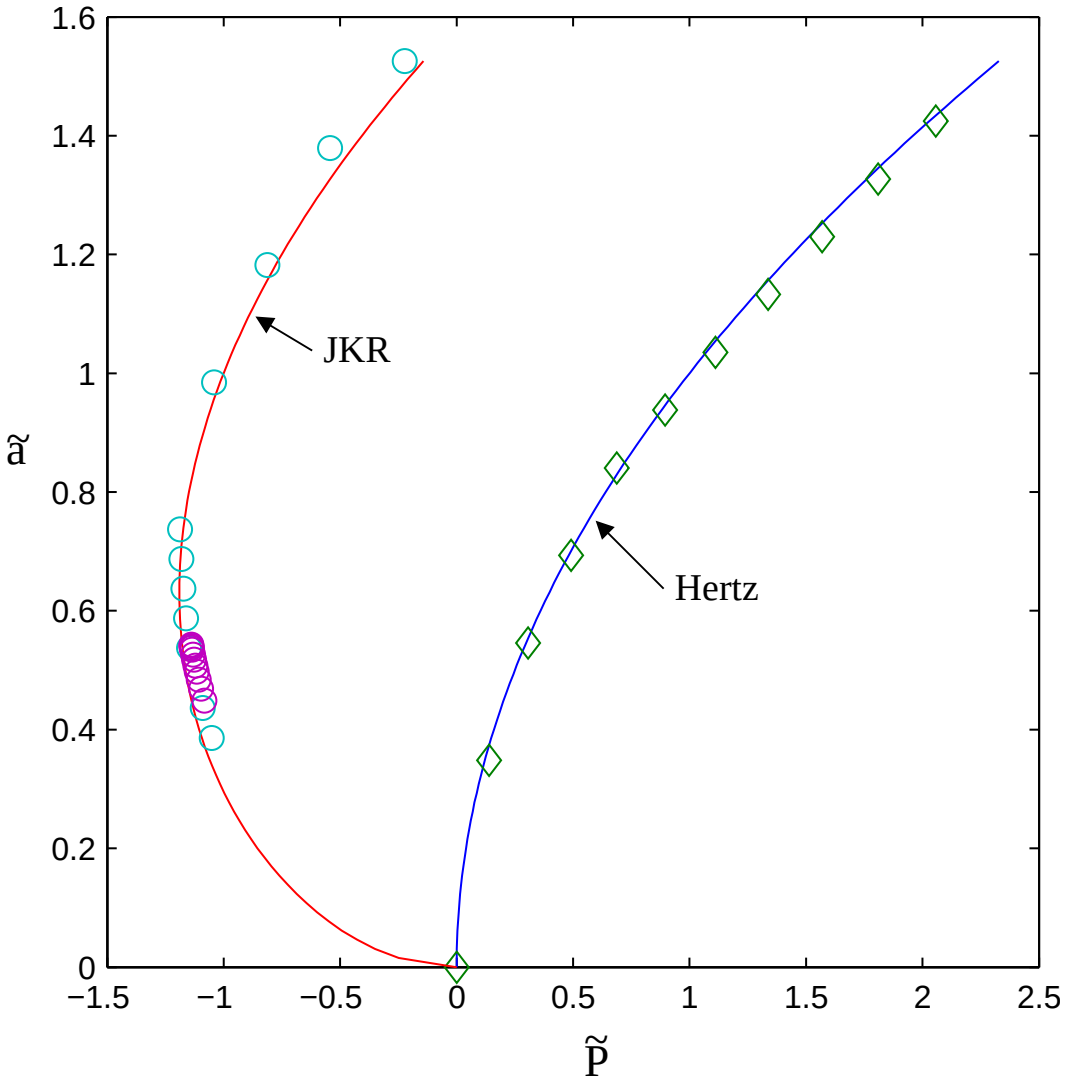

Figure 3.30: The numerical solution of the $\tilde{P} - \tilde{a}$ curves compared to the analytical solution of the JKR and Hertz cases.

λ	Γ
0	0
0.1	1.1727×10^1
1	3.7086×10^1
5	$\mathbf{4.1463 \times 10^2}$
10	1.1727×10^3
100	3.7086×10^4

Table 3.6: Adhesion energy per area values for a range of λ values

stituting Equation 3.83 into Equation 3.82,

$$\begin{aligned} \lambda &= \frac{8\Gamma}{u_2\left(\frac{\pi^2 E^{*2}\Gamma}{R}\right)^{\frac{1}{3}}} \\ &= \frac{8}{u_2}\left(\frac{\Gamma^2 R}{E^{*2}\pi^2}\right)^{\frac{1}{3}} \\ \Gamma &= \frac{E^*\pi}{16}\sqrt{\frac{\lambda^3 u_2^3}{2R}} \end{aligned} \tag{3.84}$$

Table 3.6 gives the adhesion energy per area that corresponds to several different values of λ when substituting values from Table 3.5. According to Baney and Hui [2] the JKR model is roughly valid for $\lambda > 4$. The value $\lambda = 5$ is selected for the numerical analysis of the JKR model. The results are plotted against the analytical solution (Equation 3.76) in Figure 3.30. The numerical and analytical solutions for the JKR and Hertz cases match well, further validating the accuracy of the Inter element discretization and the adhesion/contact models used.

It is important to note that in the case where the JKR curve was matched it was not possible to solve for points less than a certain $\tilde{P}$ value. The reason for this is related to the discussion in Section 3.2.1. Neither $\tilde{P}$ nor $\tilde{a}$ are the control variable. Therefore, for a given displacement of the upper surface of the cylinder there may be multiple $(\tilde{a},\tilde{P})$ stable equilibria points. Additionally, there may be a range of $(\tilde{a},\tilde{P})$ points along the JKR curve for which there is not a stable equilibrium. Attempts were made to find $(\tilde{a},\tilde{P})$ points for small values of $\tilde{P}$ using both a static solver and a quasi-static solver using dynamic relaxation without success.

3.5 Sheet Wrapping Example

While the problems presented up to this point are academically interesting, the following example grows from an actual application of adhesion at small scales. Here a nanotube wraps a thin sheet around itself, forming another layer or wall to the tube. An illustration of this for a carbon nanotube

variable	value	description
r	$4.0 \times 10^{-6} m$	cylinder radius
l	$8.0 \times 10^{-6} m$	cylinder length
g_0	$4.0 \times 10^{-7} m$	initial gap between cylinder and sheet
t	$1.0 \times 10^{-7} m$	sheet thickness
E	$4.0 \times 10^{8} Pa$	sheet Young's modulus
g_m	$2.0 \times 10^{-8} m$	Lennard-Jones gap corresponding to maximum adhesive force
Γ	$1.0 \times 10^{-2} \frac{J}{m^2}$	Adhesion energy per area between surfaces
c	$1 \times 10^{14} \frac{N}{m^3}$	contact penetration penalty

Table 3.7: Material properties and problem parameters for sheet wrapping example

wrapping a graphene sheet is shown in Figure 3.31. The creation of nanotubes though folding a thin film has been of interest to the scientific community ([15], [17], [46]).

The problem of rolling a sheet around a cylinder is modeled here using shell finite elements connected by InterShells. The shell elements are geometrically nonlinear, allowing large displacements but small deformations through the corotational formulation [12]. The element pattern is very similar to that of the beam problem, shown in Figure 3.15, but with the upper sheet wrapped into a cylinder. The dimensions and properties for the problem are shown in Table 3.7. Here the diameter length scale is slightly larger than a typical nanotube, which is generally as large as $1 \mu m$ [15]. In general the scales of this problem were chosen to be on the same order as the other example problems presented earlier. For the boundary conditions of the finite element simulation, the cylinder is rigid with every nodal displacement prescribed to zero. The center points of the sheet directly under the cylinder's lowest point have prescribed vertical displacement directly toward the cylinder. The remaining sheet nodes are free to translate in the x and z-directions and to rotate about the y-axis while other displacements and rotations are prescribed to zero. This problem could only be solved with the static solver for relatively weak adhesive energies, causing only slight bending of the sheet as shown in Figure 3.32. For stronger adhesive energies, there was a certain point in the displacement controlled solution method where the sheet would try to wrap around the cylinder all in one step. As one element approaches the surface of the cylinder close enough to be pulled in it initiated a chain reaction where neighboring elements also became close enough to be pulled in. In this case the solver could not converge. Instead, for larger values of Γ, a quasi-static solver was employed. With appropriate levels of artificial damping and an adaptive pseudotime step a steady-state solution could be reached, shown in Figure 3.33. In this case the wrapping process was smooth due to the high damping term. This high level of damping makes intermediate solutions look as though the stiffness of the sheet is less than it is in reality.

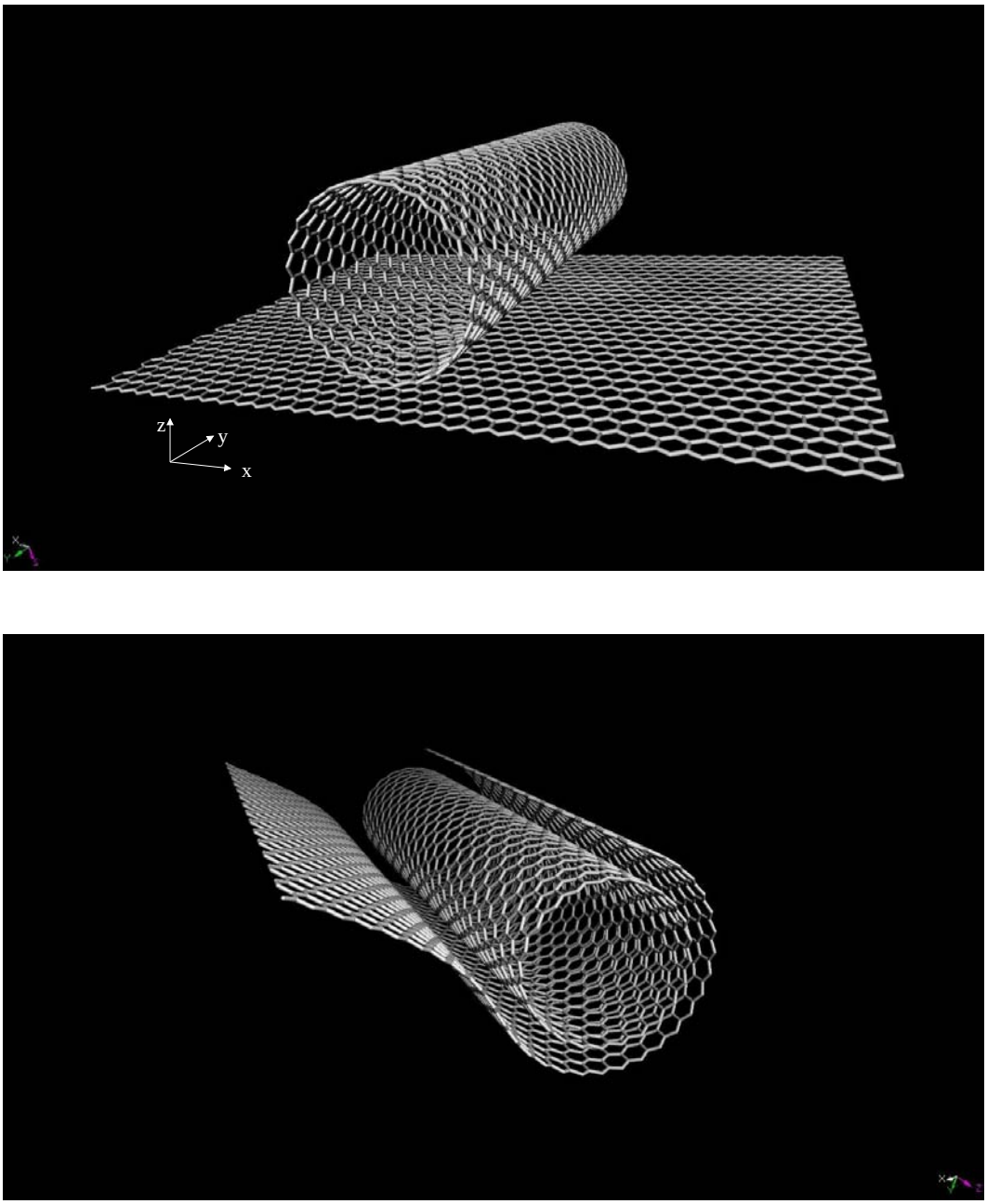

Figure 3.31: an illustration of a single walled carbon nanotube wrapping a graphene sheet around itself through van der Waals adhesion [5].

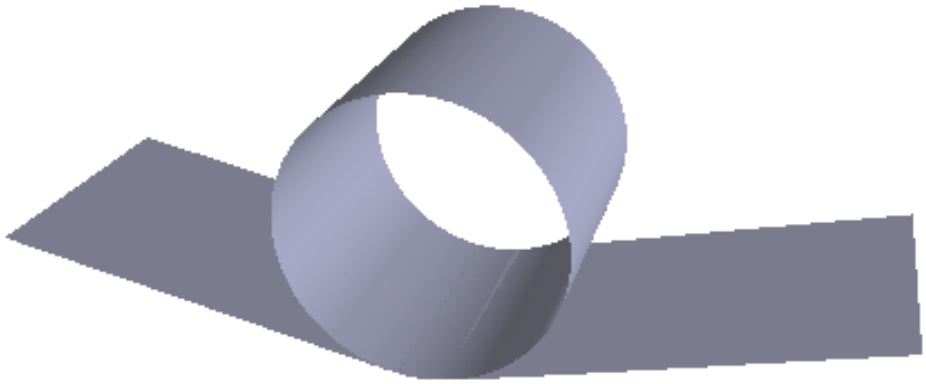

Figure 3.32: The sheet wrapping problem solved with a relatively gentle Γ and a static solver

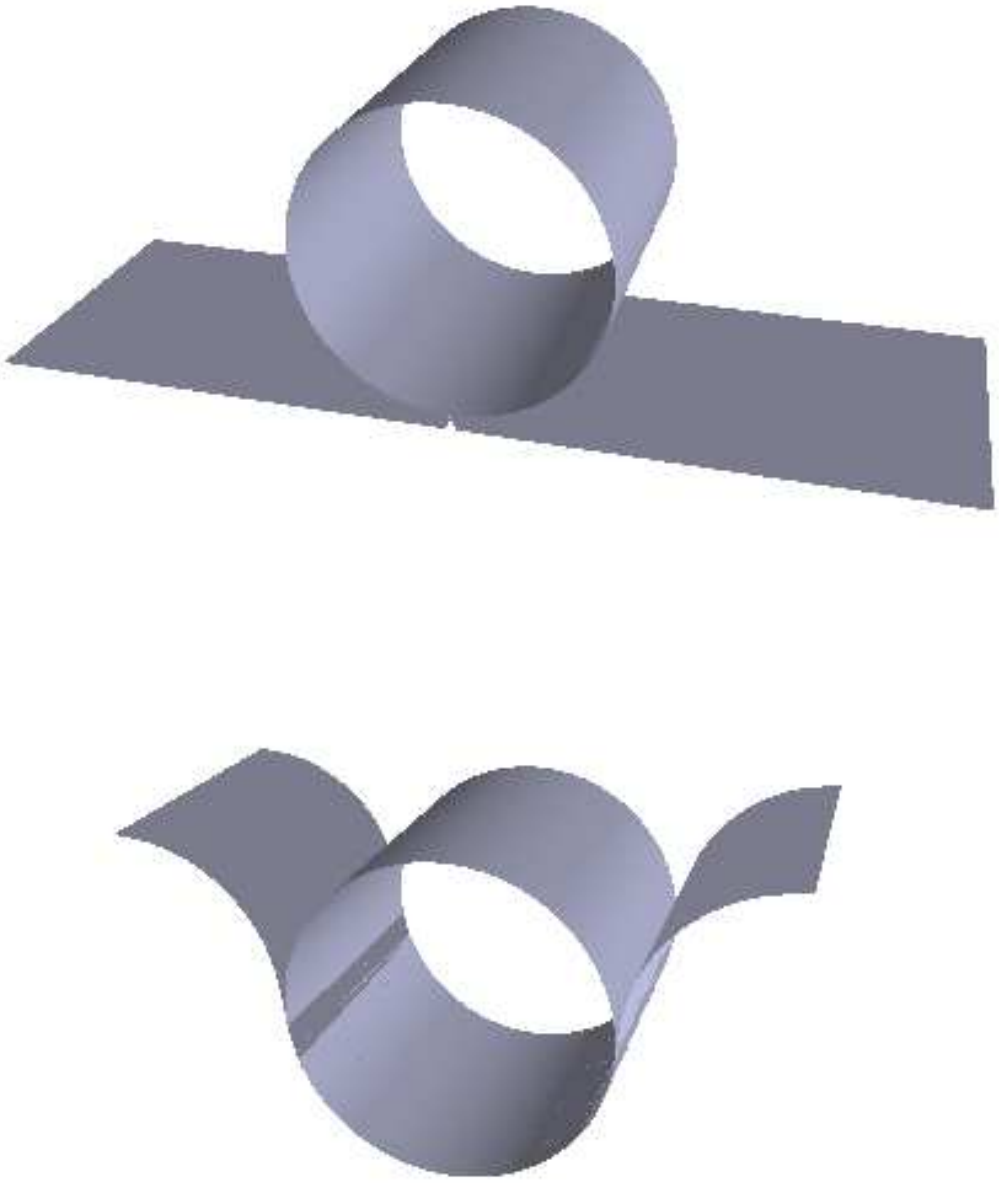

Figure 3.33: The sheet wrapping problem solved with a stronger adhesive with a quasi-static solver

Chapter 4

Design Framework

In this chapter, design optimization is applied to the adhesive finite element framework described in Chapter 3. First topology optimization is briefly described. Next sensitivity analysis is discussed and the analytical sensitivities of the Inter elements are computed and checked against finite differencing. Finally the beam delamination and cylinder examples from Chapter 3 are modified to include optimization of the force-displacement characteristic in delamination or compression. Several parameter studies and variations are explored.

In optimization problems there exists an objective function, z, which is a function of multiple optimization variables s_i. The goal is find the optimal values of the optimization variables s_i^* which minimize the objective function. In addition to the objective, there may be constraints which are also functions of the optimization variables. These may include equality constraints, h, or inequality constraints g. There may also be box constraints, or upper and lower boundaries for the optimization variables $\overline{s_i}$ and $\underline{s_i}$. The optimization problem can be expressed mathematically:

$$\begin{array}{lll} \min & z(s_i) & i = 0,1,\ldots,n_s \\ & g_j(s) & \leq 0 \quad j = 0,1,\ldots,n_g \\ & h_k(s) & = 0 \quad k = 0,1,\ldots,n_h \end{array}$$

$$s_i = \{s_i \in \mathbb{R} \mid \underline{s_i} \leq s_i \leq \overline{s_i}\}$$

where n_s, n_g and n_h are the numbers of optimization variables, inequality constraints and equality constraints.

For the structural optimization problems studied here gradient-based nonlinear programming is employed. Specifically, topology optimization is used, where the domain is discretized into a mesh and each element of the mesh represents a single optimization variable. Topology optimization is highly compatible with finite element analysis since in FEA there is also a domain that is discretized. Typically in topology optimization each optimization variable corresponds to an attribute of a single element such as density. For optimization within a finite element framework the objective function and constraints are rewritten to be functions of optimization criteria q_j, which correspond to components of the finite element problem or solution such as a maximum stress value or a nodal displacement. These criteria are functions of the optimization variables s_i and the displacement vector $\mathbf{u}$. For example, the objective can be rewritten as follows:

$$z = z(q_j(s_i, \mathbf{u}(s_i))) \tag{4.1}$$

4.1 Sensitivity Analysis

The optimization algorithms used here are gradient-based. To evaluate the gradients of the objective and constraints the sensitivities of the criteria need to be computed with respect to the optimization variables, $\frac{\partial q_j}{\partial s_i}$. The optimization algorithm uses this gradient information to decide which direction to move in the optimization variable space between each iteration. For example in the steepest descent method the optimizer assumes the best direction to search for the optimal solution is in the negative gradient direction. The sensitivities can be computed analytically or numerically. It is imperative that the gradients are calculated correctly and coded correctly. Typically the method used to verify the sensitivities in a finite element framework is to compare analytical results to those computed by a numerical finite difference scheme for a highly simplified problem, usually consisting of the fewest number of elements possible.

4.1.1 Finite Differences

Finite differencing is a numerical approximation for computing a derivative. The derivative of a function $q(s)$ is defined as

$$\frac{dq}{ds} \equiv \lim_{\varepsilon \to 0} \frac{q(s+\varepsilon) - q(s)}{\varepsilon}. \tag{4.2}$$

For finite values of ε this expression becomes an approximation of the derivative, called forward differencing. The error of the approximation is on the order $O(\varepsilon)$. The approximation error is significantly less for a central differencing scheme, defined as

$$\frac{dq}{ds} \cong \frac{q(s+\varepsilon) - q(s-\varepsilon)}{2\varepsilon} \tag{4.3}$$

The error of central differencing is on the order $O(\varepsilon^2)$.

There are two major drawbacks to using finite differencing as the method of computing sensitivities within a finite element optimization framework. One drawback is for each optimization variable the criteria need to be reevaluated twice for central differencing. Each evaluation of the criteria requires the entire finite element problem to be solved, which is prohibitively costly for nontrivial problems. The other drawback stems from the limitations of finite precision arithmetic. Theoretically central differencing, like forward differencing, should converge to the derivative as ε approaches zero. However truncation error increases as ε becomes small. There exists an optimal ε that minimizes the combined computational and mathematical error, but it is not known beforehand and may be different for each optimization variable. This is shown in Figure 4.1. This is a graph of the "II" column of data in Table 4.1. The central difference sensitivities over a range of ε values are compared to the analytically calculated sensitivity.

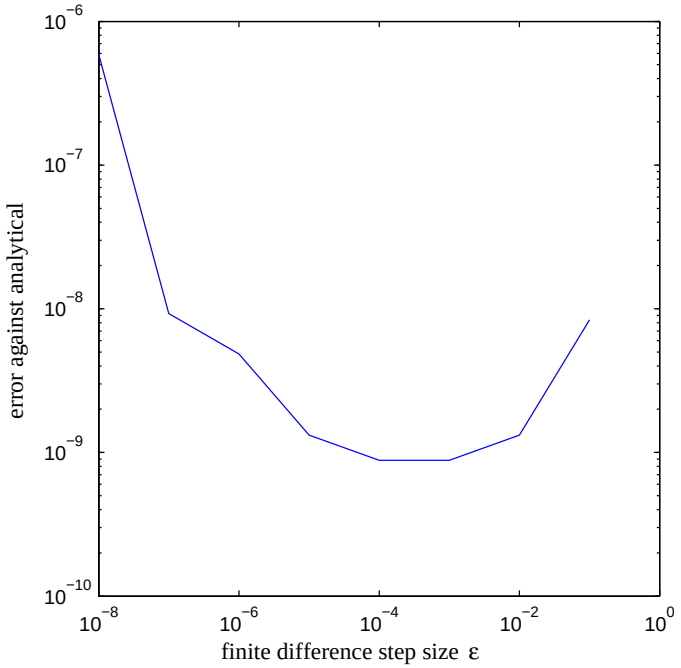

Figure 4.1: The error in calculating sensitivities of $\frac{\partial f_6}{\partial \Gamma}$ for the beam example. From data in Table 4.1.

4.1.2 Analytical Approach

In the analytical approach, the exact derivatives of the criteria with respect to the optimization variables are computed. Analytical sensitivity analysis is preferred over finite differencing because the computation is exact and does not require the finite element problem to be solved multiple times in each optimization iteration. On the elemental level, the derivatives of the internal force vector with respect to any possible material property or nodal coordinate needs to be computed, resulting in much more coding and the possibility for coding error. It is the possibility of human error that necessitates the checking of sensitivities computed analytically against finite differencing.

The sensitivities expressed analytically are

$$\frac{dq_j}{ds_i} = \frac{\partial q_j}{\partial s_i} + \frac{\partial q_j}{\partial \mathbf{u}}^T \frac{d\mathbf{u}}{ds_i} \tag{4.4}$$

Here the $\frac{d\mathbf{u}}{ds_i}$ term can be computed by differentiating the equilibrium residual equation,

$$\begin{aligned}
\mathbf{r}(s_i, \mathbf{u}(s_i)) &= 0 \\
\frac{d\mathbf{r}}{ds_i} &= 0 \\
\frac{\partial \mathbf{r}}{\partial s_i} + \frac{\partial \mathbf{r}}{\partial \mathbf{u}} \frac{d\mathbf{u}}{ds_i} &= 0 \\
\frac{\partial \mathbf{r}}{\partial s_i} + \mathbf{K}_t \frac{d\mathbf{u}}{ds_i} &= 0 \\
\frac{d\mathbf{u}}{ds_i} &= -\mathbf{K}_t^{-1} \frac{\partial \mathbf{r}}{\partial s_i}
\end{aligned} \tag{4.5}$$

substituting Equation 4.5 into Equation 4.4,

$$\frac{dq_j}{ds_i} = \frac{\partial q_j}{\partial s_i} - \frac{\partial q_j}{\partial \mathbf{u}}^T \mathbf{K}_t^{-1} \frac{\partial \mathbf{r}}{\partial s_i} \tag{4.6}$$

There are two methods to compute the sensitivities analytically, the direct and adjoint methods. They differ in the number of times it is necessary to solve an equation involving the tangential stiffness matrix, which is computationally costly. In the direct method the $\frac{d\mathbf{u}}{ds_i} = -\mathbf{K}_t^{-1} \frac{\partial \mathbf{r}}{\partial s_i}$ part of the second term of Equation 4.6 is solved first. This equation needs to be solved once for each optimization variable s_i, a total of n_s times. In the adjoint method, the adjoint vector $\mathbf{a}_j = \frac{\partial q_j}{\partial \mathbf{u}}^T \mathbf{K}_t^{-1}$ part of the second term of Equation 4.6 is solved first. This equation needs to be solved once for each criteria, n_q. Therefore in the case $n_s > n_q$, which is true in the majority of topology optimization problems, the adjoint method requires fewer effective inversions of the tangential stiffness matrix.

In both the direct and adjoint methods the quantity $\frac{\partial \mathbf{r}}{\partial s_i}$, called the pseudoload vector, needs to be computed. From the definition of the residual $\mathbf{r} = \mathbf{f} - \mathbf{p}$ where $\mathbf{f}$ is the external force and $\mathbf{p}$ is the internal force,

$$\frac{\partial \mathbf{r}}{\partial s_i} = \frac{\partial \mathbf{f}}{\partial s_i} - \frac{\partial \mathbf{p}}{\partial s_i} \tag{4.7}$$

The internal force derivative is computed on the element level and is assembled into the global vector in the same way as the internal force. Of the three Inter elements, the sensitivities of the InterQuad element may be the most simple to compute. The derivative of the internal force vector (Equation 3.25) with respect to an arbitrary optimization variable is

$$\frac{d\mathbf{p}}{ds_i} = \frac{1}{2}\left(\frac{dw}{ds_i}L + w\frac{dL}{ds_i}\right) \sum_k^n w_i \sigma(g_k) \frac{\partial g}{\partial \mathbf{u}}\bigg|_{x_{g_k}} + \frac{wL}{2} \sum_k^n w_k \left(\frac{d\sigma}{ds_i}\frac{\partial g}{\partial \mathbf{u}}\right)\bigg|_{x_{g_k}} \tag{4.8}$$

The derivative $\frac{d\sigma}{ds_i}$ corresponds to whichever one-dimensional adhesion model is in use. For the Lennard-Jones case,

$$\frac{d\sigma}{ds_i} = \frac{\partial \sigma}{\partial g}\frac{dg}{ds_i} + \frac{\partial \sigma}{\partial c}\frac{dc}{ds_i} + \frac{\partial \sigma}{\partial g_m}\frac{dg_m}{ds_i} + \frac{\partial \sigma}{\partial \Gamma}\frac{d\Gamma}{ds_i} \tag{4.9}$$

where g is the gap between upper and lower edges of the element, c is the contact penalty term, g_m is the gap size that maximizes the adhesive force and Γ is the energy of adhesion per area. The partial derivatives of Equation 3.8 with respect to the above variables are

$$\frac{\partial \sigma}{\partial g} = \begin{cases} c & ,g < 0 \\ ab\left(\frac{-3}{(bg+1)^4} + \frac{9}{(bg+1)^{10}}\right) & ,g \geq 0 \end{cases} \tag{4.10}$$

$$\frac{\partial \sigma}{\partial c} = \begin{cases} g & ,g < 0 \\ 0 & ,g \geq 0 \end{cases} \tag{4.11}$$

$$\frac{\partial \sigma}{\partial g_m} = \begin{cases} 0 & ,g < 0 \\ \frac{a}{g_m}\left(\frac{3bg}{(gb+1)^4} - \frac{1}{(gb+1)^3} + \frac{1}{(gb+1)^9} - \frac{9bg}{(gb+1)^{10}}\right) & ,g \geq 0 \end{cases} \tag{4.12}$$

and a and b are defined in Equations 3.13 and 3.10. The derivatives of other one-dimensional σ functions would need to be computed in the same matter. Finally, differentiating Equation 3.23,

$$\frac{dg}{ds_i} = N_{4y}\left(\frac{dy_{04}}{ds_i} + \frac{du_{4y}}{ds_i}\right) + N_{3y}\left(\frac{dy_{03}}{ds_i} + \frac{du_{3y}}{ds_i}\right) - N_{1y}\left(\frac{dy_{01}}{ds_i} + \frac{du_{1y}}{ds_i}\right) - N_{2y}\left(\frac{dy_{02}}{ds_i} + \frac{du_{2y}}{ds_i}\right) \tag{4.13}$$

For the InterBeam element the derivative of the gap with respect to the optimization variable is much more complicated because the shape functions are functions of the nodal coordinates. There is also an additional term in the $\frac{d\mathbf{p}}{ds_i}$ equation since the $\frac{\partial g}{\partial \mathbf{u}}$ vector is a function of the shape functions and is not constant in s_i. The sensitivities of InterShell elements are similar to InterQuads since the shape functions are constant in s_i.

In the above equations, the derivatives of the Inter element material properties, nodal displacements and nodal coordinates with respect to the optimization variables are supplied as input. Coding the most general case allows the optimization variables to be functions of any combination of material properties of nodal coordinates.

4.1.3 Results

The sensitivities for the InterBeam element was computed by constructing a simple 5-element system, shown in Figure 4.2. There are two beams, made of two beam elements each, which are

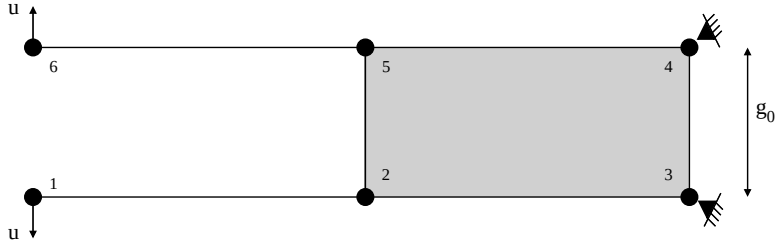

Figure 4.2: The finite element layout for the InterBeam element sensitivity check

$\frac{\partial f_6}{\partial \Gamma}$	**I**	**II**	**III**
direct	$3.696746841 \times 10^{0}$	$2.270400493 \times 10^{-1}$	$4.094092631 \times 10^{-5}$
adjoint	$3.696746841 \times 10^{0}$	$2.270400493 \times 10^{-1}$	$4.094092628 \times 10^{-5}$
$\varepsilon = 1 \times 10^{-1}$	$3.696286841 \times 10^{0}$	$2.270400512 \times 10^{-1}$	$4.093309709 \times 10^{-5}$
1×10^{-2}	$3.696742240 \times 10^{0}$	$2.270400496 \times 10^{-1}$	$4.092980252 \times 10^{-5}$
1×10^{-3}	$3.696746796 \times 10^{0}$	$2.270400495 \times 10^{-1}$	$4.092180105 \times 10^{-5}$
1×10^{-4}	$3.696746841 \times 10^{0}$	$2.270400495 \times 10^{-1}$	$4.078951661 \times 10^{-5}$
1×10^{-5}	$3.696746842 \times 10^{0}$	$2.270400496 \times 10^{-1}$	$4.080763782 \times 10^{-5}$
1×10^{-6}	$3.696746840 \times 10^{0}$	$2.270400504 \times 10^{-1}$	$3.484397950 \times 10^{-5}$
1×10^{-7}	$3.696746827 \times 10^{0}$	$2.270400472 \times 10^{-1}$	$2.310063506 \times 10^{-4}$
1×10^{-8}	$3.696746982 \times 10^{0}$	$2.270401822 \times 10^{-1}$	$2.260155132 \times 10^{-3}$

Table 4.1: Sensitivities of the force at node 6 of the InterBeam example to adhesive energy, Γ

constrained in all degrees of freedom at nodes 3 and 4 and in the x-direction at nodes 1 and 6. Equal y-displacements are applied to nodes 1 and 6 as shown. Between the beams there is a single InterBeam element. The sensitivities of the force at node 6 to the adhesive energy per area of the InterQuad element is in Table 4.1. The three different cases examined correspond to gap sizes g_0 that correspond to different regions of the Lennard-Jones adhesion law, shown in Figure 4.3. In all

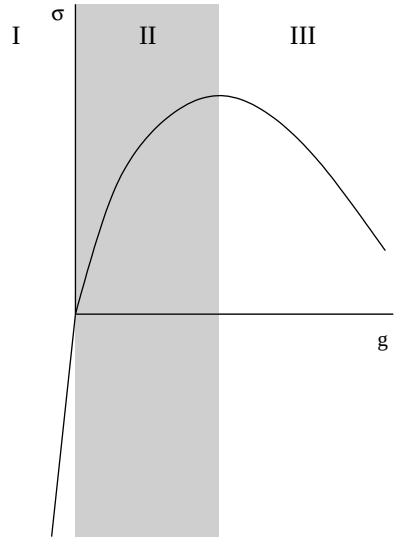

Figure 4.3: Lennard-Jones adhesive law with three gap size zones indicated. I. Contact, II. Positive slope, III. Negative slope

three initial gap size cases the sensitivities between the direct and adjoint analytical methods agree exactly, and they both agree within several digits of accuracy to the central differencing results. One exception is very small ε values for the gap in region III, which are orders of magnitude different than the analytical results. This can be explained by truncation error.

Table 4.2 shows the data for the sensitivities of the tip force to beam width. Width is explored

$\frac{\partial f_6}{\partial w}$	**I**	**II**	**III**
direct	$4.449455236 \times 10^{0}$	$5.529858599 \times 10^{-1}$	$4.094179274 \times 10^{-2}$
adjoint	$4.449455236 \times 10^{0}$	$5.529858599 \times 10^{-1}$	$4.094179274 \times 10^{-2}$
$\varepsilon = 1 \times 10^{-1}$	$4.449455236 \times 10^{0}$	$5.529858599 \times 10^{-1}$	$4.094179254 \times 10^{-2}$
1×10^{-2}	$4.449455236 \times 10^{0}$	$5.529858599 \times 10^{-1}$	$4.094179275 \times 10^{-2}$
1×10^{-3}	$4.449455236 \times 10^{0}$	$5.529858592 \times 10^{-1}$	$4.094179099 \times 10^{-2}$
1×10^{-4}	$4.449455236 \times 10^{0}$	$5.529859907 \times 10^{-1}$	$4.094164689 \times 10^{-2}$
1×10^{-5}	$4.449455236 \times 10^{0}$	$5.529855603 \times 10^{-1}$	$4.094196780 \times 10^{-2}$
1×10^{-6}	$4.449455234 \times 10^{0}$	$5.529875401 \times 10^{-1}$	$4.096046156 \times 10^{-2}$
1×10^{-7}	$4.449455248 \times 10^{0}$	$5.530231104 \times 10^{-1}$	$4.099429810 \times 10^{-2}$
1×10^{-8}	$4.449455207 \times 10^{0}$	$5.533583741 \times 10^{-1}$	$4.024173437 \times 10^{-2}$

Table 4.2: Sensitivities of the force at node 6 of the InterBeam example to beam width, *w*

as an optimization variable in Section 4.2.2.1. As with the sensitivities to energy of adhesion per area, the analytical measures agree exactly and they both agree with the numerical results to several significant digits.

The sensitivities of the InterQuad and InterShell were also verified. The setup for the InterQuad check is shown in Figure 4.4. Here a single InterQuad element is positioned between two 4 node

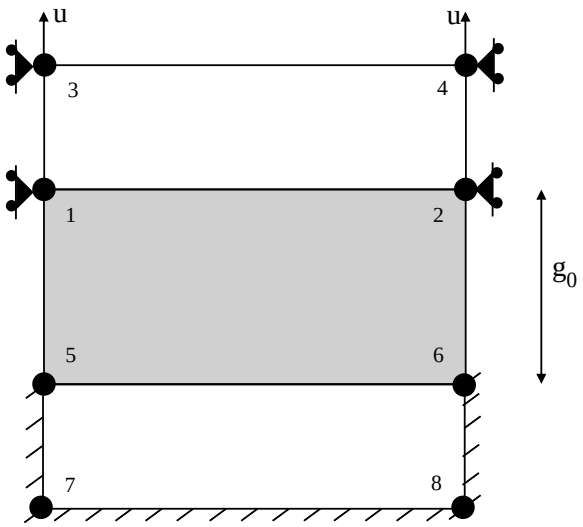

Figure 4.4: The finite element layout for the InterQuad element sensitivity check

quadrilateral elements. Nodes 5-8 are fixed in both x and y and nodes 1-4 are only free in y. The stiffness of the upper quadrilateral element was set high relative to the energy of adhesion of the InterQuad element such that it would not deform under displacement of nodes 3 and 4. Since the same functions for derivatives of the adhesion law are used by all three Inter elements, it is only necessary to check the sensitivities in one of the regions of the Lennard-Jones function. The dimensions of this problems were increased to the macroscale to help alleviate truncation errors.

$\frac{\partial f_1}{\partial \Gamma}$	**II**
direct	1.256271149×10^7
adjoint	1.256271149×10^7
$\varepsilon = 1 \times 10^{-1}$	1.261395711×10^7
1×10^{-2}	1.256323620×10^7
1×10^{-3}	1.256271673×10^7
1×10^{-4}	1.256271154×10^7
1×10^{-5}	1.256271149×10^7
1×10^{-6}	1.256271149×10^7
1×10^{-7}	1.256271147×10^7
1×10^{-8}	1.256271151×10^7

Table 4.3: Sensitivities of the force at node 1 of the InterQuad example to adhesion energy, Γ

These sensitivities are given in Table 4.3. For the InterQuad element the sensitivities agree well between the analytical and numerical techniques. In this case larger error between the analytical and numerical solutions occurs for larger ε values.

Finally the sensitivities of the InterShell element were tested. The setup is similar to the InterQuad setup, shown in Figure 4.5. An InterShell element is sandwiched between two 3-node

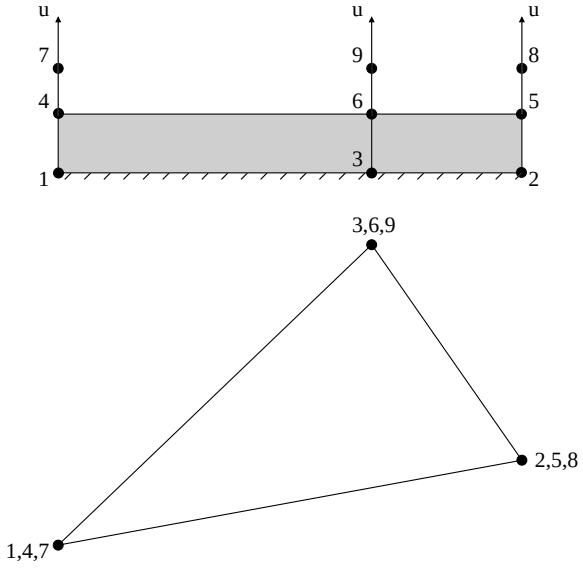

Figure 4.5: The finite element layout for the InterShell element sensitivity check

shell elements. One difference is the addition of bar elements at nodes 4-6. This additions was necessary because otherwise there would be no nodes that had an unspecified displacement degree of freedom. Also as with the InterQuad example, the dimensions used were on the macroscale.

$\frac{\partial f_1}{\partial \Gamma}$	**II**
direct	2.259858413×10^6
adjoint	2.259858413×10^6
$\varepsilon = 1 \times 10^{-1}$	2.982228635×10^6
1×10^{-2}	2.982228808×10^6
1×10^{-3}	2.982234007×10^6
1×10^{-4}	2.982216677×10^6
1×10^{-5}	2.982476626×10^6
1×10^{-6}	2.980743635×10^6
1×10^{-7}	2.946083825×10^6
1×10^{-8}	3.465980955×10^6

Table 4.4: Sensitivities of the force at node 7 of the InterShell example to adhesion energy, Γ

4.2 Beam Delamination Example

The first problem studied is derived from the beam delamination problem of Section 3.3. Unless otherwise stated, the problem parameters are the same as given in Table 3.2. In all variations of the problem described below, the objective is to minimize the difference between the tip force-displacement response and some objective function. For example in Figure 4.10(a) the objective force-displacement function is linear, denoted by the square indicators. The optimization criteria q_j are the nodal forces at the leftmost tip of the beam at various specified tip displacement levels. As in Chapter 3, the analysis is displacement controlled. The tip force and nodal displacement vector are saved at various displacement levels for objective evaluation and sensitivity calculation. The objective z is to minimize the area between the line segments defined by the objective points and the optimization force-displacement solution points at the corresponding tip displacements, shown graphically in Figure 4.6. Mathematically, the objective is defined

$$z = \sum_{j=0}^{n_{obj}} \left(f_{o_{j+1}} - q_{j+1} + f_{o_j} - q_j \right)^2 \tag{4.14}$$

where n_{obj} is the number of objective points and f_{o_j} are the force levels of the objective points corresponding to the j^{th} criteria. The 0^{th} criteria is always zero. This equation squares the area to guarantee that the number is always positive and disregards the $\frac{1}{4}(u_{t_{j+1}} - u_{t_j})^2$ term. The tip displacements term puts a larger emphasis on minimizing sections of the objective with larger spacing between the specified tip displacements u_{t_j}, which may not be desirable

For all optimization problems described in this chapter a GCMMA, or globally convergent method of moving asymptotes is employed. This method was developed and described in detail by Svanberg [48].

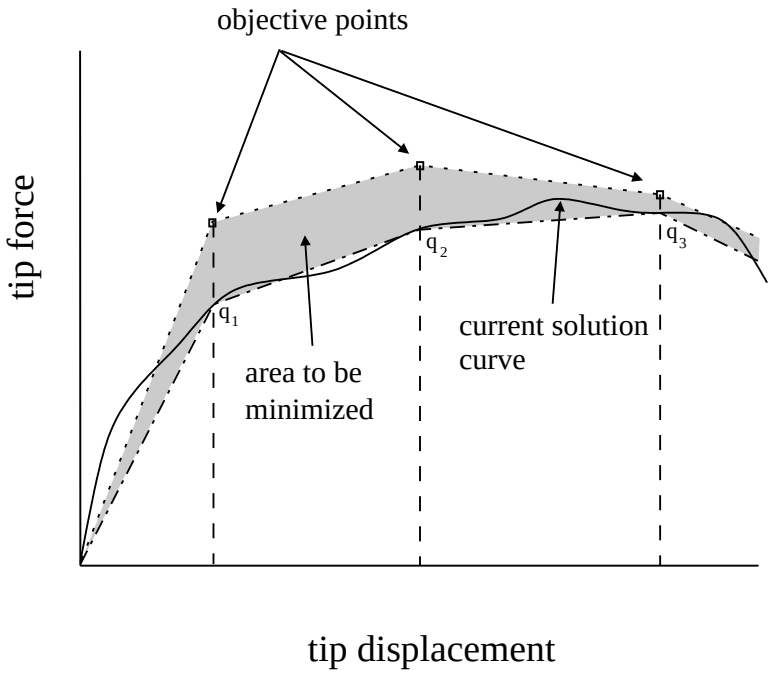

Figure 4.6: The force-displacement objective is the area between the line segments defined by the objective points and the optimization force-displacement solution points at the corresponding tip displacements.

4.2.1 Preconstructed Solution

Although the goal in this work is to demonstrate the ability to find an adhesive energy distribution that meets an arbitrary objective, it is useful to study the case where the optimal adhesive distribution is known beforehand. In the case presented here the glue distribution pattern shown in Figure 4.7(b) was applied. The figure shows the beam, looking from the top down. The left end is the tip, which is lifted off the substrate. The black regions correspond to the maximum adhesive energy allowed by the optimization box constraints ($1 \times 10^{-3} \frac{\mu J}{m^2}$) while the white corresponds to the minimum energy per area (effectively zero). The delamination behavior of this adhesive pattern is to rip each strip of adhesive individually. The tip force-displacement characteristic is shown in the dotted line of Figure 4.7(a). There are two sharp dropoffs in force as the tip displacement increases, corresponding to the two adhesive strips delaminating. This force-displacement curve was taken as the objective for an optimization problem. Twenty points along the curve were used. Figure 4.8 shows the progression of the optimization from the initial conditions, where the entire beam has the maximum adhesive energy per area, to the solution which is effectively the same as the case used to generate the objective.

In this problem each optimization variable corresponded to the adhesive energy per area of a group of 20 elements along the beam. There were four variables to each 'strip' in the optimal distribution. This example demonstrates that topology optimization techniques can be applied to simple adhesive problems.

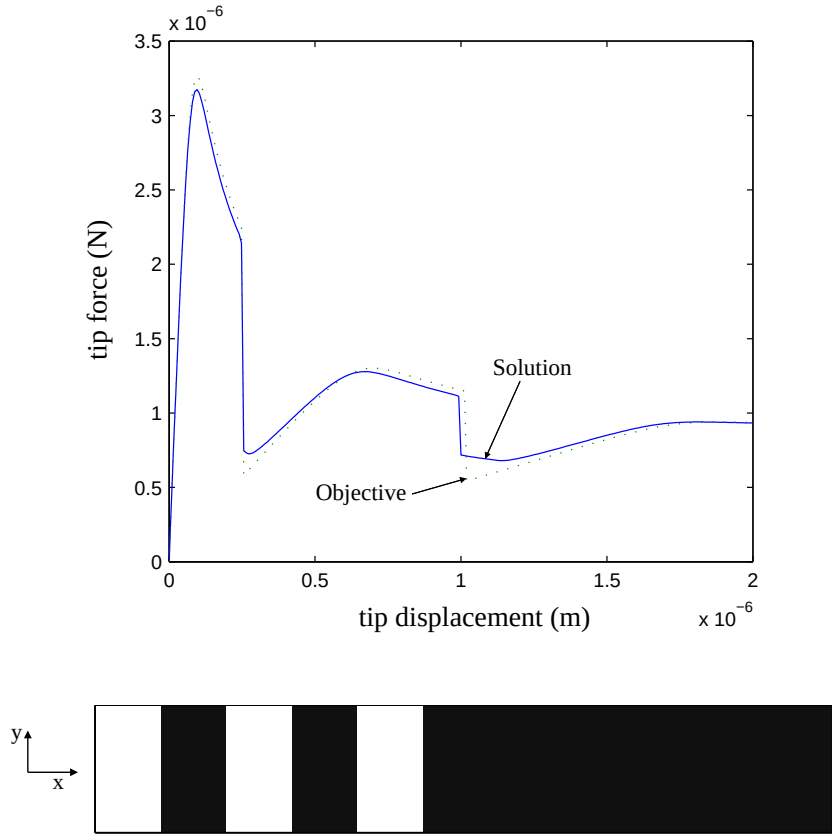

Figure 4.7: The beam optimization problem with preconstructed 'strips' adhesive energy distribution. (a) Tip force versus tip displacement. The solid curve is the tip force-displacement characteristic of the optimized solution while the dotted curve is the optimization objective behavior. (b) The distribution of adhesive energy along the beam-substrate interface used to generate the objective. Darker regions indicate higher adhesive energy.

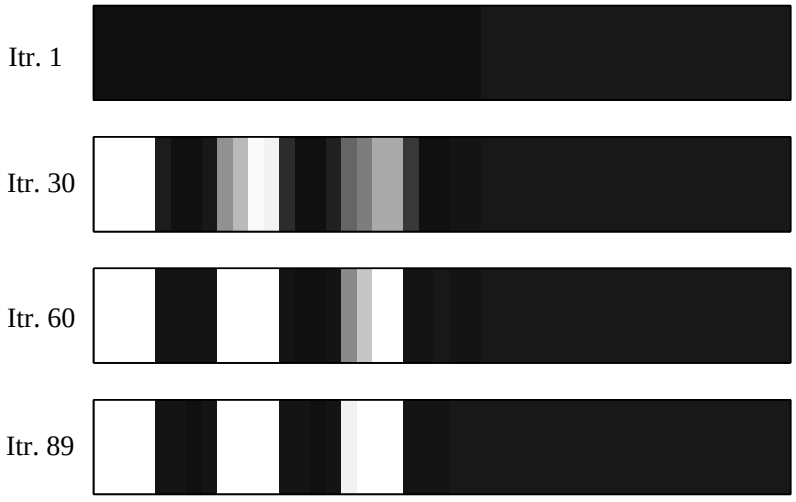

Figure 4.8: The progression of the prescribed optimization problem from the initial conditions to the final solution. Intermediate results at 30 and 60 optimization iterations are shown.

4.2.1.1 Initial Condition Study

In optimization problems the selection of the initial conditions for the optimization variables can have a large impact on the solution. For some initial conditions the optimizer may find a local minimum instead of the global optimum, especially if the initial values are not close to the optimal solution. In the case of adhesion a poor selection of initial conditions can prevent the optimal solution from ever being reached. If the triangular adhesion model is used (Equation 3.15) and the initial gap sizes of all the elements is greater than u_2 then the sensitivities of the nodal forces are identically zero, giving the optimizer no gradient information and making optimization impossible. However, if the initial conditions left at least some Inter element gap sizes in the range less than u_2 the sensitivities in those element become non-zero, giving the optimizer needed gradient data for finding the next solution step.

The preconstructed beam delamination problem is relatively insensitive to initial Γ conditions. Figure 4.9 shows the optimization solutions for a range of initial conditions. For all of these cases

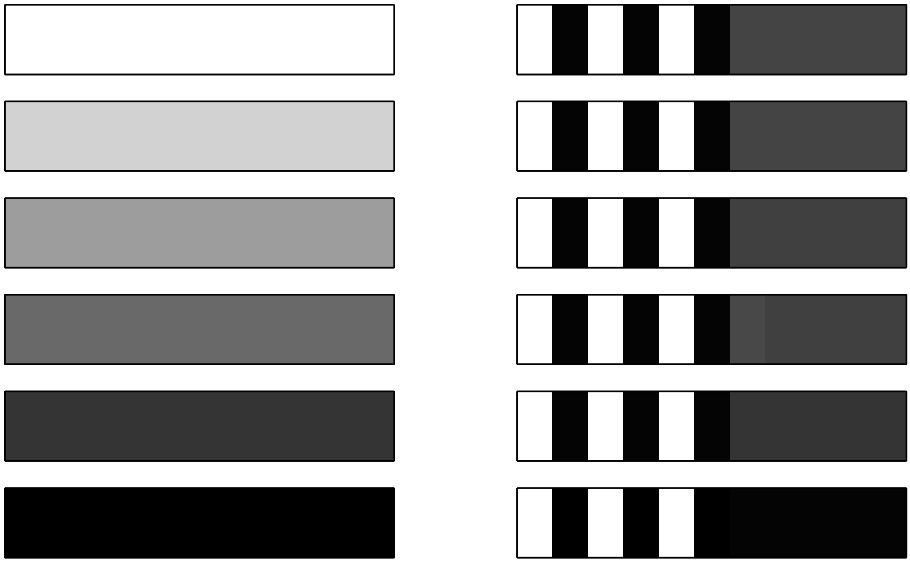

Figure 4.9: The solution to the optimization problem starting from various initial conditions. The initial conditions are shown on the left and the corresponding optimization solution is on the right.

the same solution emerged in the region ahead of the final crack tip. However the Γ values in the region of the beam that remains adhered to the substrate are different in each initial condition case. This is due to the fact that these elements do not contribute to the tip force, making the sensitivities of these elements to Γ nearly zero. Since the optimizer does not detect gradients for these elements, the Γ values are left unchanged. For the lower initial condition cases, these element did have non-negligible gradient in the early optimization iteration when the crack tip was able to traverse further down the beam. As the solution evolved, however, the crack tip never reached those elements at the base of the beam, freezing the Γ values there. These artifact Γ values that do not contribute to the solution can be removed by imposing another term to the objective minimizing the total amount of adhesive energy per area, as shown in Figure 4.10(b) of the following section.

variable	value	description
$\overline{s_i}$	1×10^{-3}	maximum allowed value for opt. var. (Γ)
$\underline{s_i}$	1×10^{-11}	minimum allowed value for opt. var. (Γ)
s_{i0}	1×10^{-11}	initial value for opt. var.

Table 4.5: Box constraints and initial value for optimization variables in baseline optimization problem.

4.2.2 Unknown Solution

In this section the optimal solution is not known beforehand. Instead, an objective is constructed and the optimizer finds the optimal values for the chosen variables. Like in the analytical beam delamination studies of Chapter 3, a baseline optimization case is defined and all subsequent cases and studies are variations of this case. The optimization objective is a linear force-displacement relationship, shown in Figure 4.10(a).

Including the origin there are 20 objective points, increasing linearly until the tip force is $9 \times 10^{-7}\,N$ at a tip displacement of $1 \times 10^{-6}\,m$. This objective is reachable given the box constraints on the optimization variables. The objective force displacement relation lies between the curves where the optimization variables are at the maximum and minimum box constraints, as shown in Figure 4.15. In this case the optimization variables, as in the preconstructed solution cases, correspond to the energy of adhesion per area Γ of groups of elements along the beam. Here each variable is associated with a group of 4 elements, allowing much greater variability in the distribution of adhesive over the beam than in the preconstructed case where 20 elements corresponded to each variable. The box constraints and initial conditions are shown in Table 4.5.

Figure 4.10(a) shows that the optimizer found an adhesive distribution that matches the objective closely. The final value of the objective was 4.4×10^{-5}, which is six orders of magnitude less than the initial value of 1.9×10^{1}. The first diagram in Figure 4.10(b) shows the corresponding adhesive energy distribution to the solution in Figure 4.10(a). The most important feature to note is that ahead of the final crack tip position (indicated by the small triangle above the diagram) there is virtually no adhesive toward the tip, and there is a quick transition from no adhesive to maximum allowed adhesive over a very short range.

It is important to note that the adhesive energy beyond the final crack tip location does not contribute to the force-displacement characteristic in the region that the objective is defined over. Adding another term to the objective function which sums the total amount of adhesive energy applied to the beam forces a reduction of adhesive energy in regions of the beam that have no impact on the original objective. The solution to this modified problem is shown in the second diagram in Figure 4.10(b). It is identical to the solution without the adhesive reduction objective but with the majority of the adhesive energy beyond the final crack tip location removed. The force-displacement characteristic curve, plotted over the same range as that in Figure 4.10(a), looks identical to the case without the adhesive reduction objective addition.

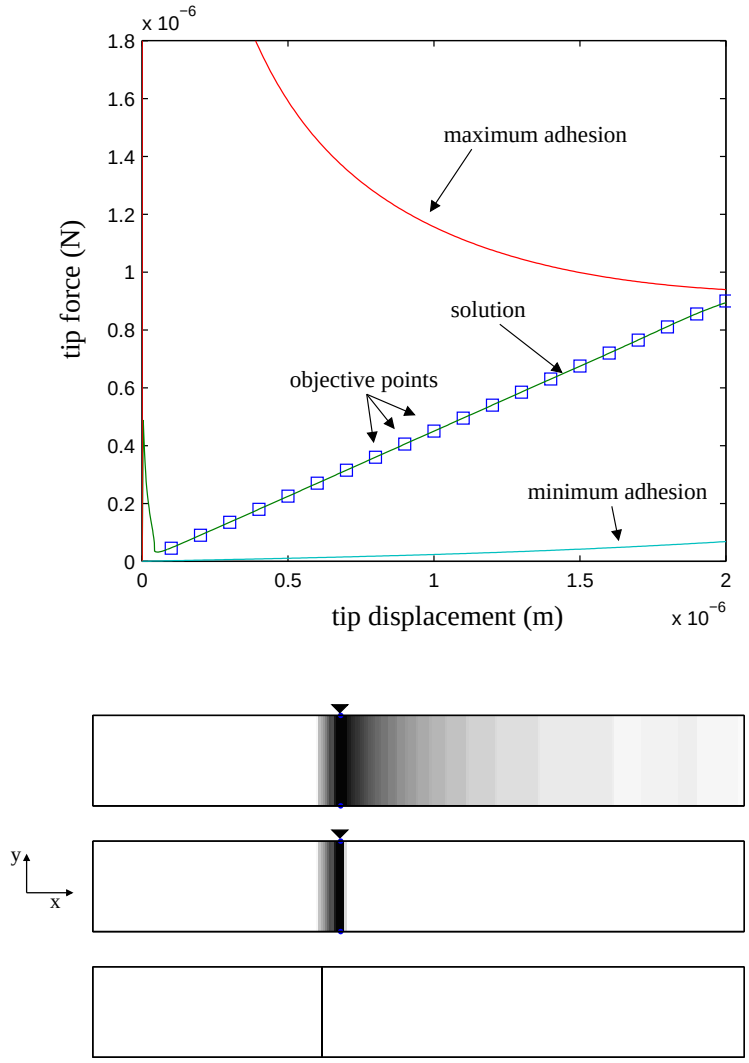

Figure 4.10: The baseline optimization problem. (a) Tip force versus tip displacement. The squares indicate objective points and the solid line passing through them indicates the solution reached by the optimizer. Analysis with all elements set to maximum adhesive and minimum adhesive also shown. (b) The distribution of adhesive energy along the beam-substrate interface. Darker regions indicate higher adhesive energy. The top diagram is the adhesive distribution corresponding to the solution curve in (a). The middle diagram is the same solution but with extraneous adhesive removed through a modification of the objective. The bottom diagram is the corresponding analytical solution for infinite adhesive energy

variable	value	description
$\overline{s_i}$	8×10^{-5}	maximum allowed value for opt. var. (w)
$\underline{s_i}$	8×10^{-7}	minimum allowed value for opt. var. (w)
s_{i0}	1×10^{-11}	initial value for opt. var.

Table 4.6: Box constraints and initial value for beam width optimization variables.

This result can be compared to a roughly analogous analytically obtainable solution. If there was no upper box constraint on Γ, then the effect of adding a thin strip of relatively strong adhesive would be the same as clamping the beam at that point. A clamped beam has the same linear response as the objective function in this case. To find the location of this adhesive strip Equation 3.67 is solved for the crack length s given the slope of the objective, $\frac{F_t}{u_t}$. The result is shown in the third diagram of Figure 4.10(b). Note the similarities between the second and third diagrams of Figure 4.10(b). In the optimization problem the box constraint on Γ makes the analytical solution unobtainable, and the adhesive energy is instead spread over a larger region and the final crack tip location is slightly further back along the beam than in the clamped case.

In topology optimization problems it it typically desirable to have a 0-1 solution, or a solution where the optimization variables approach their box constraints. Although in these beam delamination cases the adhesive energy does not tend to a 0-1 solution in general, the results can be reinterpreted that way. The surface of the beam that is being patterned with various adhesive energy levels is two dimensional. If the width of a given adhesive strip on the beam is seen independent of the beam width, a pattern of uniform adhesive energy can be created that has the same adhesive properties as the case with variable adhesive energy but fixed adhesive width, shown in Figure 4.11.

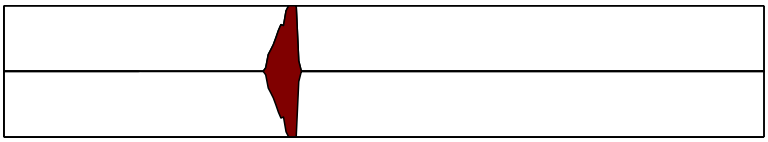

Figure 4.11: The solution to the baseline optimization problem reinterpreted as a constant Γ but variable adhesive width keeping beam width fixed.

4.2.2.1 Beam Width as Structural Variable

In the baseline case the adhesive energies of small groups of elements along the beam are the structural optimization variables. However other parameters can be varied in addition to the energy of adhesion. First the beam width is studied as an optimization variable. Varying the beam width affects both the moment of inertia of the beam and also the width of the InterBeam element, which is locked together to the beam width. The design tended to be much more sensitive to beam width than to the adhesion energy generally, necessitating tighter box constraints shown in Table 4.6.

When beam width was the only optimization variable the optimizer drove the problem to an intermediate step which did not converge in the analytical solver. Figure 4.12 shows the last solution iteration before the problem diverged. Toward the tip of the beam the optimizer formed hinge-like

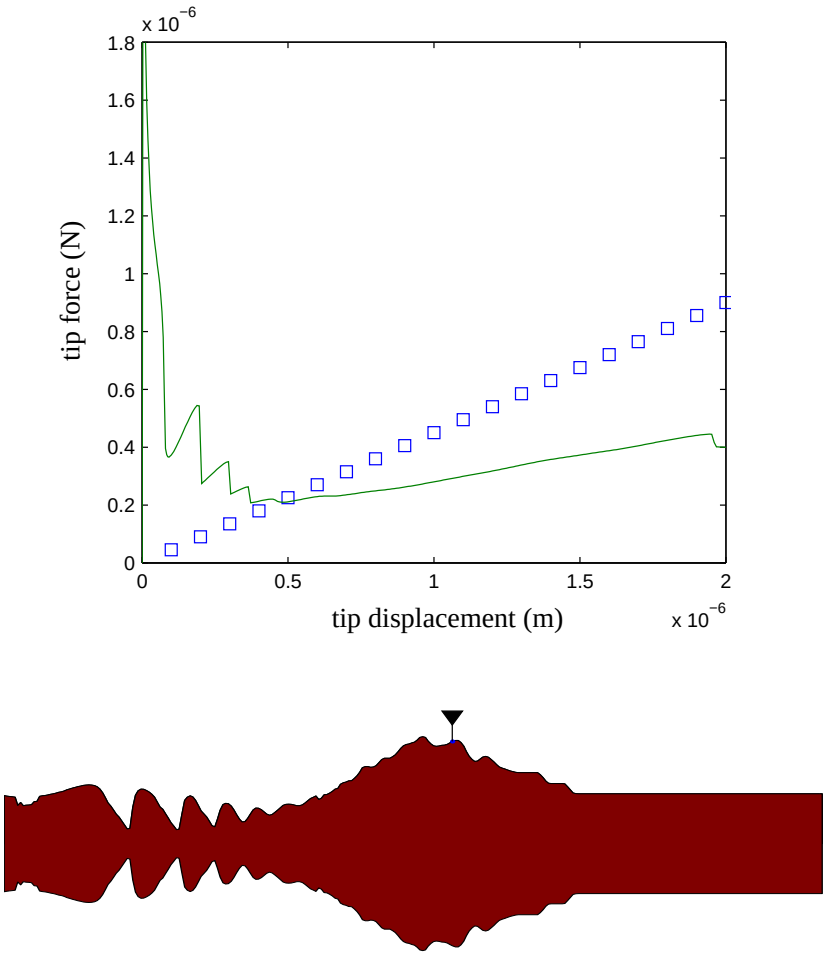

Figure 4.12: The beam optimization problem with width as variable. (a) Tip force versus tip displacement. (b) Top-down view of beam shape. Final crack tip location marked.

structures in an attempt to match the individual objective points. Each hinge corresponds to the sharp drop in tip force at the first several objective points. The main issue here seemed to be that adhesive energy was equally distributed along the beam, not allowing the clamped behavior seen previously.

The problem of divergence can be alleviated if Γ is varied along with beam width. In this case each group of 4 InterBeam elements have a corresponding variable for width and for adhesive energy per area. The solution is shown in Figure 4.13. In this case there is a single hinge formed in the same region where adhesive energy begins to appear. There are several areas ahead of the hinge where the width suddenly becomes smaller or larger, creating wing-like structures. In an attempt to force the optimizer to reduce these structures the total surface area of the beam was constrained to 25% of the area of the beam in Figure 4.13(a). The results are shown in Figure 4.14.

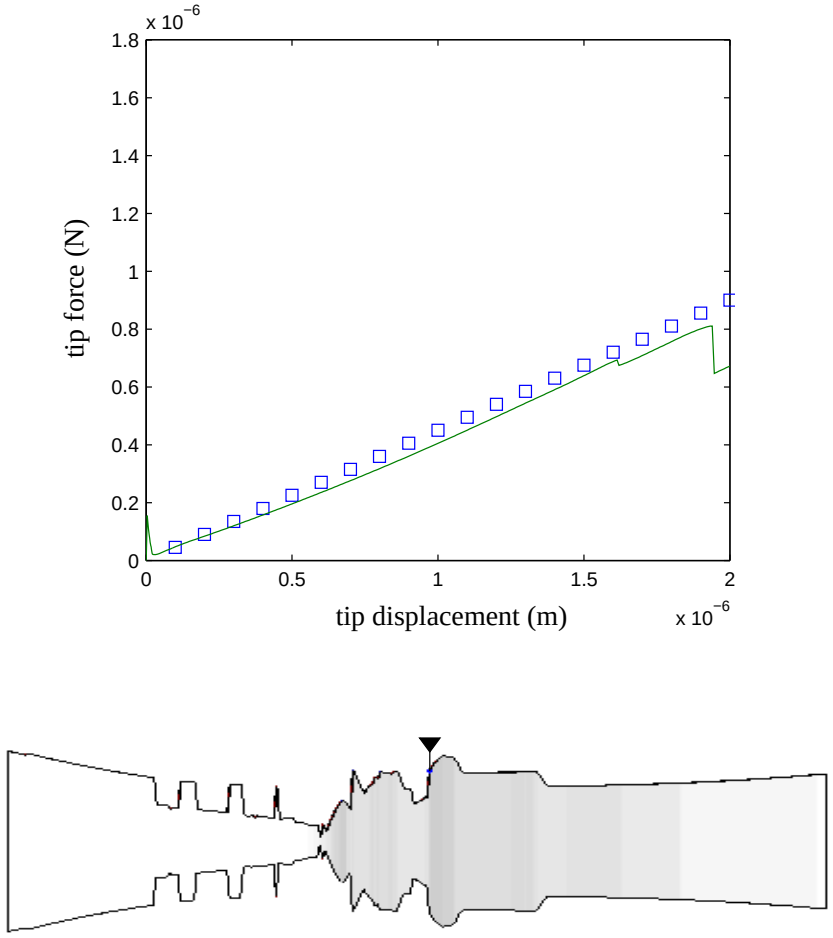

Figure 4.13: The beam optimization problem with both adhesion energy and width as variables. (a) Tip force versus tip displacement. (b) Top-down view of beam shape with adhesion energy distribution superimposed

Note that the beams shown in Figures 4.13(b) and 4.14(b) are not drawn to the same scale. When this constraint is applied the wing structures ahead of the crack tip are reduced somewhat and the hinging effect is less drastic than in the unconstrained case. Figure 4.14(c) shows an alternate view of the energy of adhesion distribution. As in Figure 4.11, Γ is held constant while the width of the adhesive is varied independently of the beam width.

4.2.2.2 Objectives

Figure 4.15 shows the baseline optimization objective along with three other variations. Additionally the envelope of possible solutions is shown. The maximum curve corresponds to the case where all Γ values are set to the upper optimization box constraints. It is not possible for an optimization solution to reach objective points above this curve if Γ is the only optimization variable.

Figure 4.16 shows the solution of the optimization problem with an objective that is twice as steep as the baseline case. Since this objective is also linear and goes through the origin, the optimal solution if there were no box constraints on the adhesive energy would be an infinitely strong strip at a location along the beam, effectively clamping it. In the baseline case the solution with box constraints was to spread the adhesive out slightly behind the location of the analytical solution. In this case the same type of solution is reached, however even at the maximum allowed adhesive energy the last objective points cannot be reached. Figure 4.16(a) shows a dotted line indicating the maximum possible force for a given tip displacement with the box constraints.

The remaining objective points can be reached without increasing the box constraints on Γ by also assigning optimization variables to the beam width. As in the baseline case where width and Γ are optimization variables a hinge forms ahead of the majority of the adhesive energy distribution. This demonstrates that otherwise unreachable objectives can be obtained if additional optimization variables are used.

Figure 4.18 shows an objective which has the same first 10 objective points as the baseline case but then has a decreasing force-displacement relation afterward. This objective has no analogous analytical solution. Figure 4.18(a) shows that the objective was not converged on as well as in other the case with other objectives. The curve is especially jagged in the downward sloping region. A more smooth response may be possible if more objective points are added, although a smooth downward sloping response may not be obtainable by varying the adhesive energy alone. The solution shown in Figure 4.18(b) shows a non-intuitive distribution. This demonstrated that adhesive distributions that do not have analytical solutions can be obtained using topology optimization.

The objective shown in Figure 4.19(a) has the same slope as the baseline objective but is shifted vertically in the force-displacement plane. This shifts it outside of the envelope of obtainable objective points. Like the hill objective, this objective does not have an intuitive or analytically obtainable solution. The adhesive distribution solution gradually increases to a maximum adhesive energy and then gradually tapers off. As in the hill case, this example demonstrates that design optimization can be utilized to design adhesive patterns that are not otherwise obvious. For more complicated adhesion problems and surface geometries or objectives there most likely is no intu-

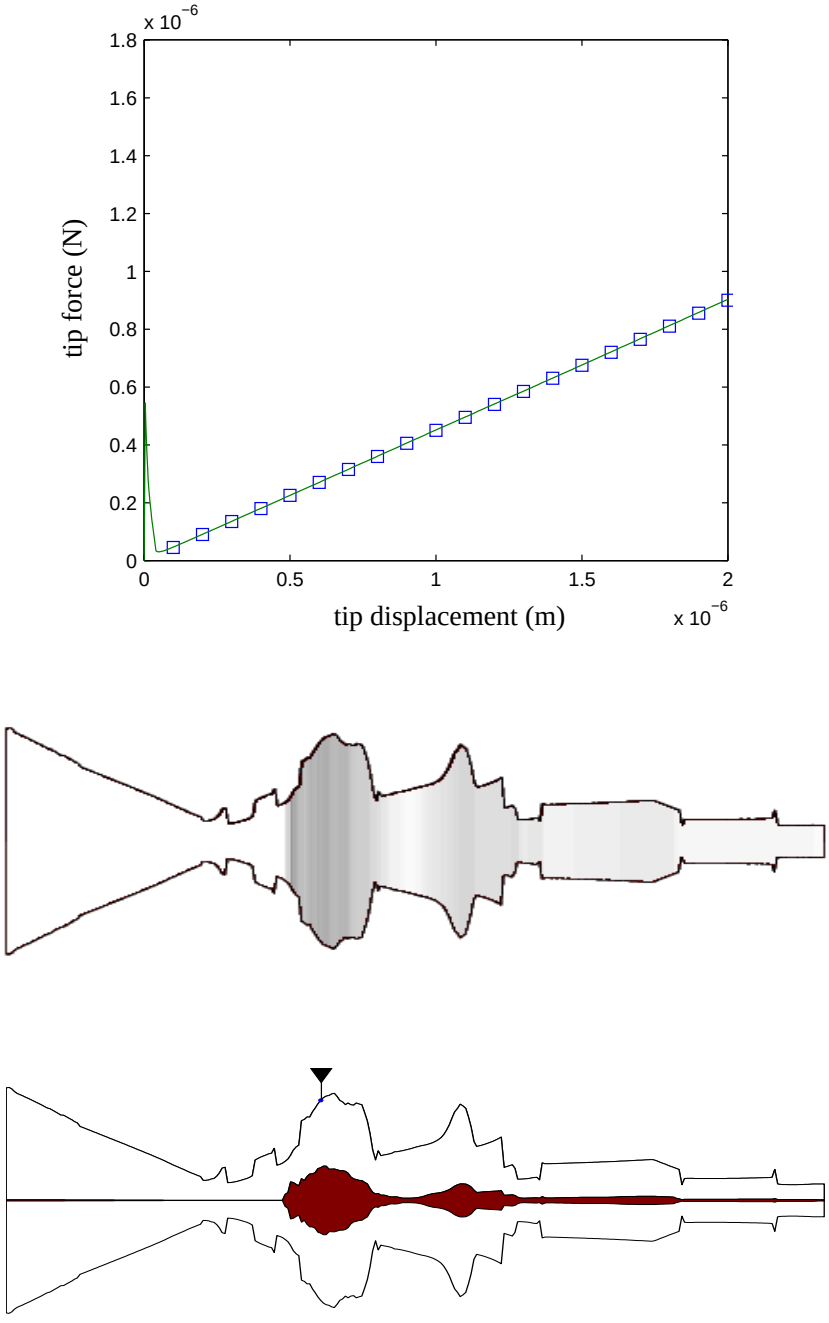

Figure 4.14: The beam optimization problem with both adhesion energy and width as variables with beam area constrained to 25% of the unconstrained solution. (a) Tip force versus tip displacement. (b) Top-down view of beam shape with adhesion energy distribution superimposed. (c) Reinterpretation of adhesion energy distribution to be constant Γ and variable width independent of beam width. Marker indicates final location of crack tip.

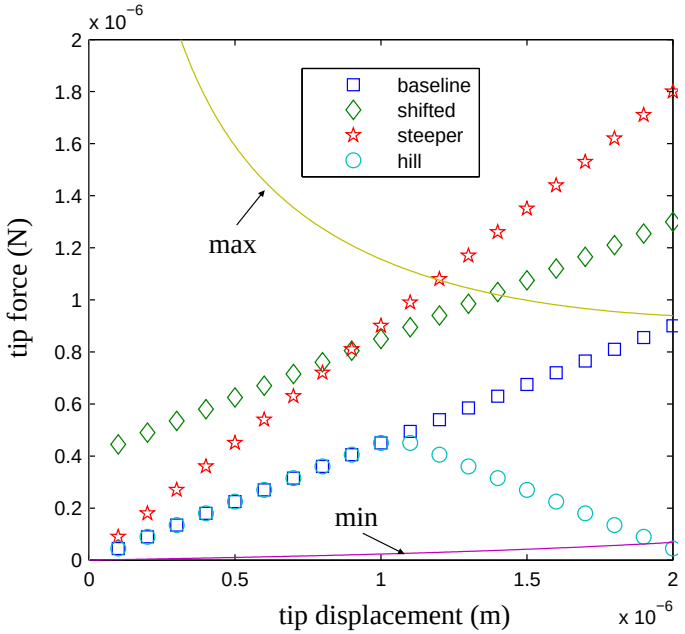

Figure 4.15: Maximum and minimum bounds of possible solutions given box constraints with various objectives.

itive solution.

4.2.2.3 Beam Stiffness Study

In Chapter 3 the delamination problem for a uniform adhesive energy distribution was studied over a range of beam stiffness values. As the stiffness of the beam relative to the adhesive strength decreased the analysis became tempermental and took more steps to converge. This was due to the increasing curvature of the beam at the crack tip, which reduced the number of elements in the adhesive zone, shown in Figure 4.20. In optimization problems, intermediate solutions can arise where the the crack tip encounters strong strips of adhesive relative to the beam strength, creating convergence problems and derailing the optimization procedure. The beam delamination problem is relatively well-behaved in this regard, but convergence issues do arise when the beam Young's modulus is too low. Figure 4.21 shows the solution of the baseline delamination problem with reduced beam stiffnesses. As the beam gets weaker the maximum force that the adhesive can support is reduced, making fewer objective points reachable. The optimization routine moves the adhesive strip further toward the beam tip as the beam Young's modulus decreases. For values of E smaller than 1×10^7 the optimization problem stopped converging.

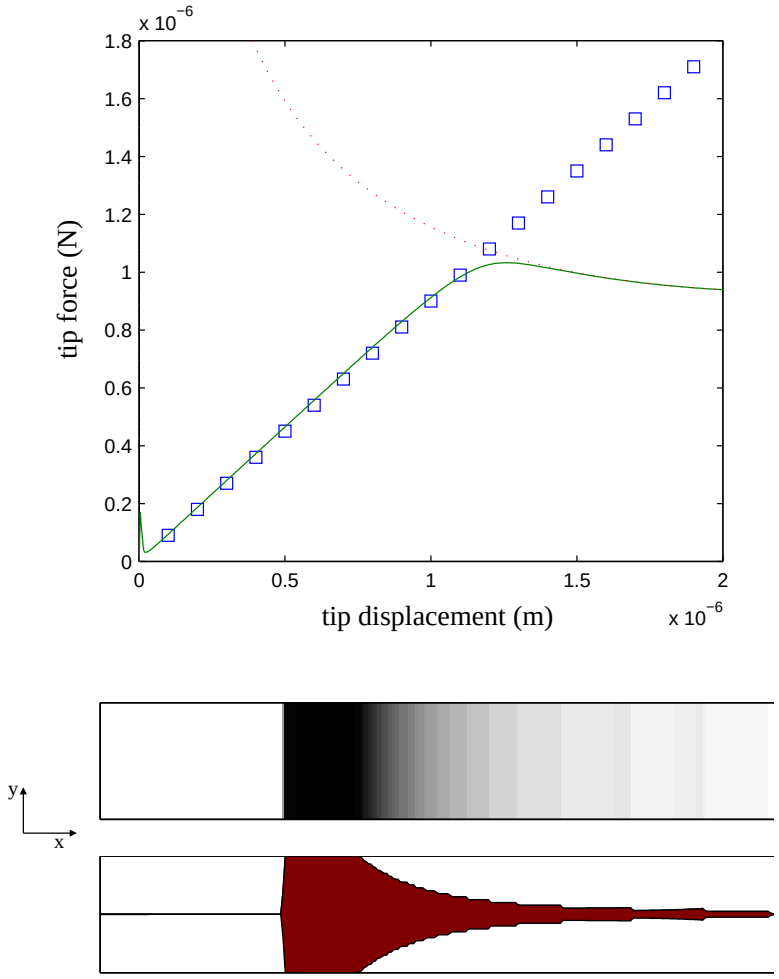

Figure 4.16: Optimization problem with steeper objective. (a) Tip force versus tip displacement. (b) The distribution of adhesive energy along the beam-substrate interface.

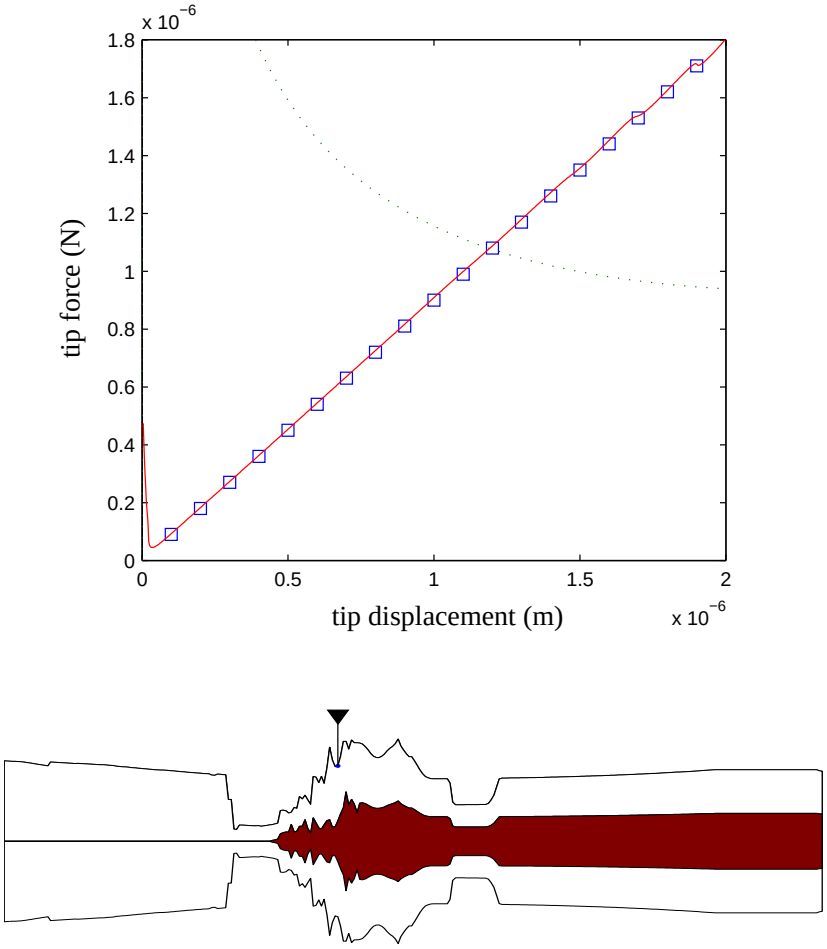

Figure 4.17: Optimization problem with steeper objective including beam width as optimization variables. (a) Tip force versus tip displacement. (b) The shape of the optimal beam and the optimal adhesive energy distribution.

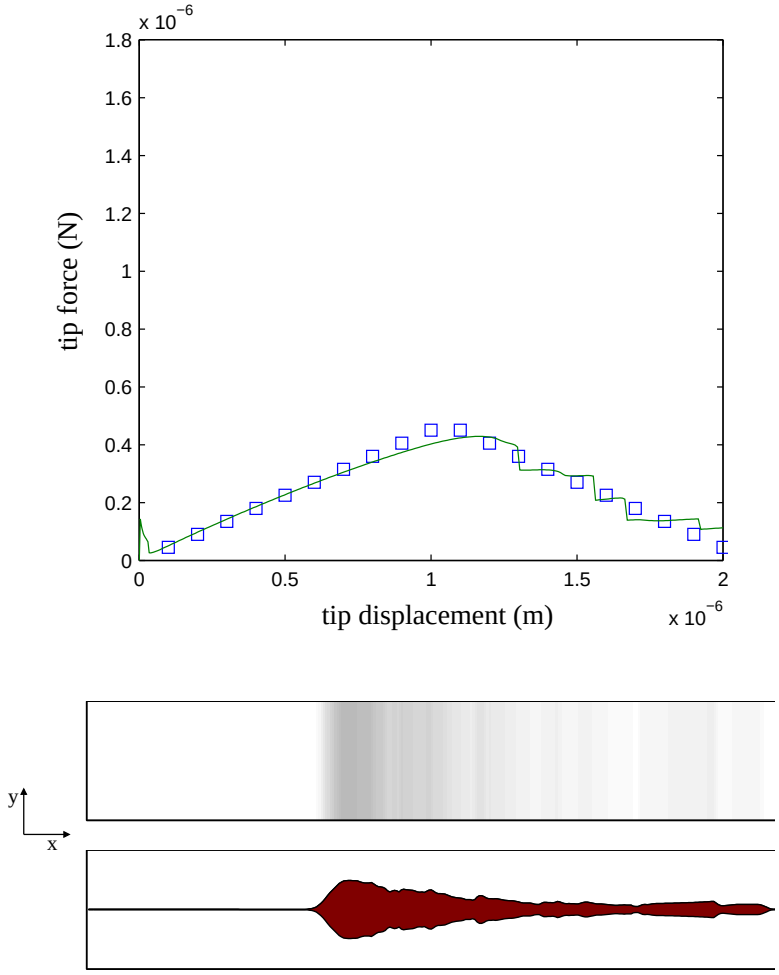

Figure 4.18: Optimization problem with ’Hill’ objective. (a) Tip force versus tip displacement. (b) The distribution of adhesive energy along the beam-substrate interface.

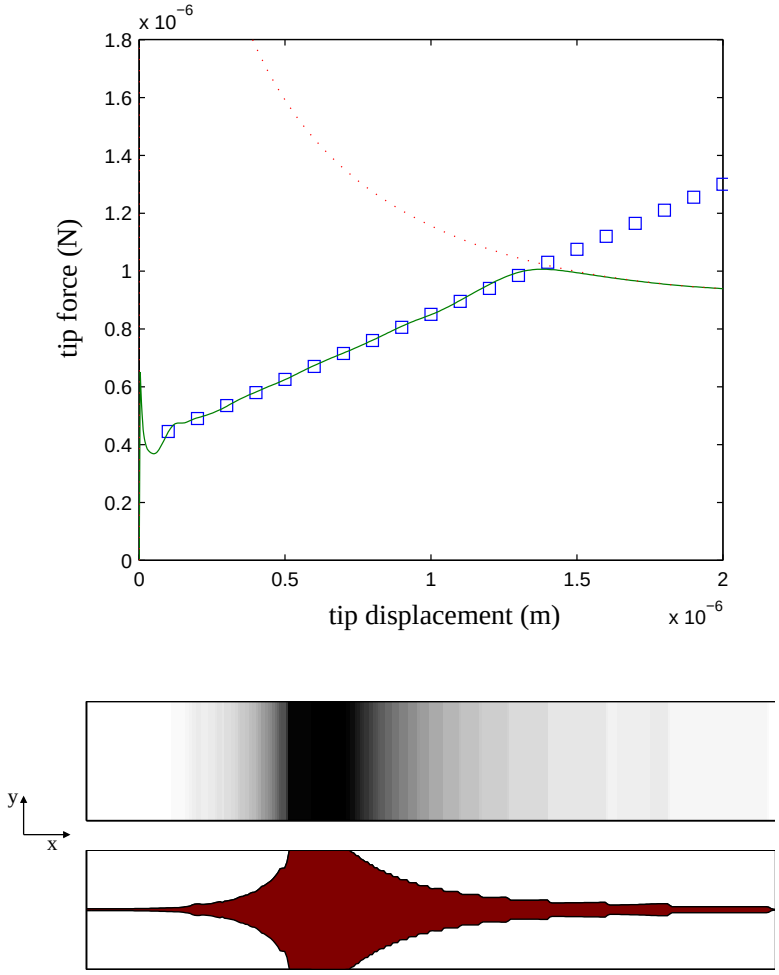

Figure 4.19: Optimization problem with vertically shifted objective. (a) Tip force versus tip displacement. (b) The distribution of adhesive energy along the beam-substrate interface.

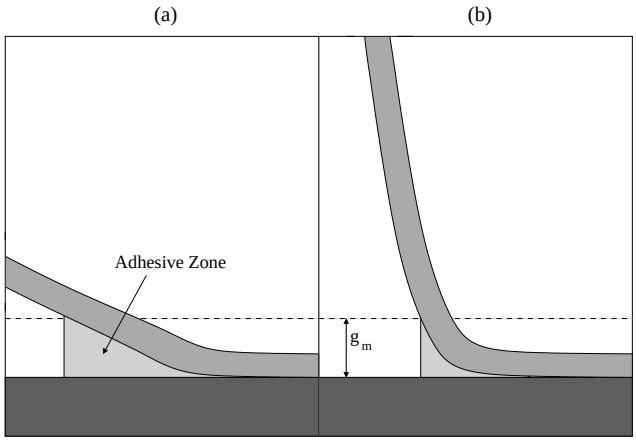

Figure 4.20: Adhesive zone sizes for different beam stiffnesses. (a) For a stiff beam there is less curvature at the crack tip and the length of beam that is in the adhesive zone but not in contact is larger. (b) For a weaker beam there is more curvature at the crack tip and fewer elements of the beam in the adhesive zone.

4.3 Cylinder Compression Example

The cylinder compression optimization example is an extension of the analysis presented in Section 3.4. In that example the relationship between adhesive/contact force and contact area was studied and compared to analytical results. For optimization purposes, the force-displacement characteristic is instead studied and optimized, as it was for the beam optimization example. The objective is to minimize the difference between the force on the top surface of the cylinder and specified objective points at certain value of displacement of the top surface. This objective is defined in an identical way to that of the beam problem, shown in Figure 4.6 and Equation 4.14. The variables in this case are the adhesive energies per are Γ in each InterQuad element, also just as in the beam optimization case.

There are some differences between the set-up in this case and the case described in Section 3.4. One difference is that here the Lennard-Jones adhesion model is used instead of the triangular model. While the triangular model made for a more straightforward comparison between the numerical and analytical results, which used a Dugdale model, the Lennard-Jones model is the most compatible with optimization due to more useful gradients for sensitivities. Another difference is the problem parameters. The problem needed to be shifted well out of the JKR regime to ensure that the analysis at each optimization step could converge. The problem parameters for the optimization problem are shown in Table 4.7.

The range of possible force-displacement solutions given Γ_{min} and Γ_{max} is shown in Figure 4.22(a). In the minimum adhesive case contact forces dominate. As the cylinder is lowered into the substrate, the force is effectively zero until contact when the gap between the cylinder and substrate closes at a displacement of $-4 \times 10^{-3} m$, at which times contact forces begin to take effect. In the case of maximum adhesive, there is a large positive adhesive force that dominates,

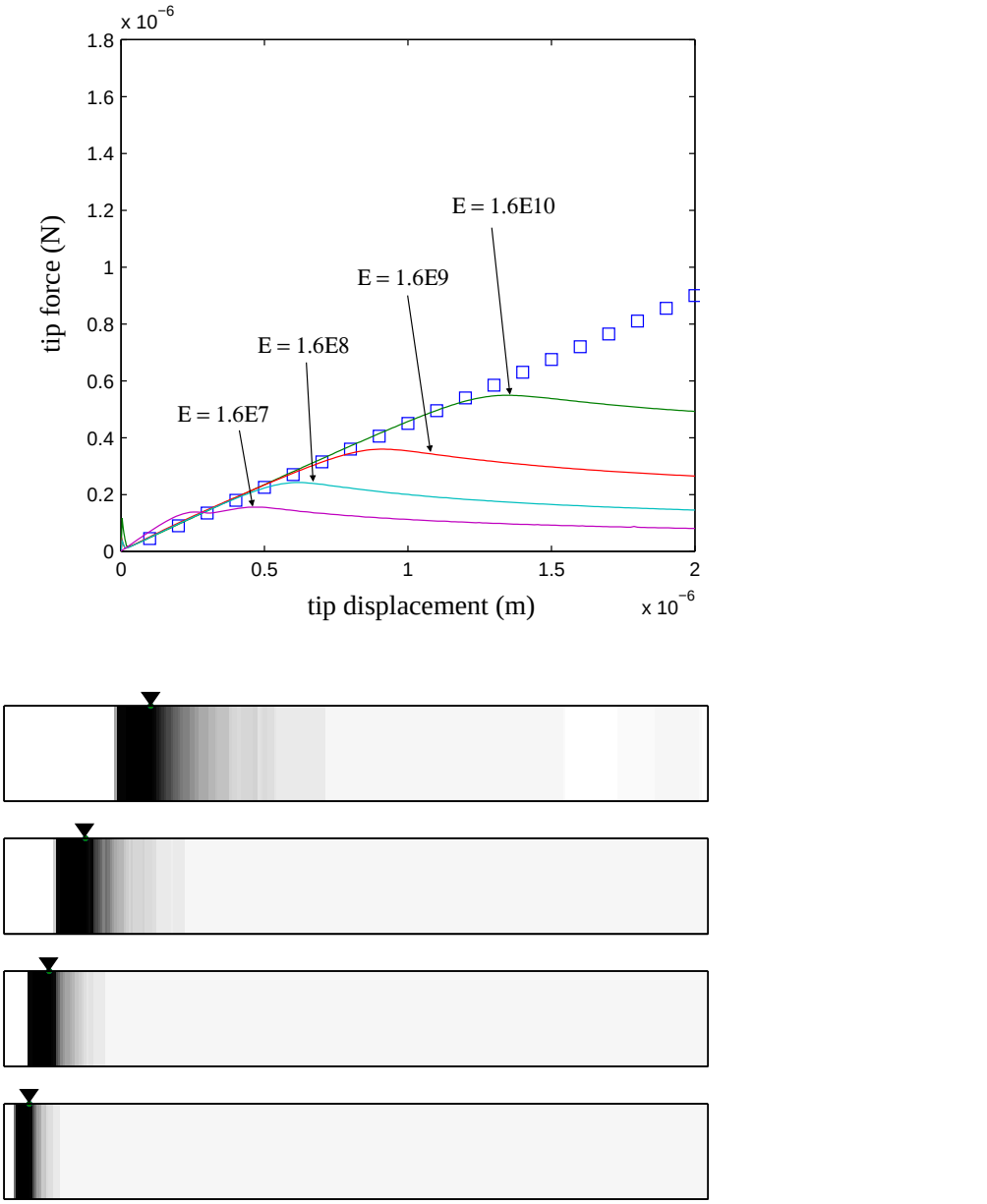

Figure 4.21: A study of optimization results when beam stiffness is reduced. (a) Tip force versus tip displacement. (b) The distribution of adhesive energy along the beam-substrate interface for increasingly weak beams.

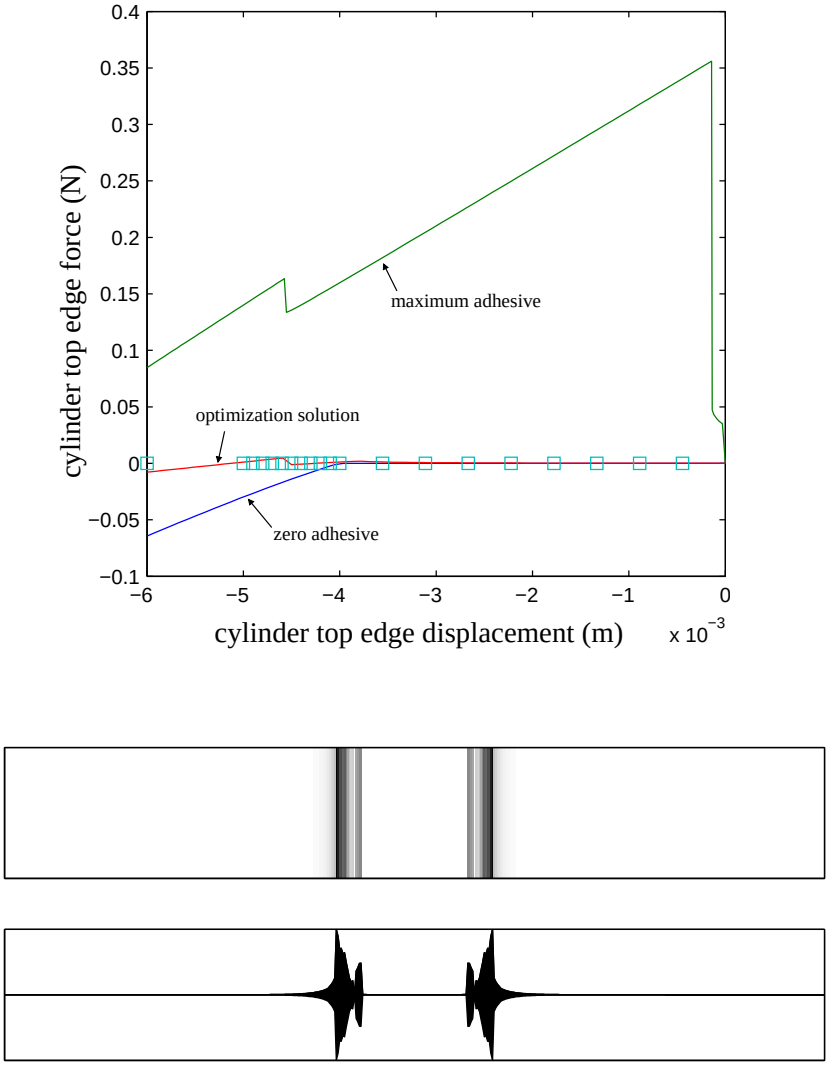

Figure 4.22: Adhesive distribution optimization of zero-force contact cylinder problem. (a) Force versus displacement at the top surface of the cylinder with max/min adhesive envelope shown. (b) The distribution of adhesive energy along the cylinder-substrate interpreted as fixed adhesive width (top) and fixed adhesive energy (bottom).

variable	value	description
E	$1 \times 10^{10}\,Pa$	cylinder Young's modulus
ν	0.23	cylinder Poisson's ratio
L	$8 \times 10^{-6}\,m$	cylinder length
R	$8\,m$	cylinder radius of curvature
g_0	$4 \times 10^{-3}\,m$	initial gap between cylinder and substrate
g_m	$1 \times 10^{-4}\,m$	Lennard-Jones gap corresponding to maximum adhesive force
c	$1 \times 10^{13}\,\frac{N}{m^3}$	contact penetration penalty
Γ_{max}	$1 \times 10^{6}\,\frac{N}{m}$	maximum allowed adhesive energy per area
Γ_{min}	$1 \times 10^{-6}\,\frac{N}{m}$	minimum allowed adhesive energy per area
tol	1×10^{-7}	absolute residual convergence tolerance

Table 4.7: Nominal values for the parameters in the cylinder optimization example problem

even when contact is initiated for the entire displacement range studied. For larger displacements the contact forces begin to dominate in the case of maximum adhesive as well.

The objective for this problem, shown in Figure 4.22(a), is for the force on the upper surface of the cylinder to remain zero over the entire range of displacements studied. The physical meaning of this is that the adhesive pattern is such that for any given displacement within a specified range, the repulsive penetration prevention forces acting inside the contact area and the attractive adhesive forces acting both inside and outside the contact area balance each other out. Several objective points are grouped together near where contact forces first begin to dominate.

The solution to the optimization problem is a very close match to the objective. The resulting adhesive pattern is shown in Figure 4.22(b). As with the beam problem, the results can be interpreted as either variations in adhesive strength or as variations in the width of the adhesive in each element between the cylinder and the substrate. The results are symmetric about the center low point of the cylinder, which makes sense given the symmetry in the problem set-up. The solution has no adhesive at the center elements, allowing the results to closely match the zero adhesive solution up until the point of contact. As the more peripheral cylinder elements come into active adhesive range with the substrate, the adhesion energy is increased to offset the forces that counter penetration. The cylinder optimization problem demonstrates that optimization is possible with more complicated surface geometries than the beam example.

4.4 Sheet Wrapping Example

As with the other examples in this chapter, the optimization of the sheet wrapping problem is an extension of the analogous problem in Chapter 3. This example demonstrates optimization using 3D shell elements and adhesive InterShell interface elements. In this case the optimization variables are the adhesion energies between the cylinder and the sheet in each element along the interface. The objective, also as in previous examples, is to match a specified force-displacement curve

by minimizing the area between the current and target displacement curves. Here, the force and displacement are measured at the midpoints of the sheet, where the displacements are prescribed. Figure 4.23 shows the results of an optimization case with a linear objective. In this case, the initial value for Γ in all elements was the maximum allowed value (box constraint), $5.0 \times 10^{-4} \frac{J}{m^2}$. This is a relatively gentle adhesive energy compared to that used in the Chapter 3 example, allowing the use of a static solver. The optimizer was not able to converge exactly to the objective curve. This is due to physical limitations in the problem; the curvature of the cylinder relative to the sheet limits the number of InterShell elements in the ”active” gap range where changing the adhesion energy can have a large impact. For large gaps, changing the adhesion energy has nearly no impact on the solution since the adhesive forces are weak. The optimized adhesive distribution is symmetric, which is expected due to the symmetry in the problem geometry and boundary conditions. It removes adhesive from the center of the interface to minimize the for for initial small displacement values, and then the adhesion energy grows further from the center to begin increasing adhesive forces. The remaining adhesive energy left at the sides of the sheet/cylinder interface is due to the initial conditions and the relatively small sensitivities in this region, as described in Section 4.2.1.1.

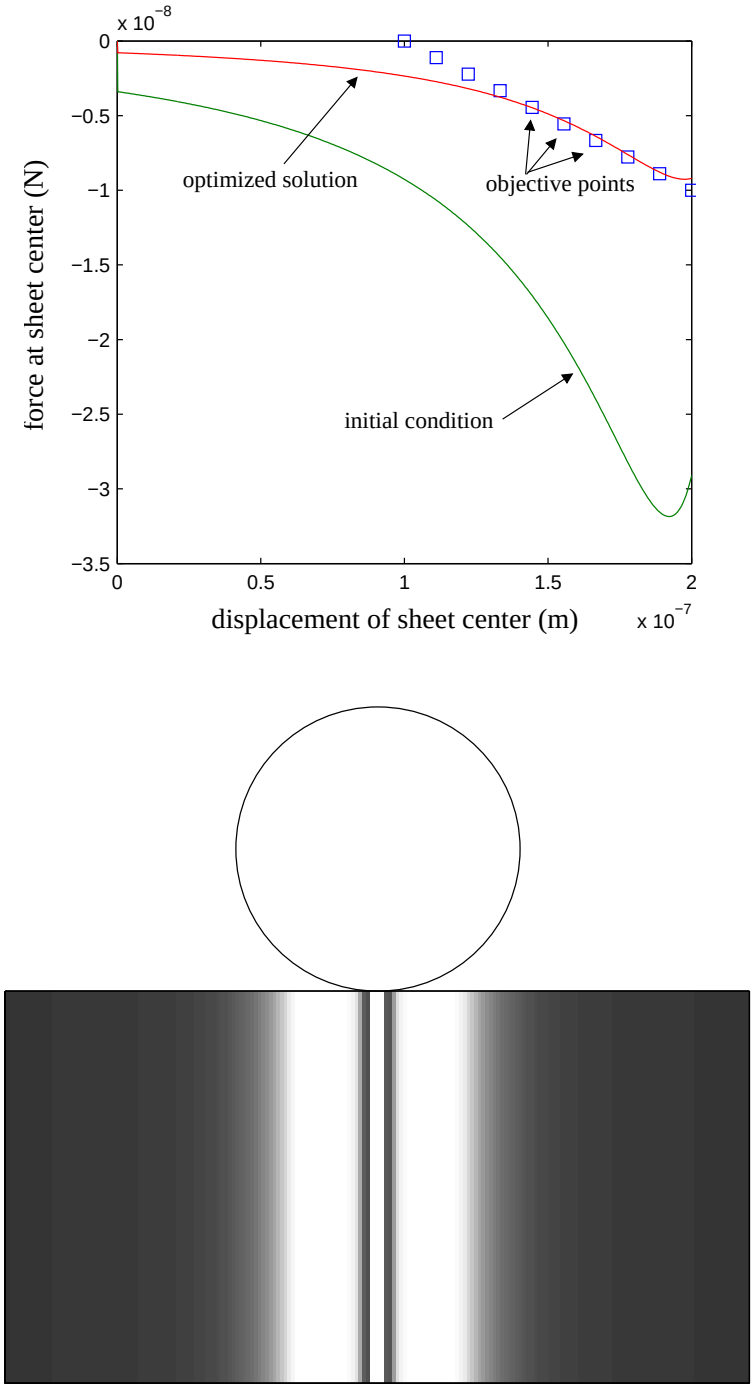

Figure 4.23: Adhesive distribution in optimization of sheet wrapping problem. (a) Force versus displacement at the center of the sheet for the initial case with maximum adhesive and the optimized solution.. (b) The distribution of adhesive energy along the cylinder/sheet interface for the optimized case.

Chapter 5

Summary and Recommendations for Future Work

5.1 Analysis

Several one-dimensional adhesive and contact penetration models were presented. Three Inter elements were formulated, which integrated these adhesive and contact functions as they acted between two surfaces. For the InterBeam element, a correction to account for beam thickness in the gap measurement was used. The nonlinear solver was described, including the use of displacement control to traverse limit points and the adaptive step size algorithm employed. An example problem was described where a beam which, initially adhered to a substrate, was delaminated by pulling upwards on on end. An analytical solution for the crack length and beam shape as a function of tip displacement was computed assuming that the adhesive only acted in the region that had not yet delaminated, and was infinitely stiff in that region, effectively clamping the beam at any given crack tip location.

The beam was modeled in both 2D and 3D using beam elements, quadrilateral elements and shell elements and their corresponding Inter elements. The resulting shape profiles of these three models were nearly identical to each other and also to the analytical solution. The main difference between the models and the analytical solution can be attributed in large part to the existence of an adhesive zone outside of the contact area which the analytical model did not take into account.

The beam delamination problem was solved using various adhesive laws, and in general there was agreement between the models in the beam shape under tip displacement to within 6 nm at any given point along the beam. The law that fit the analytical data the best was the Lennard-Jones case, most likely because it was able to more closely match the analytical adhesion assumptions without having convergence problems as the triangular model tended to as the adhesive zone decreased.

The effects that various parameters of the nonlinear solver had on the solution was studied including the convergence tolerance on each nonlinear iteration, the penetration penalty factor, the number of gauss points used to approximate the integral of the adhesive force over the area in the inter elements and the effects of mesh coarseness/refinement. Due to the nature of the nonlinear solution method and how data is saved at specific steps for optimization, it was most logical to use an absolute convergence criterion. A good absolute tolerance was found for the beam problem,

however a new tolerance would need to be found for each new problem solved. The contact penalty is also not a dimensionless quantity, and due to the nature of optimization there is not a good value to scale it by to make a penalty factor from one simulation work in a different one. It was found that the number of Gauss points used had little effect on the beam solution shape profile, but fewer Gauss points created more numerical difficulty and needed more Newton iterations to converge to equilibrium in each step. The mesh refinement study showed that there is an optimal mesh density for a given problem. If the mesh is too coarse the solver has difficulty reaching an equilibrium in each analysis step or may possible not converge at all. this has to do with the crack tip being distributed over too few variables and the tangential stiffness matrix loosing positive definiteness. If the mesh is too fine, the simulation takes much longer to complete with little to no improvement in the solution accuracy.

Finally in the analysis of the beam example the effect of varying the Young's modulus of the beam and the adhesion energy per area of the interface were studied. The resulting beam profiles and tip force-displacement relation vary in the same manner in both studies. This can be explained by the fact that the ratio $\frac{E}{\Gamma}$ can be factored out of the analytical equations. Increasing Γ had the same effect as decreasing E.

Next the analysis of a cylinder in adhesive contact with a rigid substrate was studied. Here the applied force at the top of the cylinder as it relates to the radius of contact was simulated for two extreme cases and compared to analytical results from the literature. The data in both the JKR and Hertz cases matched with analytical results.

5.2 Optimization

The analytical sensitivities of optimization criteria to optimization variables were computed and compared to numerical results in simple single Inter element problems. For optimization the Lennard-Jones adhesive model is the best because not only is it a smooth function but it has gradients everywhere with respect to optimization variables, while this is not the case in the other adhesive models presented.

An optimization problem was defined for the beam delamination case where the area between an objective tip force-displacement curve and the current iteration was minimized with the adhesive energy of groups of elements along the beam interface as the optimization variables. First a preconstructed solution was analyzed where the objective curve was generated by applying a known adhesive distribution along the beam. The variables were then set to other initial conditions and the optimizer found the original distribution as the optimal solution. A study of starting from different initial conditions showed that this particular example was not very sensitive to initial conditions, but this is not the case in general for adhesive optimization.

Next the beam problem was optimized with objective force-displacement curves that were not the result of analysis of a known adhesive distribution. In the baseline case a linear curve was the objective. This objective has an analytical solution for the case of infinite adhesive energy,

effectively clamping the material to the substrate at a certain location along the beam. In the optimization framework there was a box constraint on the range of admissible adhesive energies. Although the analytical solution was not obtainable, the optimizer found a similar solution by spreading adhesive in a strip in the region just behind where the beam would be clamped in the analytical case. Furthermore, if the total amount of adhesive energy is also minimized by including it in the objective function, unnecessary adhesive energy behind the crack tip is removed, leaving only the amount needed to meet the force-displacement objective.

In the case of the beam delamination problem, a single element spans the entire width of the beam. For this reason, the resulting adhesive distribution can be reinterpreted as a constant adhesion energy but only taking up a percentage of the entire beam width, effectively reducing the adhesive energy for that group of elements. Thus a 0-1 adhesive distribution is obtained for any beam delamination problem solved in this fashion. Alternately, gradients in adhesion energy along an interface can be allowed. This result can be manufactured by varying the surface roughness in the interface.

Beam width was studied as an optimization variable. The optimizer did not converge when the adhesive energy was held constant across the beam while width was an optimization variable, but a solution was achieved if both width and adhesive energy were optimization variables. In fact, objectives that were not reachable given the box constraints on Γ alone became reachable when both Γ and width are optimization variables.

Other objectives were applied to the optimization problem that do not have obvious analytical solutions. The optimizer was able to find adhesive distributions that converged to these objectives, implying that adhesive topology optimization is a useful tool for designing surfaces to meet adhesive objectives that are not easily obtained though other methods.

The baseline optimization problem was solved with a range of beam stiffnesses. As the beam stiffness decreased, the adhesive strip moved toward the tip of the beam. For very weak beams, the optimizer stopped converging.

In the final section, the cylinder problem of Chapter 3 was revisited in an optimization framework. Here, as in the beam optimization example, the objective was to match specified force-displacement points as the cylinder is pressed into the substrate. The optimization variables were the energy of adhesion in each interface element between the cylinder and the substrate. Specifically, the objective was for the contact forces to counterbalance the adhesion forces at every displacement step, creating no net force on the cylinder even when it is in contact with the substrate. The optimizer converged on a solution that met this objective, demonstrating that this design optimization approach to adhesive patterning is effective for more complicated surface geometries than in the beam problem.

5.3 Future Work

Design optimization for structures in adhesive contact is a rich area that still has much room for exploration. It is desirable to capture additional interfacial forces, especially friction which can play a large role in adhesive contact. However, friction is a nonconservative force and requires a dynamic nonlinear solver. To solve optimization problems with friction, other nonconservative forces, or other dynamic problems transient sensitivity analysis needs to be implemented.

While the interface element approach captures adhesion between prescribed sites it is not possible to enforce adhesion or penetration penalties between any two arbitrary surfaces in a design. This becomes desirable in dynamic systems or systems with large displacements where adhesive contact sites are not known beforehand. For these cases an interface element that connects specific nodes on surfaces should be replaced by a search algorithm that detects adequately small gaps between all possible interfaces. This will also alleviate the need for matching meshes on contacting surfaces, facilitating the design of more complicated geometries. Additionally penetration should be prevented by a Lagrange multiplier method instead of by a penalty factor.

These modifications and expansions on the finite element code will greatly expand the types and complexity of design problems that can be solved. Problems of interest include those involving multiphysics such as heat or electric conduction across an adhesive interface and interactions between soft particles immersed in an external force field, such as an electrostatic or a flow field, which have a broad range of applications in areas including manufacturing and processing.

References

[1] K. Autumn, Y. A. Liang, S. T. Hsieh, W. Zesch, W.-P. Chan, W. T. Kenny, R. Fearing, and R. J. Full. Adhesive force of a single gecko foot-hair. *Nature*, 405:681–685, 2000.

[2] J. M. Baney and C.-Y. Hui. A cohesive zone model for the adhesion of cylinders. *J. Adhesion Sci. Technol.*, 11(3):393–406, 1997.

[3] Martin P. Bendsoe and Ole Sigmund. *Topology Optimization: Theory, Methods and Applications*. Springer, 2003.

[4] R. S. Bradley. The cohesive force between solid surfaces and the surface energy of solids. *Philos. Mag.*, 13:853–862, 1932.

[5] Scott Buechler and Martin Dunn. Structural effects of SWCNTs due to mechanical deformation and van der Waals forces. In *ASME Applied Mechanics and Materials Conference*, 2007.

[6] Vivien J. Challis, Anthony P. Roberts, and Andrew H. Wilkins. Fracture resistance via topology optimization. *Struct. Multidisc. Optim.*, 177:383–399, 1999.

[7] Sung-San Cho and Seungho Park. Finite element modeling of adhesive contact using molecular potential. *Tribol. Internat.*, 37:763–769, 2004.

[8] Frank W. DelRio, Maarten P. de Boer, James A. Knapp, E. David Reedy Jr., Peggy J. Clews, and Martin L. Dunn. The role of van der Waals forces in adhesion of micromachined surfaces. *Nature Materials*, 4:629–634, 2005.

[9] B. V. Derjaguin, V. M. Muller, and Y. P. Toporov. Effect of contact deformations on the adhesion of particles. *J. Colloid Interface Sci.*, 53(2):314, 1975.

[10] B. V. Deryagin. *Kolloid Z.*, 69:163, 1934.

[11] E. A. Fancello. Topology optimization for minimum mass design considering local failure constraints and contact boundary conditions. *Struct. Multidisc. Optim.*, 32:229–240, 2006.

[12] Carlos A. Felippa. *Nonlinear Finite Element Methods*. unpublished, 2007.

[13] Huajian Gao, Xiang Wang, Haimin Yao, Stanislav Gorb, and Eduard Arzt. Mechanics of hierarchical adhesion structures of geckos. *Mech. Materials*, 37:275–285, 2005.

[14] A. K. Geim, S. V. Dubonos, I. V. Grigorieva, K. S. Novoselov, A. A. Zhukov, and S. Yu. Shapoval. Microfabricated adhesive mimicking gecko foot-hair. *Nature Materials*, 2:461–463, 2003.

[15] N. J. Glassmaker and C. Y. Hui. Elastica solution for a nanotube formed by self-ahesion of a folded thin film. *J. Appl. Phys.*, 96(6):3429–3434, 2004.

[16] H. L. Groth and P. Nordlund. Shape optimization of bonded joints. *Internat. J. Adhesion Adhesives*, 11:204–212, 1991.

[17] Tobias Hertel, Richard Martel, and Phaedon Avouris. Manipulation of individual carbon nanotubes and their interaction with surfaces. *J. Phys. Chem. B*, 102:910–915, 1998.

[18] Heinrich Hertz. Ueber die Beruhrung fester elastischer Korper. *Journal fur die reine und angewandte Mathematik*, 92:156–171, 1882.

[19] D. Hilding, A. Klarbring, and J Petersson. Optimization of structures in unilateral contact. *Appl. Mech. Rev.*, 52(4):139–160, 1999.

[20] A. Hilleborg, M. Modeer, and I. E. Petersson. Analysis of crack formation and crack growth in concrete by means of fracture mechanics and finite elements. *Cement Concrete Res.*, 6:773–782, 1976.

[21] C.-Y. Hui, Y. Y. Lin, J. M. Baney, and E. J. Kramer. The mechanics of contact and adhesion of periodically rough surfaces. *J. Polym. Sci. Part B: Polym. Phys.*, 39:1195–1214, 2001.

[22] V. Jegatheesan and S. Vigneswaran. Deep bed filtration: mathematical models and observations. *Crit. Rev. Environ. Sci. Technol.*, 35:515–569, 2005.

[23] K. L. Johnson. Mechanics of adhesion. *Tribology International*, 31(8):413–418, 1998.

[24] K. L. Johnson and J. A. Greenwood. An adhesion map for the contact of elastic spheres. *J. Colloid Interface Sci.*, 192:326–333, 1997.

[25] K. L. Johnson, K. Kendall, and A. D. Roberts. Surface energy and the contact of elastic solids. *Proc. R. Soc. Lond. A.*, 324:301–313, 1971.

[26] James A. Knapp and Maarten P. de Boer. Mechanics of microcantilever beams subject to combined electrostatic and adhesive forces. *Journal of Microelectromechanical Systems*, 11(6):754–764, 2002.

[27] B. Liu, Y. Huang, H. Jiang, S. Qu, and K.C. Hwang. The atomic-scale finite element method. *Comput. Methods Appl. Mech. Engrg.*, 193:1849–1864, 2004.

[28] Fritz London. *Zeitschrift fur Physik*, 60:245, 1930.

[29] Nilesh D. Mankame and G.K. Ananthasuresh. Topology optimization for synthesis of contact-aided compliant mechanisms using regularized contact modeling. *Computers and Structures*, 82:1267–1290, 2004.

[30] Y. Masuda, K. Tomimoto, and K. Koumoto. Two-dimensional self-assembly of spherical particles using a liquid mold and its drying process. *Langmuir*, 19(13):5179–5183, 2003.

[31] Daniel Maugis. Adhesion of spheres: The JKR-DMT transition using a Dugdale model. *Journal of Colloid and Interface Science*, 150(1):243–269, 1992.

[32] Daniel Maugis. *Contact, Adhesion and Rupture of Elastic Solids*. Number 130 in Solid-State Sciences. Springer, 2000.

[33] Daniel Maugis, M. Barquins, and R Courtel. Griffith cracks and adhesion of elastic solids. *Metaux-Corrosion-Industrie*, 605:1–10, 1976.

[34] Matthew A. Meitl, Zheng-Tao Zhu, Vipan Kumar, Keon Jae Lee, Xue Feng, Yonggang Y. Huang, Ilesanmi Adesida, Ralph G. Nuzzo, and John A. Rogers. Transfer printing by kinetic control of adhesion to an elastomeric stamp. *Nature Materials*, 5:33–38, 2006.

[35] Carlo Menon and Metin Sitti. A biomimetic climbing robot based on the gecko. *J. Bionic Eng.*, 3:115–125, 2006.

[36] Y. Mi, M. A. Crisfield, and G. A. O. Davies. Progressive delamination using interface elements. *J. Composite Materials*, 32(14):1246–1272, 1998.

[37] Carmelo Militello and Carlos A. Felippa. The first andes elements: 9-dof plate bending triangles. *Computer Methods in Applied Mechanics and Engineering*, 93(2):217–246, 1991.

[38] Andrzej Myslinski. Topology and shape optimization of contact problems using a level set. In *6th World Congresses of Structural and Multidisciplinary Optimization, Rio de Janeiro, 30 May - 03 June 2005, Brazil*, 2005.

[39] Michael T. Northen and Kimberly L. Turner. A batch fabricated biomimetic dry adhesive. *Nanotechnology*, 16:1159–1166, 2005.

[40] Joseph M. Pajot. *Topology optimization of geometrically nonlinear structures including thermo-mechanical coupling*. PhD thesis, University of Colorado at Boulder, 2006.

[41] J.T. Pereira, E. Fancello, and C.S. Barcellos. Topology optimization of continuum structures with material failure constraints. *Struct. Multidisc. Optim.*, 26:50–66, 2004.

[42] Joakim Petersson and Michael Patriksson. Topology optimization of sheets in contact by a subgradient method. *Internat. J. Num. Meth. Eng.*, 40:1295–1321, 1997.

[43] M. Raous, L. Cangemi, and M. Cocu. A consistent model coupling adhesion, friction, and unilateral contact. *Comput. Methods Appl. Mech. Engrg.*, 177:383–399, 1999.

[44] E. David Reedy Jr. Thin-coating contact mechanics with adhesion. *J. Mater. Res.*, 21(10):2660–2668, 2006.

[45] Cory J. Rupp, Anton Evgrafov, Kurt Maute, and Martin L. Dunn. Design of phononic materials/structures for surface wave devices using topology optimization. *Struct. Multidisc. Optim.*, 34:111–121, 2007.

[46] Oliver G. Schmidt and Karl Eberl. Nanotechnology: Thin solid films roll up into nanotubes. *Nature*, 410:168, 2001.

[47] M. Sitti and R. Fearing. Synthetic gecko foot-hair micro/nano-structures as dry adhesives. *J. Adhesion Sci. Technol.*, 17:1055–1073, 2003.

[48] Krister Svanberg. A globally convergent version of MMA without linesearch. In *Proceedings of the First World Congress of Structural and Multidisciplinary Optimization, 28 May - 2 June 1995*, pages 9–16.

[49] D. Tabor. Surface forces and surface interactions. *Journal of Colloid and Interface Science*, 58(1):2–13, 1977.

[50] Noureddine Tayebi and Andreas A. Polycarpou. Reducing the effects of adhesion and friction in microelectromechanical systems (MEMSs) through surface roughening: comparison between theory and experiments. *J. Appl. Phys.*, 98(073528), 2005.

[51] John Tsibouklis, Maureen Stone, Adrian A. Thorpe, Paul Graham, Vanessa Peters, Rene Heerlien, James R. Smith, Keith L. Green, and Thomas G. Nevel. Preventing bacterial adhesion onto surfaces: the low-surface-energy approach. *Biomaterials*, 20(13):1229–1235, 1999.

[52] Peter Wriggers. *Computational Contact Mechanics*. Wiley, 2002.

[53] Haimin Yao and Haujian Gao. Optimal shapes for adhesive binding between two elastic bodies. *J. Colloid Interface Sci.*, 298:564–572, 2006.

[54] Youngjoo Yee, Kukjin Chun, Jong Duk Lee, and Chang-Jin Kim. Polysilicon surface-modification technique to reduce sticking of microstructures. *Sensors and Actuators A*, 52:145–150, 1996.

[55] Y.-P. Zhao, L. S. Wang, and T. X. Yu. Mechanics of adhesion in MEMS - a review. *J. Adhesion Sci. Technol.*, 17(4):519–546, 2003.

[56] Yang Zhaoa, Tao Tong, Lance Delzeit, Ali Kashani, M. Meyyappan, and Arun Majumdar. Interfacial energy and strength of multiwalled-carbon-nanotube-based dry adhesive. *J. Vac. Sci. Technol. B*, 24(1):331–335, 2006.

DISTRIBUTION:

1	MS 0123	D. Chavez, LDRD Office, 1011 (electronic)
1	MS 0899	Technical Library, 9536 (electronic)

Sandia National Laboratories